The Pennsylvania State University
The Graduate School

# SMALL X RESUMMATION IN PERTURBATIVE QCD

A Dissertation in
Physics
by
Wanchen Li



Submitted in Partial Fulfillment
of the Requirements
for the Degree of

Doctor of Philosophy

May 2024

The dissertation of Wanchen Li was reviewed and approved by the following:

Anna Staśto
Professor of Physics
Dissertation Advisor
Chair of Committee

Mark Strikman
Distinguished Professor of Physics

Kohta Murase
Associate Professor of Physics and Astronomy & Astrophysics

James Brannick
Professor of Mathematics

Irina Mocioiu
Associate Professor of Physics
Director of Graduate Studies

# Abstract

In this dissertation, we study the small $x$ resummation in perturbative Quantum Chromodynamics (QCD). In the past decades, the particle accelerators with increasing center of mass energies have opened up the so-called small Bjorken $x$ regime. We are interested in the small $x$ evolution of gluon density, which is described by the Balitsky-Fadin-Kuraev-Lipatov (BFKL) equation. Currently, the BFKL kernel eigenvalue is known up to the next-to-leading logarithm (NLL) accuracy. However, it leads to instabilities in calculations and indicates the necessity of resummation of higher order terms. We present the BFKL formalism, parton evolution, and QCD in general in the introductory Chapter 1 of this dissertation.

In Chapter 2, we introduce the kinematical constraints and renormalization group improved resummation. We analyze the different types of kinematical constraints in the BFKL equation and show their impact on the BFKL effective eigenfunction and gluon density by numerical calculations. Furthermore, we describe the scale changing transformation in the renormalization group improved resummation and the corresponding expansion technique. We demonstrate the pole structure of the BFKL equation with kinematical constraints in Mellin space in BFKL up to NLL and in $N = 4$ supersymmetric Yang-Mills theory (sYM) up to next-to-next-to leading logarithmic level (NNLL). We investigate the scale changing transformations and give proof of the vanishing sub-leading poles in $N = 4$ sYM to all orders.

In Chapter 3, we present a more detailed description of the renormalization group improved resummation. We perform the numerical calculation of the structure function $F_2$ in Deep Inelastic Scattering (DIS) and subsequently a fit to the data from HERA collider. We achieve a very good description of the structure function $F_2$ and its charm component $F_2^c$ simultaneously. The resulting unintegrated gluon density is consistent with the calculations based on similar approaches available in the literature.

In Chapter 4, we perform the renormalization group improved resummation of the photon-gluon impact factors. We construct the resummed cross section for virtual photon-photon scattering which incorporates the resummed impact factors and BFKL gluon

Green's function up to the NLL. Conditions on the resummed cross section are constructed by requiring consistency with standard high energy factorization in the collinear limits. Our result is consistent with previous impact factor calculations at the next-to-leading order (NLO), apart from a new term proportional to $C_F$ for the longitudinal photon polarization. We compute the resummed cross section and compare it with the LEP data and previous calculations. Our result is lower than the LL approximation but higher than the pure NLL one, being more consistent with the experimental data.

# Table of Contents

# List of Figures

# List of Tables

# List of Symbols

| | |
|---|---|
| LL, NLL, NNLL | The leading logarithm (LL) approximation;<br>The next-to-leading logarithm (NLL) approximation;<br>The next-to-next-to-leading logarithm (NLL) approximation. |
| LO, NLO, NNLO | The leading order (LO);<br>The next-to-leading order (NLO);<br>The next-to-next-to-leading order (NNLO). |
| $\alpha_s$ | The Strong coupling constant, p. 7 |
| $\beta$ | The $\beta$ function in the running coupling, p. 7 |
| $b$ | A constant in the running coupling, p. 7 |
| $N_c$ | The number of color, p. 8 |
| $N_f$ | The number of flavors, p. 8 |
| $C_F$ | The Casimir constant defined in the color group, $C_F = (N_c^2 - 1)/2N_c$, p. 8 |
| $Q^2$ | The minus photon virtuality, p. 10 |
| $x$ | The Bjorken $x$, p. 10 |
| $y$ | The inelasticity, p. 10 |
| $s$ | The center of mass energy squared in DIS, p. 10 |
| $W^2$ | The invariant mass squared of the hadron states in DIS, p. 10 |
| $\sigma$ | The cross section, p. 10 |
| $F_2, F_1$ | The structure functions, p. 10 |
| $\mathcal{A}$ | The scattering amplitude, p. 11 |
| $s, t, u$ | The Mandelstem variables, p. 11 |

| | |
|---|---|
| $e_q$ | The electric charge of a quark, p. 11 |
| $e$ | The electric charge of an electron, p. 11 |
| $\delta(x)$ | The Dirac delta function, p. 12 |
| $\mathcal{O}(x)$ | A term that is in the order of its argument, p. 12 |
| $q(x), \overline{q}(x), g(x),$ | The parton densities, p. 16 |
| $P_{ab}$ | The DGLAP splitting function, p. 16 |
| $T_R$ | A constant defined in the color group, $T_R = 1/2$, p. 17 |
| $C_A$ | A constant defined in the flavor group, $C_A = N_c$, p. 17 |
| $\omega$ | The Mellin variable conjugate to $x$, p. 18 |
| $\gamma_{ab}$ | The anomalous dimension, p. 18 |
| $f(x, k^2)$ | The unintegrated gluon density in the $(x, k^2)$ space, p. 19 |
| $\overline{\alpha}_s$ | The rescaled strong coupling constant, $\overline{\alpha}_s = \alpha_s C_A/\pi$, p. 20 |
| $\alpha\,(t)$ | The Regge trajectory, p. 23 |
| $S_{ab}$ | The unitary Lorentz invariant $S$ matrix, p. 23 |
| $\rho, \lambda$ | The Sudakov parameters, p. 24 |
| $\mathbf{k}, \mathbf{k}', \mathbf{q}$ | The boldface two-dimensional vectors are the transverse components of the four-vectors $k, k', q$ respectively, p. 25 |
| $G_0$ | The color factor for the singlet state, p. 26 |
| $G_0^{(8)}$ | The color factor for the octet state, p. 26 |
| $\delta_{ab}$ | The Kronecker delta function, p. 26 |
| $\epsilon_G(t)$ | An infra-red divergent integral noted for wider usage, p. 26 |
| $\mathcal{G}$ | The gluon Green's function, p. 29 |
| $\mathcal{K}$ | The kernel in the BFKL equation, p. 33 |
| $\phi$ | The impact factor, p. 33 |
| $s_0$ | The energy scale in the high energy factorization, p. 33 |
| $\Theta(x)$ | The Heaviside function, p. 34 |
| $\chi$ | The BFKL eigenfunction in the Mellin space, p. 35 |

| | |
|---|---|
| $\overline{f}(\omega, k^2)$ | The unintegrated gluon density in the $(\omega, k^2)$ space,, p. 35 |
| $\tilde{f}(\omega, \gamma)$ | The unintegrated gluon density in the $(\omega, \gamma)$ space,, p. 35 |
| $\overline{b}$ | The rescaled $b = \pi b/C_A$, p. 37 |
| $\chi_{\text{eff}}$ | The effective solution to $\omega = \overline{\alpha}_s \chi(\omega, \gamma)$, p. 50 |
| $A_1(\omega)$ | The non-singular part of the singlet gluon anomalous dimension, p. 58 |
| $S_q$ | The off-shell photon-gluon partonic cross section, p. 73 |
| $Y$ | The rapidity, p. 87 |
| $\Phi(\omega, \gamma)$ | The impact factor in the renormalization group improved resummation, p. 90 |
| $G(\omega, \gamma)$ | The gluon Green's function in the renormalization group improved resummation, p. 90 |
| $X(\omega, \gamma)$ | The BFKL eigenfunction in the renormalization group improved resummation, p. 90 |
| $\tilde{\sigma}$ | The collinear integrated of the cross section in the $(\omega, Q^2)$ space, p. 95 |
| $\tilde{\tilde{\sigma}}$ | The collinear integrated of the cross section in the $(\omega, \gamma)$ space, p. 97 |
| $B, \overline{B}, D, \overline{D}$ | The coefficients of the certain poles of the LO resummed impact factors, p. 100 |
| $M, \overline{M}$ | The coefficients of the certain poles of the NLO resummed impact factors, p. 103 |
| $U, V$ | The coefficients of the certain poles of the LL and NLL resummed BFKL eigenfunctions, p. 103 |
| $\eta, \overline{\eta}$ | The coefficients of the certain poles of the NLO BFKL impact factors, p. 104 |
| $H_1$ | The coefficients of a certain pole of the NLL BFKL eigenfunctions, p. 104 |
| $\mathcal{P}_L$ | The coefficients of a certain pole of the NLL longitudinal cross section, corresponding to the photon-quark interaction, p. 112 |

# Acknowledgments

I thank my advisor, Prof. Staśto, for her patience and great advice throughout my Ph.D. years. She helped me a lot whether it was about the basic knowledge and skills in the field or the opportunities to join the research, collaborations, and conferences.

I thank my committee members and every other researcher I communicated with for their patience.

I thank my parents and friends for their accompany.

This Ph.D. program is supported by the U.S. Department of Energy Grant DE-SC-0002145.

Disclaimer: The findings and conclusions of this dissertation do not necessarily reflect the view of the funding agency.

# Preface

Chapters 2,3 and 4 in this dissertation are based on the following publications:

1. M. Deak, K. Kutak, W. Li and A. M. Staśto, “On the different forms of the kinematical constraint in BFKL,”
   Eur. Phys. J. C **79**, no.8, 647 (2019)
   doi:10.1140/epjc/s10052-019-7171-z [arXiv:1906.09062 [hep-ph]].

2. W. Li and A. M. Stasto, “Structure functions from renormalization group improved small x evolution,”
   Eur. Phys. J. C **82**, no.6, 562 (2022)
   doi:10.1140/epjc/s10052-022-10523-6 [arXiv:2201.10579 [hep-ph]].

3. D. Colferai, W. Li and A. M. Stasto, “Renormalization group improved photon impact factors and the high energy virtual photon scattering,”
   JHEP **01**, 106 (2024)
   doi:10.1007/JHEP01(2024)106 [arXiv:2311.07443 [hep-ph]].

In publication 1, I calculated the Mellin space results with another author independently and gave proof of an all-order pattern.

In publication 2, I coded the computation of the structure function and fitted it with experimental data.

In publication 3, I computed the cross section numerically and compared it with previous calculations and experimental data.

# Chapter 1 Introduction to the Small x Physics in QCD

## 1.1 Introduction

Quantum chromodynamics (QCD) is a well-established quantum field theory developed to describe strong interactions. QCD is regarded as a cornerstone of the Standard Model of particle physics, which also includes the theories of electromagnetic and weak interactions. The fundamental objects in QCD are quarks and gluons which make up the composite particles called hadrons. Hadrons can be divided into two main categories: baryons, which usually have three, so called valence, quarks, and mesons which have a valence quark-antiquark pair. Examples of baryons are protons and neutrons, which are the main building blocks of nuclei in all atoms. An example of a meson is a pion, first discovered in cosmic rays [1]. In recent years more exotic hadrons have been discovered in accelerators: tetraquarks (formed by 2 quarks and 2 anti-quarks) and pentaquarks (formed by 4 quarks and 1 anti-quark), see review in [2, 3].

QCD is an SU($N_c$) non-Abelian theory, where the $N_c = 3$ is the number of colors. The prefix 'chromo' stands for the color, parallel to the prefix 'electro' of the quantum electrodynamics (QED), while the color is loosely analogous to the electric charge. Similar to the photon propagating the electromagnetic force in QED, the gluon is the force carrier in QCD. However, unlike photons, gluons are allowed to self-interact through fundamental 3- or 4- gluon vertices. This is the consequence of the non-Abelian nature of QCD.

There are several important features of QCD:

- Asymptotic freedom: Experiments at SLAC in the late 60s showed that the quarks in the proton behave as if they were free. That suggested that the strong interaction is weak at high energy (or short distance). Theoretically, the asymptotic freedom is a consequence of the non-Abelian nature of QCD. The strong interaction coupling is not constant but decreases for higher energy. This feature allows to use calculational techniques based on the perturbative expansion in small values of strong coupling, when high energy scales are present in the process. The magnitude of the running coupling at different scales denotes the division of perturbative and non-perturbative QCD.

- Color confinement: This feature refers to the phenomenon that the quarks and gluons cannot be isolated from the hadrons. Outgoing quarks and gluons produced in scatterings need to undergo color rearrangement to produce colorless hadrons in the final state, through the non-perturbative process called hadronization. Although the color confinement has not been proven in analytical QCD, it is well established, e.g., in lattice QCD simulations [4].

- Chiral symmetry breaking: In QCD, this feature refers to the spontaneous breaking of a chiral symmetry associated with massless fermions. It is regarded as the source of the most masses of the hadrons, whose masses are significantly larger than the simple summation of masses of the quarks.

It would seem at first glance that computing any observable quantity in QCD using perturbative methods is an impossible task due to the fact that the quarks and gluons are confined in hadrons and never observed as asymptotic free states. However, computations can be made in the cases when there is a large scale in the process. In such a case, the cross section will contain regions dominated by large and small values of the strong coupling, and it can be shown that it can be computed through means of the so-called factorization theorems [5]. The factorization in QCD means that the observable cross section can be represented as the convolution of contributions from short distance (perturbative part) and long distance interactions (non-perturbative part). For the short distance part, which is the cross section on the level of partons, one can employ the rigorous techniques of perturbative QCD. On the other hand, the non-perturbative quantity cannot be usually directly computed in QCD since it involves long-distance, strong coupling phenomena[1].

The main idea of the factorization is to renormalize a quantity at a factorization scale $\mu^2$, where certain singularities (for example so called collinear singularities which appear

[1]Other methods might be suitable for computations of these objects like numerical approaches of lattice QCD

in the calculation of the field theory diagrams) are factorized into the non-perturbative part of this quantity. While the non-perturbative part cannot be calculated from first principles, and requires an experimental input, its evolution with the scale $\mu^2$ can be treated perturbatively. The non-perturbative parts of the cross sections, which we shall focus on in this work, are called parton distribution functions. They describe the distribution in momenta (for example longitudinal and/or transverse ) of the partons in the proton or more generally in the hadronic target. They depend on the long distance physics of the proton, but at high scales, their evolution can be computed by means of perturbative QCD, through the evolution equations. These parton distributions are also universal, that means, once extracted from a particular process, for example, Deep Inelastic Scattering of electron on a proton described below. They can be used in a calculation of different observable, like for example Higgs boson production at the Large Hadron Collider. In that case, one can make precise predictions for various cross sections in QCD.

It is thus of fundamental importance to understand in detail the behavior of the parton distribution functions, and in particular the correct structure of the equations that govern their evolution with scales in QCD. Of particular interest is the regime of high energies, since it is probed in the current accelerators like LHC as well as in ultrahigh energy cosmic interactions. As described below this regime is dominated by the gluon distribution.

Deep Inelastic Scattering (DIS) is the process of scattering of leptons off protons and the most precise way to explore the nucleon structure and extract the parton distribution functions. The pioneering DIS experiment at SLAC [6] unraveled for the first time a partonic structure of hadrons. The parton model was established to explain the observed behavior of the cross section. In the simplest parton model, the structure function $F_2$ (the quantity which is proportional to the total cross section in DIS) tends to be only dependent on the so called Bjorken $x$. This variable can be interpreted as the fraction of the longitudinal momentum of the proton carried by the struck parton. The DIS cross section is typically described as a function of two variables: the Bjorken $x$ and the hard scale, the (negative) virtuality $Q^2$ of the momentum transferred between the leptons and protons. The observed independence of the structure function on the variable $Q^2$, consistent with the predictions of the parton model, is called the Bjorken scaling.

In later DIS experiments, however, mild scaling violation was observed. The structure function turned out to be also $Q^2$ dependent. The hard scale means the scale $Q^2$ is much larger than the non-perturbative scale associated with the proton $Q_0^2$. Theoretical calculations of the amplitudes find that for a certain order of the strong coupling $\alpha_s$, the dominant contribution comes with the same order of the large logarithm $\ln(Q^2/Q_0^2)$. Therefore even for the small, perturbative values of the strong coupling $\alpha_s$, we have $\alpha_s \ln(Q^2/Q_0^2) \sim 1$, and thus these logarithms need to be resummed. The Dokshitzer-Gribov-Lipatov-Altarelli-Parisi (DGLAP) equation [7–10] resums all orders of $\alpha_s^n \ln^n(Q^2/Q_0^2)$ and gives the $Q^2$ evolution for the parton distribution functions. In the partonic language, these evolution equations resum multiple splittings of partons into other partons when the scale $Q^2$ is increased.

As the center of mass energy of the accelerators has grown larger, new phenomena were discovered in this high energy regime. The electron-proton collider at HERA was the highest energy DIS experiment constructed so far. This experiment has opened up the regime of the small $x$ physics in DIS. This is because, as we shall see later, the high energy regime corresponds to the small values of Bjorken $x$. One of the most important discoveries at HERA was the strong rise of the structure function $F_2$ at small $x$ [11, 12]. The experimental data at HERA could be well described by the DGLAP evolution, and it was understood that the strong rise of the structure function is driven by the increasing gluon density with decreasing value of Bjorken $x$. However, in the regime of small $x$ or high energy, another large logarithms appear and need to be resummed. To be precise, in the high energy regime corresponding to very small $x$, the dominant logarithm is $\ln(1/x)$. The Balitsky-Fadin-Kuraev-Lipatov (BFKL) equation [13–20] resums all orders of the leading logarithm (LL) $\alpha_s^n \ln^n(1/x)$ and corresponds to the evolution of the gluon density with $x$. The BFKL evolution predicts a power like increase of the gluon density in the form $x^{-\lambda}$. This behavior is reminiscent of the power growth with the energy of the amplitudes in the so-called Regge theory, which was a pre-QCD framework. This approach was based on the universal assumptions about the scattering matrix, like unitarity, analyticity, and Lorentz invariance. In this approach the behavior of the total cross sections was assumed to be governed by the exchange of the object, called the Pomeron, which would lead to the slow increase with the energy of the observable cross sections. Thus the solution to the BFKL equation, which exhibits the power like behavior with the decreasing $x$ (and thus increasing energy $s$) is often referred as the hard BFKL Pomeron.

The LL BFKL predicted the sharp increase of $F_2$ at small x, $\sim x^{-\lambda}$. However, a known issue of the LL BFKL is that it leads to a hard Pomeron intercept $\lambda = 4\ln 2\,\overline{\alpha}_s$, which is too large for experimental data. Decades of effort were put into the calculation of the next-to-leading logarithm (NLL) BFKL eigenfunctions [21, 22]. The NLL results tame the LL growth, but at the same time, are large and negative and can make calculations unstable [23–25].

Thus, an important problem in the description of the small $x$ Bjorken regime arises. On one hand, the DGLAP evolution successfully describes the experimental data on structure function at HERA. On the other hand, the BFKL framework, which should be suitable for the description of the small $x$ regime seemed to be unstable. Therefore resummation of higher orders in BFKL was motivated and developed to stabilize the expansion [26–40] and provide appropriate matching between the two approaches.

The main objective of this dissertation is to investigate and improve the resummation in the small $x$ regime, both in the evolution equation and in the partonic cross sections, the so called impact factors as well as to provide applications of this improved resummation to the phenomenology.

The structure of this dissertation is as follows:

In the remaining part of Chapter 1 we introduce the basics of QCD, Deep Inelastic Scattering, and parton evolution. We discuss the main building blocks of the BFKL equation and the factorization.

In Chapter 2 we analyze the kinematical constraint in the BFKL equation. The idea of the kinematical constraints was first proposed in [41–44]. It was introduced to modify the real gluon emission of the BFKL equation with improved kinematics. It comes from the limit that the four-momentum of the real gluon is dominated by its transverse components. As shown in [43] different forms of this constraint can be imposed depending on the approximations. We study in detail the effects of these different constraints in the BFKL equation. To this aim, we utilize Mellin space, where it is easier to analyze the pole structure of the corrections. We show that all forms of constraints correctly reproduce the leading corrections to NLL BFKL in QCD and up to NNLL in N=4 super Yang-Mills theory. We also provide proof of the vanishing of a certain class of subleading poles in N=4 sYM to all orders. In addition, we study the impact of different forms of kinematical constraint on the gluon density by solving the equation numerically in momentum space. The idea of the renormalization group constraints is also introduced in Chapter 2.

Chapter 3 is focused on the phenomenological applications of the Ciafaloni-Colferai-Salam-Staśto (CCSS) resummation [33, 34, 45]. This resummation features the renormalization group improved small x equation. The CCSS resummation is constructed based on the collinear DGLAP splitting function and exact BFKL up to the NLL accuracy.

It also includes the effect of the kinematical constraint. Appropriate subtractions are formed in the Mellin space to avoid double counting. We compute the structure function following the approach in [44] and fit it to the DIS HERA data. The calculation of the structure function receives the input of the unintegrated gluon density, where we solve the BFKL equation with the implementation of the CCSS resummation. We achieve a great fit to the structure function $F_2$ and its charm component $F_2^c$ simultaneously. In addition, we also fit only to the structure function $F_2$ which results in similar agreements and fit parameters.

In Chapter 4, we extend the idea of the renormalization group improved resummation into the impact factors. Since the observable quantities are cross sections, the resummation needs to be consistently performed for all the building blocks of this quantity. In the high energy limit, the cross sections are obtained through the high energy factorization. In this framework, cross section includes not only the gluon Green's function, which is the solution to BFKL, but also the process-dependent impact factors, which also need to be evaluated in the appropriate order of perturbation theory. In particular, we study the virtual photon-photon high energy scattering where such measurements were carried out in LEP $e^+e^-$ collider [46, 47]. We construct the resummed photon-gluon impact factors by performing the collinear analysis on the resummed cross section in the Mellin space. We perform a numerical computation and achieve a consistent description of the LEP data, in contrast to previous calculations which undershoot the experimental data significantly.

Chapters 2,3 and 4 are based on the publications [48–50].

## 1.2 Basics of the Quantum Chromodynamics

### 1.2.1 Asymptotic freedom

Asymptotic freedom means that the coupling between the particles involved in the strong interaction is zero at zero distance, i.e. asymptotically close to zero at larger energies. Before the foundation of QCD, researchers had already observed this important feature in the deep inelastic scattering (DIS) that the strong interaction is weak at short distances.

Coleman and Gross [51] demonstrated that a field theory with solely Abelian fields cannot be asymptotic free. Indeed, the QCD is established as a gauge theory based on a non-abelian $SU(3)$ color group. The color is an intrinsic property of the quarks and gluons. Gluon, a spin 1 boson, propagates strong interactions between the spin 1/2 fermion quarks. A crucial characteristic of the non-abelian fields is that their nature enables gluons to self-interact.

An intuitive explanation of the asymptotic freedom comes from this self-interacting nature of the gluon fields which mediate between the colored charges (quarks). A color source can emit virtual gluons into the surrounding vacuum. Consequently, the color charges spread out, causing an anti-shielding effect similar to the phenomenon in the dielectric. When two color sources get close, their color "clouds" overlap and result in a smaller coupling strength.

Asymptotic freedom describes the behavior of a vital quantity, the strong coupling constant $\alpha_s$, and thus highlights a major difference between the approaches in QCD, either perturbative or non-perturbative. In Quantum Electrodynamics (QED), the perturbation theory is a powerful and dominant approach that allows for an expansion of an observable into a series of terms in different orders of the fine structure constant $\alpha \approx 1/137$. One can compute the QED expansions order by order perturbatively since the fine structure constant is small. In contrast, the QCD strong coupling constant $\alpha_s$ can be relatively large at low energies, making higher order terms not necessarily smaller than the lower order terms. Moreover, series expansion of observables sometimes is accompanied by some large logarithm featured with different scales, e.g., $\ln Q^2$, $\ln(1/x)$. These scales can jeopardize the reliability of the direct $\alpha_s$ expansion. With such a challenging characteristic of the expansions, various resummation techniques have been developed to address these logarithm series. For the non-perturbative QCD, one would turn to process-dependent models or the lattice QCD which prescribes and simulates a grid in the spacetime.

A renormalization group analysis gives a more quantitative description of the strong coupling constant $\alpha_s$. The $\alpha_s$ runs with a energy scale $Q^2$,

$$Q^2 \frac{\partial \alpha_s(Q^2)}{\partial Q^2} = \beta(\alpha_s). \tag{1.1}$$

Where the $\beta$ function can be expanded as

$$\beta(\alpha_s) = -b_0 \alpha_s^2 \left(1 + b_1 \alpha_s + \cdots\right), \tag{1.2}$$

where

$$\begin{aligned} b_0 &= \frac{11N_c - 2N_f}{12\pi}, \\ b_1 &= \frac{17N_c^2 - 5N_cN_f - 3C_FN_f}{2\pi\left(11N_c - 2N_f\right)}, \end{aligned} \tag{1.3}$$

with $C_F = (N_c^2 - 1)/2N_c$, $N_c$ the number of colors, and $N_f$ the number of flavors. One can quickly see at the leading order $\beta < 0$ if $N_f \leq 16$. Neglecting the $b_1$ and higher order terms, the solution to eq. (1.1) is

$$\alpha_s(Q^2) = \frac{\alpha_s(\mu^2)}{1 + b\alpha_s(\mu^2)\ln Q^2/\mu^2}, \tag{1.4}$$

where $\mu$ is a reference energy scale. In the $N_f = 6$ Standard Model, the negativity of $\beta$ guarantees that at very large $Q^2$, $\alpha_s \ll 1$. This also implies that perturbation theory works well in the limit of high energy QCD. We show the running coupling as a function of energy $Q$ in fig. 1.1. A typical reference value as $\alpha_s(M_z^2) \approx 0.118$ at mass of the $Z$ boson $M_z \approx 91.2$ GeV.

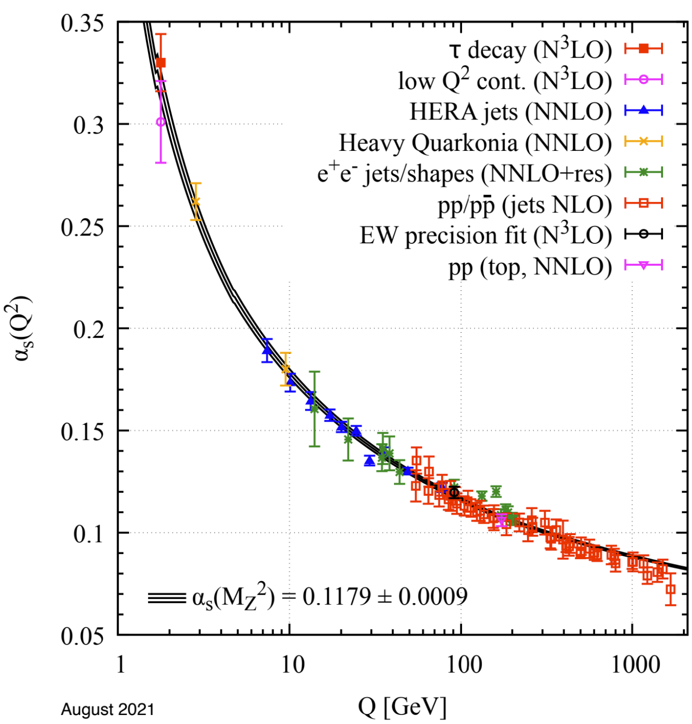


**Figure 1.1.** Running strong coupling extracted from various experiments. Figure from Review of Particle Physics [52]

At low $Q^2$, the running coupling is stronger at long distance. At a distance long enough, the strong interaction exhibits color confinement. The color confinement is a phenomenon that quarks and gluons are confined inside hadrons. All isolated particles we observed are colorless compositions, e.g., mesons, and baryons. When quarks or gluons are produced in a collision, they are separated by enough distance in the outgoing states.

Subsequently, they combine with the new quark-antiquark pairs that appeared from the gluon field and cluster and form jets. This process is called hadronization.

## 1.3 Deep inelastic scattering and parton model

### 1.3.1 Deep inelastic scattering

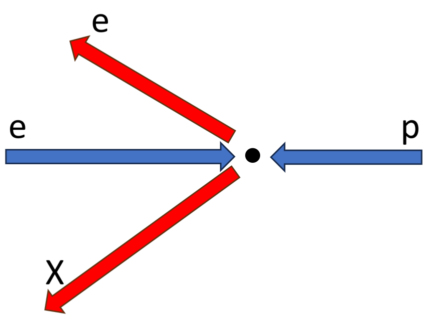


**Figure 1.2.** Schematic representation of the DIS process $ep \to eX$. Incoming(blue) electron($e$) and proton($p$) scatter into outgoing(red) electron($e$) and hadrons($X$).

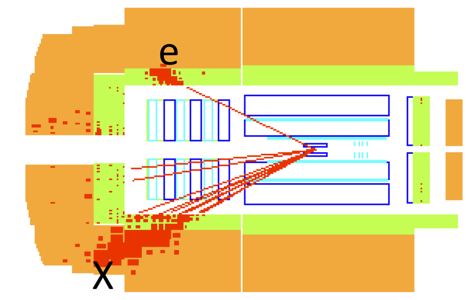


**Figure 1.3.** HERA $e-p$ scattering event observed in the H1 detector [53].

Deep inelastic scattering is one of the most important processes to test the precision of QCD theory and probe the structure of the hadrons. From this process, information about the distribution of quarks and gluons can be extracted, which then can be used for the calculation of cross sections for other high energy scattering processes which involve hadrons. In fig. 1.2, an incoming electron collides with the proton target, resulting in an outgoing electron and a hadronic state, denoted by $X$. In practice, experiments like HERA configure a beam of electrons of four-momentum $p_1$ to collide with the target protons of four-momentum $p_2$, to produce the outgoing electrons of four-momentum $p_1'$ and the hadrons $X$ in the final state. An example of a DIS event at HERA collider is shown in fig. 1.3.

The diagrammatic representation of the DIS process is shown in fig. 1.4. We consider here single boson exchange, is mostly dominated by the photon exchange process. In the following, we also assume that the initial particles are unpolarized. The exchanged virtual photon four-momentum is $q$.

The following useful variables are usually considered in the context of the Deep

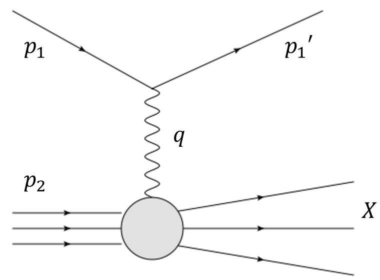


**Figure 1.4.** Diagram of the Deep Inelastic $e-p$ Scattering.

Inelastic Scattering, illustrated in fig. 1.4

$$\begin{aligned} Q^2 &= -q^2, \\ x &= \frac{Q^2}{2p_2 \cdot q}, \\ y &= \frac{q \cdot p_2}{p_1 \cdot p_2} \\ s &= (p_1 + p_2)^2 \\ W^2 &= (p_2 + q)^2, \end{aligned} \tag{1.5}$$

with $Q^2 \geq 0$ the minus photon virtuality, $x$ the Bjorken variable, $y$ the inelasticity, $s$ the center of mass energy squared and $W^2$ the invariant mass squared of the hadron state $X$. The unpolarized differential cross section is

$$\frac{\mathrm{d}^2\sigma}{\mathrm{d}x\mathrm{d}Q^2} = \frac{4\pi\alpha^2}{Q^4}\left\{\left[1 + (1-y)^2\right] F_1(x, Q^2) + \frac{1-y}{x}\left[F_2(x, Q^2) - 2xF_1(x, Q^2)\right]\right\}, \tag{1.6}$$

where the structure functions $F_2, F_1$ parametrize the inner structure of the target proton probed by the virtual photon. Such two terms correspond to the absorption of virtual photons with transverse $F_T = 2xF_1$ or longitudinal $(F_L = F_2 - 2xF_1)$ polarizations.

## 1.3.2 Structure functions in the parton model

Historically, the idea of the parton model was proposed before the underlying theory of the strong interactions was understood. It was formulated [54–56] to explain the DIS experiments, especially the short-distance observations. The essence of the model is that in a high energy electron-hadron collision, it is a good approximation to neglect the interactions between the hadron constituents(partons) and treat the electron coupling to a single target constituent, which can be treated as almost free, via the photon vertex.

A simplification of this dynamics relies on the relativistic view of the high energy collisions as illustrated in fig. 1.5. A fast-moving proton will be affected by both Lorentz time dilation and length contraction. Qualitatively speaking, the time dilation signifies that the interaction between the constituent partons happens on time scales much longer than the interaction of the electron with the parton. Meanwhile, length contraction makes the 'travel' time of the electron through the proton much shorter. In the parton model, one thus assumes that the electron interacts with a single parton, which can be treated as a free particle. As a result, the whole cross section is the summation of all the subprocesses given by the partonic cross section, weighted by the probabilities of finding the different types of partons inside the proton.

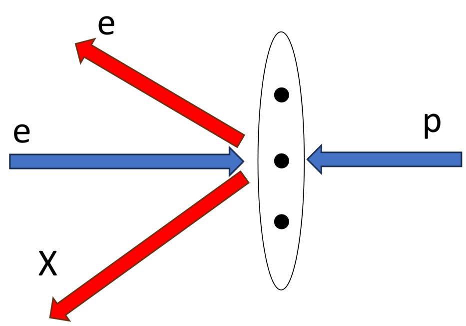


**Figure 1.5.** Relativistic view of the scattering of incoming(blue) electrons($e$) and protons($p$) scatters into outgoing(red) electrons($e$) and hadrons($X$).

In QCD literature, the term 'parton' commonly refers to the different elementary particles like gluons, quarks, and antiquarks. The more formal mathematical treatment —the QCD factorization theory—will be introduced later in section 1.4.5 to explain the separation of the long- and short-distance effects of QCD.

We start the quantitative introduction to the parton model with the kinematics of a simple model. In the infinite momentum frame, a proton with four-momentum $p^\mu$ is moving fast enough so that we can neglect its mass. A point-like quark inside this proton with four-momentum $l^\mu = zp^\mu$ carries a fraction $z$ of the parental proton momentum. Neglecting the complicated interaction between the partons, the goal is to find the differential cross section when a virtual photon emitted by an electron probes the constituent quark inside the proton.

Consider the simple scattering of charged spin 1/2 particles, $e(k)+q(l) \to e(k')+q(l')$. The differential cross section due to the exchange of a single photon is well known

$$\frac{\mathrm{d}\sigma}{\mathrm{d}t} = \frac{1}{16\pi s^2}\sum |\mathcal{A}|^2 = \frac{e_q^2 e^4}{8\pi s^2}\frac{s^2+u^2}{t^2}, \tag{1.7}$$

with $\mathcal{A}$ the amplitude, $e_q$ the electric charge of a quark and $e$ the electric charge of an electron, and, $s = (k+l)^2$, $u = (l-k')^2$ and $t = (k-k')^2$ the Mandelstan variables. Now for a constituent quark, with the Mandelstan variables in the deep inelastic scattering from $s = zQ^2/xy$, $u = s(y-1)$ and $t = -Q^2$, we have

$$\frac{\mathrm{d}\sigma}{\mathrm{d}Q^2} = \frac{2\pi\alpha^2 e_q^2}{Q^4}\left[1+(1-y)^2\right]. \tag{1.8}$$

In this massless limit, it holds

$$0 = (zp+q)^2 = q^2 + 2zp\cdot q. \tag{1.9}$$

This implies that $x = z = Q^2/2p\cdot q$. In order to compare eq. (1.6) and eq. (1.8), we can rewrite eq. (1.8) as

$$\frac{\mathrm{d}\sigma}{\mathrm{d}x\mathrm{d}Q^2} = \frac{2\pi\alpha^2 e_q^2}{Q^4}\left[1+(1-y)^2\right]\delta(x-z), \tag{1.10}$$

where we note that $\int_0^1 dx\delta(x-z) = 1$. In this naive model, we conclude

$$F_2 = xe_q^2\delta(x-z) = 2xF_1. \tag{1.11}$$

The physical meaning of the above result is that the structure function $F_2$ provides information about the quark in the proton with momentum fraction $z = x$.

However, it is well known from experiments that the structure function is a continuous distribution instead of a delta function in $x$, see for example fig. 1.6. This is a consequence of the fact that the distribution of the quarks inside the proton does not follow the discrete pattern in $x$ but rather is a continuous distribution over a range of momentum fractions $x$. This motivates us to define a probability distribution $q(z)$ to represent the quark density such that

$$\begin{aligned} F_2(x) &= \sum_{q,\bar{q}}\int_0^1 \mathrm{d}zq(z)e_q^2x\delta(x-z) \\ &= \sum_{q,\bar{q}} e_q^2xq(x). \end{aligned} \tag{1.12}$$

This relation between the structure function $F_2$ and parton density $q(x)$ is valid at $\mathcal{O}(1)$ order.

In fig. 1.7 we schematically illustrate how different assumptions about the parton

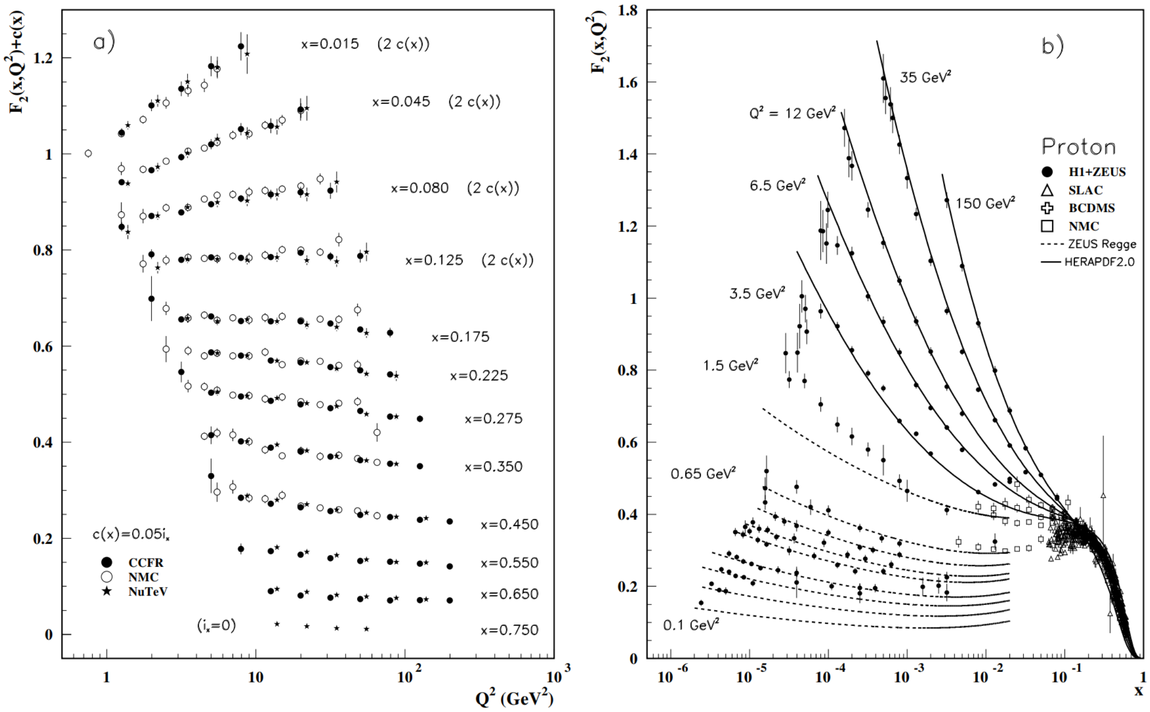


**Figure 1.6.** The $F_2$ structure function from various experiments. Left: as a function of $Q^2$ for fixed $x$, right: as a function of $x$ for fixed $Q^2$ (figure from [52]).

composition of the proton affect the parton density $q(x)$ fig. 1.7:

- (1) The proton is assumed to be a single point-like particle without any content inside. The only particle carries all the momentum and the distribution is described by the Dirac delta $\delta(x-1)$.
- (2) The proton is solely made up of three valence quarks without any interactions between them. Each valence quark carries 1/3 of the proton momentum, i.e., $q(x) = \delta(x - 1/3)$.
- (3) The proton is made up of three valence quarks, but they also interact with each other via the gluons. The gluons redistribute the momentum of the quarks and thus the distribution is continuous as a function of $x$ and peaked in the vicinity of 1/3.
- (4) The proton is made up of three valence quarks. They interact with each other via the gluons. Furthermore, the gluons split into pairs of quarks and antiquarks (sea quarks). The gluon emission is associated with lower momentum than the valence quarks and leads to the rise of the $q(x)$ at $x < 1/3$.

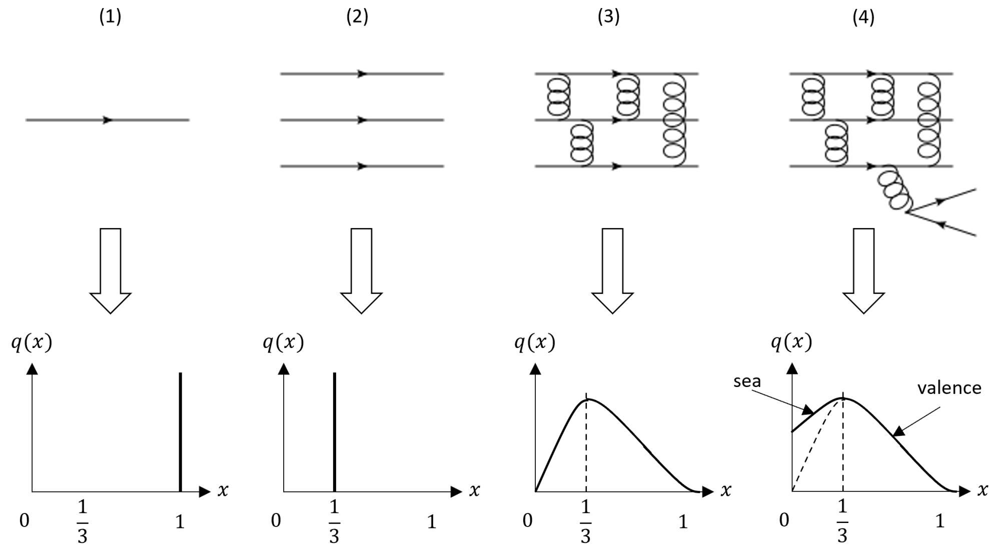


**Figure 1.7.** The parton densities arising due to different assumptions of the parton configuration and dynamics inside the proton.

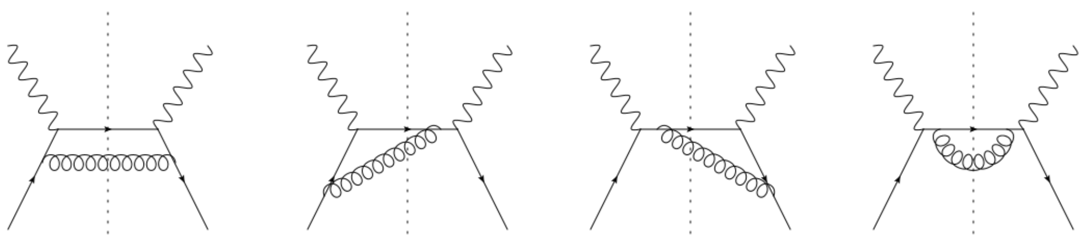

**Figure 1.8.** The $\mathcal{O}(\alpha_s)$ level diagrams of the real gluon emission contribution to DIS.

The relation $F_2 = 2xF_1$ is called the Callan-Gross relation, it holds in the parton model and it is accurate up to $\mathcal{O}(1)$, the order of unity. It is the consequence of the fact that the quarks have spin 1/2. At the order $\mathcal{O}(\alpha_s)$, we follow the approach in [57]. The one-gluon real emission contributions are derived by the calculation of the diagrams in fig. 1.8. The rule of calculation through the diagram cut will be introduced later in section 1.4.2.1. The eq. (1.11) is revisited at $\mathcal{O}(\alpha_s)$,

$$F_2 = xe_q^2 \left\{ \delta(x-z) + \frac{\alpha_s}{2\pi} \left[ P(x) \ln \frac{Q^2}{\kappa^2} + C(x) \right] \right\}, \tag{1.13}$$

where $\kappa$ is a small cut-off momentum to regulate the momentum divergence, the function $C(x)$ stands for the non-divergent terms, and

$$P(x) = C_F \frac{1+x^2}{1-x}, \tag{1.14}$$

is called called splitting function. The constant $C_F$ is defined as $C_F = (N_c^2 - 1)/2N_c$

Another part of the $\mathcal{O}(\alpha_s)$ contributions is from the virtual one-gluon emission diagrams. They are either self-energy corrections to the quark lines or the one-loop photon vertex corrections. We omit the detailed calculations here. But it is worth noting that these loop diagrams are associated with the infrared divergence at $x \to 1$ [58]. The virtual diagrams further modify the $P(x)$,

$$P(x) = C_F \left[ \frac{1 + x^2}{(1 - x)_+} + \frac{3}{2}\delta(1 - x) \right], \tag{1.15}$$

Where the '+' distribution is defined to compensate the endpoint ($x = 1$) singularity,

$$\int_0^1 \mathrm{d}x \frac{f(x)}{(1 - x)_+} = \int_0^1 \mathrm{d}x \frac{f(x) - f(1)}{1 - x}. \tag{1.16}$$

and

$$\frac{1}{(1 - x)_+} = \frac{1}{1 - x}, \quad \text{for } x \neq 1. \tag{1.17}$$

The divergent term $P(x) \ln \frac{Q^2}{\kappa^2}$ arises only from the first diagram in the fig. 1.8, when the gluon is emitted parallel to the quark in the limit gluon transverse momentum $k_t \to 0$.

With these corrections it turns out that $F_2$ also depends on $Q^2$, breaking the sole dependency on $x$ in $O(1)$ order, i.e. the Bjorken scaling. Similar to how we extend eq. (1.11) to eq. (1.12), we can convolute the eq. (1.13) with the quark density $q_0(x)$,

$$F_2(x, Q^2) = x \sum_{q,\bar{q}} e_q^2 \left\{ q_0(x) + \frac{\alpha_s}{2\pi} \int_x^1 \frac{\mathrm{d}z}{z} q_0(z) \left[ P\left(\frac{x}{z}\right) \ln \frac{Q^2}{\kappa^2} + C\left(\frac{x}{z}\right) \right] \right\}. \tag{1.18}$$

Yet eq. (1.18) comes with an inconvenience. The momentum cut-off $\kappa$ is a signal for the existence of the long-range (small momentum) interaction, and such long-range contribution isn't available in perturbation theory by its nature.

A solution to this problem is to separate the long and short-range contributions by factorization. Here, we can introduce a 'renormalized' quark distribution $q(x, \mu^2)$ at a factorization scale $\mu^2$, comparing with the 'bare' quark distribution $q_0(x)$,

$$q(x, \mu^2) = q_0(x) + \frac{\alpha_s}{2\pi} \int_x^1 \frac{\mathrm{d}z}{z} q_0(z) \left[ P\left(\frac{x}{z}\right) \ln \frac{\mu^2}{\kappa^2} + C\left(\frac{x}{z}\right) \right]. \tag{1.19}$$

Therefore,

$$F_2(x,Q^2) = x\sum_{q,\bar{q}} e_q^2 \int_x^1 \frac{\mathrm{d}z}{z} q(x,\mu^2)\left[\delta\left(1-\frac{x}{z}\right) + \frac{\alpha_s}{2\pi} P\left(\frac{x}{z}\right)\ln\frac{Q^2}{\mu^2}\right], \tag{1.20}$$

where the finite term $C(x)$ has been absorbed into the $q(x,\mu^2)$.

### 1.3.3 DGLAP equation

Let $t = \mu^2$ and take the $\ln t$ partial derivative of eq. (1.19), we get the famous Dokshitzer-Gribov-Lipatov-Altarelli-Parisi (DGLAP) equation [7–10],

$$t\frac{\partial q(x,t)}{\partial t} = \frac{\alpha_s(t)}{2\pi}\int_x^1 \frac{\mathrm{d}z}{z} P\left(\frac{x}{z}\right) q(z,t). \tag{1.21}$$

The physical interpretation of this evolution equation is that it resums all the large logarithms of $\ln \mu^2$ stemming from the QCD emissions of the partons.

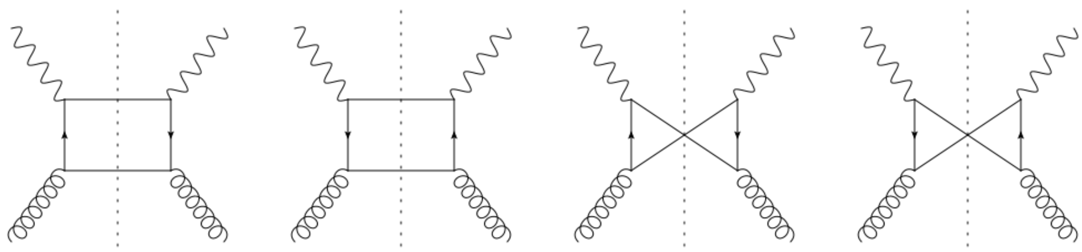

**Figure 1.9.** The $\mathcal{O}(\alpha_s)$ level diagrams with initial gluons in DIS.

In fig. 1.8, we calculate the evolution with an initial quark. For a complete evolution with initial gluon, one must include the $\mathcal{O}(\alpha_s)$ level contribution in fig. 1.9. The $\gamma^* g \to qq$ scattering gives structure function $F_2^g(x,Q^2)$ in the gluon channel, similar to eq. (1.13),

$$F_2^g(x,Q^2) = x\sum_{q,\bar{q}} e_q^2 \frac{\alpha_s}{2\pi}\left(P_{qg}(x)\ln\frac{Q^2}{\kappa^2} + C_g(x)\right). \tag{1.22}$$

Note again, that the divergent logarithm comes from the vanishing quark virtuality limit $|k^2| \to 0$. More generally, with quark flavor number $N_f$, the DGLAP equation is

$$t\frac{\partial}{\partial t}\begin{pmatrix} q_i(x,t) \\ g(x,t)\end{pmatrix} = \frac{\alpha_s(t)}{2\pi}\sum_{q_j,\bar{q}_j}\int_x^1 \frac{\mathrm{d}z}{z}\begin{pmatrix} P_{q_iq_j}\left(\frac{x}{z}\right) & P_{q_ig}\left(\frac{x}{z}\right) \\ P_{gq_j}\left(\frac{x}{z}\right) & P_{gg}\left(\frac{x}{z}\right)\end{pmatrix}\begin{pmatrix} q_j(z,t) \\ g(z,t)\,. \end{pmatrix} \tag{1.23}$$

The splitting function $P_{ab}$ can be interpreted as the probability of finding a parton of type a in a parton of type b when the parton of type b carries a fraction $x$ of the longitudinal momentum of the parental parton. In other words, the splitting function $P_{ab}$ describes the probability of a parton of type b 'splits' into a parton of type a. Since the total number of quarks minus antiquarks is conserved, we have such a sum rule

$$\int_0^1 \mathrm{d}x P_{qq}(x) = 0. \tag{1.24}$$

Considering the total momentum of the proton is also conserved, two more sum rules hold

$$\begin{aligned} \int_0^1 \mathrm{d}x\ x\left[P_{qq}(x) + P_{gq}(x)\right] = 0, \\ \int_0^1 \mathrm{d}x\ x\left[2N_f P_{qg}(x) + P_{gg}(x)\right] = 0. \end{aligned} \tag{1.25}$$

The splitting function $P_{ab}$ can be calculated by perturbation expansion in series of $\alpha_s$

$$P_{ab}(x,\alpha_s) = P_{ab}^{(0)}(x) + \frac{\alpha_s}{2\pi}P_{ab}^{(1)}(x) + \cdots . \tag{1.26}$$

The splitting functions in QCD are known at next-to-leading order (NLO) [59–61] and up to the next-to-next-to-leading order (NNLO) [62, 63]. The expressions for the leading order (LO) DGLAP splitting functions are

$$\begin{aligned} P_{qq}^{(0)}(x) &= C_F\left[\frac{1+x^2}{(1-x)_+} + \frac{3}{2}\delta\left(1-x\right)\right] \\ P_{qg}^{(0)}(x) &= T_R\left[x^2 + (1+x)^2\right], \qquad T_R = \frac{1}{2} \\ P_{gq}^{(0)}(x) &= C_F\left[\frac{1+(1-x)^2}{x}\right] \\ P_{gg}^{(0)}(x) &= 2C_A\left[\frac{x}{(1-x)_+} + \frac{1-x}{x} + x(1-x)\right] + \delta(1-x)\frac{11C_A - 4N_f T_R}{6} \end{aligned} \tag{1.27}$$

where $C_A = N_c$.

### 1.3.4 Anomalous dimensions

As evident from eq. (1.21), DGLAP evolution is given by integro-differential equations. The convolution in the $z$ variable can be cast into multiplication utilizing the Mellin transform. It is defined by

$$f_j^{\omega}(\omega,t) = \int_0^1 \mathrm{d}x\; x^{\omega-1} f_j(x,t) \tag{1.28}$$

for a parton of type $j$. The Mellin transform expresses the parton density in terms of its Mellin moments. This mathematical tool provides a more convenient and analytical framework for studying the evolution of parton distributions. We define singlet quark density

$$\Sigma(x,t) = \sum_i \left[q_i(x,t) + \overline{q}_i(x,t)\right], \tag{1.29}$$

and in Mellin space, the DGLAP equation reads

$$t\frac{\partial}{\partial t}\begin{pmatrix}\Sigma(\omega,t)\\ g(\omega,t)\end{pmatrix} = \frac{\alpha_s(t)}{2\pi}\begin{pmatrix}\gamma_{qq}\left(\omega\right) & 2N_f\gamma_{qg}\left(\omega\right)\\ \gamma_{gq}\left(\omega\right) & \gamma_{gg}\left(\omega\right)\end{pmatrix}\begin{pmatrix}\Sigma(\omega,t)\\ g(\omega,t)\end{pmatrix}, \tag{1.30}$$

where the anomalous dimensions $\gamma_{ab}$ is given by Mellin transform of the splitting function

$$\gamma_{ab}(\omega) = \int_0^1 \mathrm{d}x x^{\omega-1} P_{ab}(x). \tag{1.31}$$

We see from eq. (1.30) equation in Mellin space becomes a differential equation. The LO anomalous dimensions have the following expression

$$\begin{aligned}
\gamma_{qq}^{(0)} &= C_F\left[\frac{3}{2} + \frac{1}{(\omega)(\omega+1)} + 2\psi(1) - 2\psi(\omega+1)\right]\\
\gamma_{gq}^{(0)} &= C_F\frac{\omega^2+\omega+2}{\omega(\omega^2-1)}\\
\gamma_{qg}^{(0)} &= T_R\frac{\omega^2+\omega+2}{(\omega)(\omega+1)(\omega+2)}\\
\gamma_{gg}^{(0)} &= 2C_A\left[\frac{11}{12} + \frac{1}{\omega(\omega-1)} + \frac{1}{(\omega+1)(\omega+2)} + \psi(1) - \psi(\omega+1)\right] - \frac{N_f}{3N_C^2}
\end{aligned} \tag{1.32}$$

To better understand the connection between the DGLAP calculation and the anomalous dimensions obtained from the renormalization group equations, we will explore collinear factorization in the section 1.4.5.

## 1.4 Gluon evolution at small x

Before entering the discussion at small x region, we need to clarify the complicated situation of different variables involved in various evolutions. We start this section with a schematic description of the relevant dominant series expansions and outline the general picture, leaving the detailed calculation to the following subsections.

As we introduced in the DGLAP evolution, the divergent term in eq. (1.18) arises when a gluon is emitted parallel to the quark with transverse momentum ($k_T \to 0$), this singularity is then referred to as the collinear divergence. Accompanied by the splitting functions $P_{ab}$, the divergence is the main construct of the DGLAP equation kernel. We say the DGLAP equation is the consequence of the collinear limit.

From a kinematical perspective, the collinear limit corresponds to a strong ordering on the transverse momenta of the gluons exchanged in the gluon ladder when $Q^2 \to \infty$, see fig. 1.10,

$$Q^2 \gg k_{1\perp}^2 \gg k_{2\perp}^2 \gg \cdots \gg k_{n\perp}^2. \tag{1.33}$$

One can perform integration over the transverse momenta in the $n$-rung ladder. Taking into account the strong ordering in the transverse momenta, this results in the nested integrals, which can be performed to obtain the leading logarithmic contribution

$$\int_{\mu^2}^{Q^2} \frac{\mathrm{d}k_{1\perp}^2}{k_{1\perp}^2}\alpha_s \int_{\mu^2}^{k_{1\perp}^2} \frac{\mathrm{d}k_{2\perp}^2}{k_{2\perp}^2}\alpha_s \int_{\mu^2}^{k_{2\perp}^2} \frac{\mathrm{d}k_{3\perp}^2}{k_{3\perp}^2}\alpha_s \cdots \int_{\mu^2}^{k_{n-1\perp}^2} \frac{\mathrm{d}k_{n\perp}^2}{k_{n\perp}^2}\alpha_s \sim \left(\alpha_s \ln \frac{Q^2}{\mu^2}\right)^n . \tag{1.34}$$

in the large $Q^2$ limit, where we adopt the a frozen $\alpha_s$ for simplicity. We see that the large logarithms $\left(\alpha_s \ln \frac{Q^2}{\mu^2}\right)^n$ are the dominant terms in the collinear limit. This is an important observation. As we discussed briefly in section 1.2.1 on the asymptotic freedom, we see this large logarithm $\ln Q^2$ appears with coupling constant $\alpha_s$. In collinear limit $\alpha_s \ln Q^2 \sim 1$, we need to include all the terms $(\alpha_s \ln Q^2),\ (\alpha_s \ln Q^2)^2,\ (\alpha_s \ln Q^2)^3,\ \ldots$. The resummation is developed to account for such behavior and probes the all-order structure of this expansion. The leading order (LO) DGLAP evolution resums the series $(\alpha_s \ln Q^2)^n$ and the next-to-leading order (NLO) DGLAP is responsible for the series $\alpha_s(\alpha_s \ln Q^2)^n$.

However, now we also can spot the existence of a $1/x$ term in $P_{gg}$ function eq. (1.27), what would happen if we investigate the evolution behavior when $x \to 0$?

In order to study limit $x \to 0$, it is useful to examine the DGLAP equation in terms

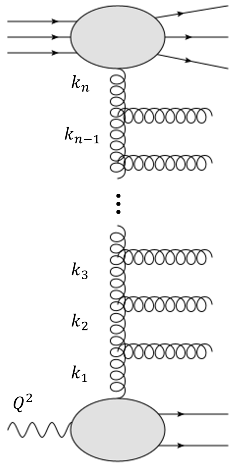


**Figure 1.10.** A strong ordering on the transverse momenta of the gluon ladder in the collinear limit.

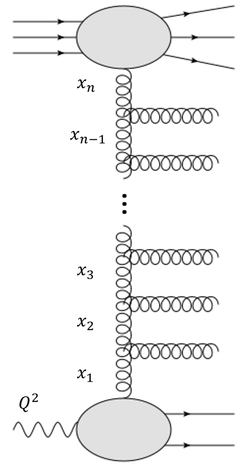


**Figure 1.11.** A strong ordering on the longitudinal momentum fractions of the gluon ladder in the high energy limit.

of the derivative of $xg(x, Q^2)$ over $Q^2$,

$$f(x, Q^2) = x\frac{\mathrm{d}g(x, Q^2)}{\mathrm{d}Q^2}. \tag{1.35}$$

The function $f(x, Q^2)$ is referred to as the unintegrated gluon density. We follow [64] for the derivation of the logarithm series below. We start to solve the gluonic part of the DGLAP equation in the differential form

$$Q^2 x\frac{\mathrm{d}g(x, Q^2)}{\mathrm{d}Q^2} = \alpha_s \int_x^1 \mathrm{d}z P_{gg}(z)\frac{x}{z} g\left(\frac{x}{z}, Q^2\right). \tag{1.36}$$

By iterating from a simple initial condition

$$f^{(0)}(x, Q^2) = \frac{1}{Q^2}\Theta(1-x)\Theta(Q^2-\mu^2), \tag{1.37}$$

we obtain the first order iteration result

$$\begin{aligned} Q^2 f^{(1)}(x, Q^2) &= \alpha_s \int_x^1 \mathrm{d}z P_{gg}(z) \int^{Q^2} \mathrm{d}k^2 f^{(0)}\left(\frac{x}{z}, k^2\right) \\ &\approx \overline{\alpha}_s \int_x^1 \frac{\mathrm{d}z}{z} \int^{Q^2} \mathrm{d}k^2 f^{(0)}\left(\frac{x}{z}, k^2\right) \\ &= \overline{\alpha}_s \ln\frac{1}{x} \ln\frac{Q^2}{\mu^2}, \end{aligned} \tag{1.38}$$

where $\overline{\alpha}_s = \alpha_s C_A/\pi$. The approximation in the second line is a direct result of the small

$x$ limit. The second-order contribution by iteration is

$$Q^2 f^{(2)}(x, Q^2) = \overline{\alpha}_s \int_x^1 \frac{\mathrm{d}z}{z} \int^{Q^2} \mathrm{d}k^2 f^{(1)}\left(\frac{x}{z}, k^2\right) = \frac{\overline{\alpha}_s^2}{(2!)^2} \ln^2 \frac{1}{x} \ln^2 \frac{Q^2}{\mu^2}. \tag{1.39}$$

Eventually, we get the $n$th-order contribution

$$Q^2 f^{(n)}(x, Q^2) = \frac{1}{(n!)^2} \left(\overline{\alpha}_s \ln \frac{1}{x} \ln \frac{Q^2}{\mu^2}\right)^n. \tag{1.40}$$

A direct observation is that large logarithm $\ln 1/x$ contributes along with running coupling $\overline{\alpha}_s$ and another large logarithm $\ln Q^2/\mu^2$. Such behavior is named a double-logarithmic (DL) series.

In the massless case of DIS, when the center of mass energy squared $W^2$ of the photon-proton subprocess is high enough ($W^2 \gg Q^2$),

$$W^2 = \frac{Q^2(1-x)}{x} \simeq \frac{Q^2}{x} \qquad \Longrightarrow \qquad x \simeq \frac{Q^2}{W^2} \ll 1, \tag{1.41}$$

we enter the small $x$ regime. Now with the small $x$ evolution we discussed above and also eq. (1.27) in mind, we see $P_{qq}$ is constant but $P_{gg}$ grows as $1/x$. A gluon ladder with gluon splittings dominates over the quark ladders (with gluon rungs) in such a process and we have a strong ordering on the longitudinal momentum fraction $x$, see fig. 1.11,

$$x \ll x_1 \ll x_2 \ll \cdots \ll x_n. \tag{1.42}$$

We will see the calculation of the ladder in section 1.4.2.3 and the reason why the ladder is of particular interest later in this section.

A rough schematic division of various dominant evolutions is shown in fig. 1.12.

- The DGLAP equation is responsible for the $Q^2$ evolution from the low to high $Q^2$ in the diagram.

- The BFKL equation, which will be the main focus for the rest of the section, corresponds to the small $x$ evolution.

- The double leading logarithm approximation (DLLA), which combines both logarithm series in the leading order, is in the diagonal direction in the figure.

- At low $Q^2$, we have the non-perturbative region. In perturbative QCD phenomenology, this long range contribution is usually renormalized into a quantity in the factorization scale as we discussed for eq. (1.19).

- The saturation region [65] is where gluons are highly squeezed in a confined nucleus. Besides the common $g \to gg$ splitting, they also start to overlap and recombine and thus lead to non-linear dynamics. This is out of the scope of our discussion in this work.

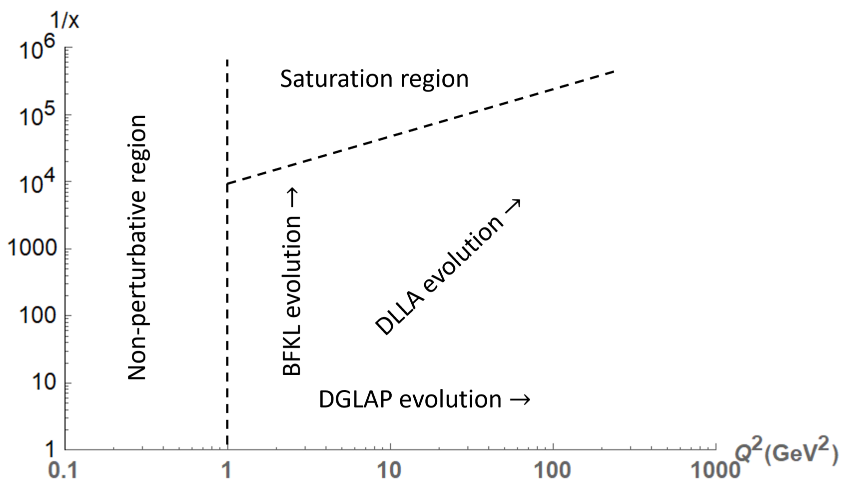


**Figure 1.12.** Schematic representation of different types of evolutions in $(x, Q^2)$ space.

### 1.4.1 Regge theory and Pomeron

As we briefly discussed for fig. 1.12, at small $x$, the dominant evolution is the BFKL equation. Historically, the BFKL formalism is motivated by a pre-QCD theory, the Regge theory, that was developed with scattering matrices and was a prevailing approach to describe experimental observations. It is useful to introduce the Regge theory and the Regge limit, before we apply the idea into BFKL. The Regge region refers to the high energy region, where the center of mass energy $s \gg |t|$. Again, we show the definitions of the Mandelstan variables here with notations consistent to fig. 1.13,

$$\begin{aligned} s &= (p_1 + p_2)^2 \\ u &= (p_1 - p_4)^2 \\ t &= (p_1 - p_3)^2 \end{aligned} \tag{1.43}$$

In a t channel scattering like fig. 1.13, we call the intermediate exchanged particle with mass $M$ and spin $J$ reggeized if the amplitude $\mathcal{A}$ is related to the center of mass energy

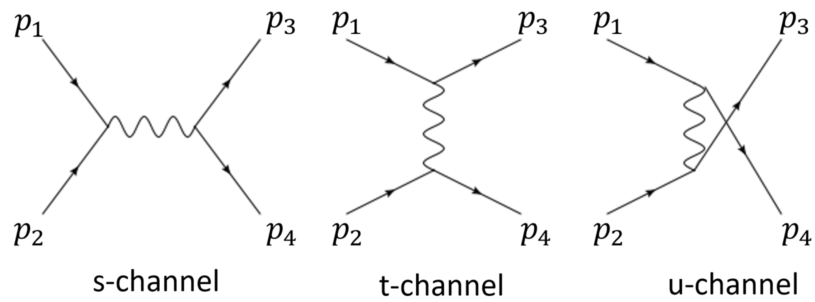


**Figure 1.13.** Diagrams corresponding to different channels in 2 particle scattering.

$s$ as

$$\mathcal{A} \propto s^{\alpha(t)}, \tag{1.44}$$

where the function $\alpha(t)$ is called the Regge trajectory and is often a linear function of $t$ with $\alpha(M^2) = J$. A Pomeron, named after the inventor Pomeranchuk, refers to a trajectory corresponding to the exchange of the quantum numbers of the vacuum and the intercept $\alpha(0) > 1$. The corresponding cross section has the power growth in energy

$$\sigma \sim s^{\alpha(0)-1}. \tag{1.45}$$

In the following discussions, we will not burden the readers with topics or observations based on these Regge trajectories. Instead, we'd like to focus on the derivations and properties of the scatterings based on reggeized gluons, to see especially the dominant contribution with the large logarithm term $\ln(1/x)$ (or equivalently, $\ln s$), that leads us to the famous Balitsky-Fadin-Kuraev-Lipatov (BFKL) equation [13–20]. In the next subsection, we will explore the all order structure of $(\alpha_s \ln s)^n$ series, i.e., the calculation on the diagram set including an infinite number of all contributing Feynman diagrams, following the derivation in [66].

## 1.4.2 From the tree diagram to the ladders of gluons

### 1.4.2.1 The Cutkosky rule

Before moving to investigate the actual scattering diagrams, we need to prepare ourselves with some basic knowledge of the scattering amplitude. Suppose we have the in-state $|a\rangle$ and the out-state $|b\rangle$, the unitary Lorentz invariant $S$ matrix is defined as

$$S_{ab} = \langle b|a\rangle \tag{1.46}$$

The scattering amplitude $\mathcal{A}$ is related to the $S$-matrix by

$$S_{ab} = \delta_{ab} + i(2\pi)^4\delta^4\left(\sum_a p_a - \sum_b p_b\right)\mathcal{A}_{ab}, \tag{1.47}$$

where $p_a$ and $p_b$ are the momenta of the incoming and outgoing particles respectively. The Cutkosky rule is then given by the unitarity of the $S$-matrix,

$$2\Im\mathrm{m}\mathcal{A}_{ab} = (2\pi)^4\delta^4\left(\sum_a p_a - \sum_b p_b\right)\sum_c \mathcal{A}_{ac}A^\dagger_{ab}. \tag{1.48}$$

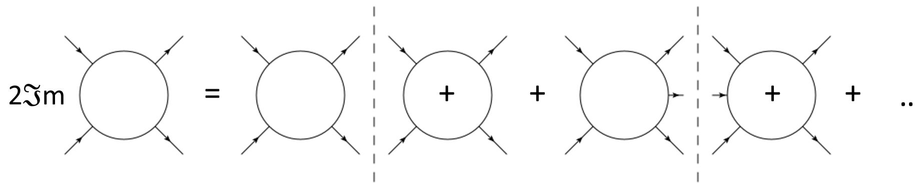


**Figure 1.14.** The Cutkosky rule for two-to-two particles scattering. The + signs denote the hermitian conjugate to the amplitude.

The visualization of the Cutkosky rule is shown in the fig. 1.14. The dashed cut in the figure means that we take intermediate particles on-shell and perform the integral over their phase space. When we consider the forward elastic amplitude, $A_{aa}$, we immediately see the optical theorem that relates the imaginary part of the forward scattering amplitude to the total cross section $\sigma_{\mathrm{tot}}$,

$$2\Im\mathrm{m}\mathcal{A}_{aa} = (2\pi)^4\sum_n \delta^4\left(\sum_f p_f - \sum_a p_a\right)|A_{a\to n}|^2 = F\sigma_{\mathrm{tot}}, \tag{1.49}$$

where the $F$ is the flux factor and $F \simeq 2s$ in the high energy limit.

#### 1.4.2.2 The tree, $O(\alpha_s)$ and $O(\alpha_s^2)$ diagrams

We begin with the first few lowest level diagrams of the elastic quark-quark scattering to see the $\alpha_s$ or $\alpha_s \ln(1/x)$ contributions. In terms of the setup of the calculation, we shall use the Sudakov parameters which are widely used in the high energy calculations. Sudakov parameters $\rho$ and $\lambda$ parameterize the momentum $k$ as

$$k^\mu = \rho p_1^\mu + \lambda p_2^\mu + k_\perp^\mu, \tag{1.50}$$

where $k_\perp^\mu$ is the momentum transverse to the incoming quarks momenta $p_1$ and $p_2$ which are lightlike.

From now on, we note this type of two-dimensional vector as the boldface $\mathbf{k}$. In the center-of-mass frame, the relevant four momenta are just

$$\begin{aligned}
p_1^\mu &= \left(\frac{\sqrt{s}}{2}, \frac{\sqrt{s}}{2}, \mathbf{0}\right) \\
p_2^\mu &= \left(\frac{\sqrt{s}}{2}, -\frac{\sqrt{s}}{2}, \mathbf{0}\right) \\
k^\mu &= \left((\rho+\lambda)\frac{\sqrt{s}}{2}, (\rho-\lambda)\frac{\sqrt{s}}{2}, \mathbf{k}\right).
\end{aligned} \tag{1.51}$$

We note the convention of the four vectors as follows. The first component is energy; the second component is longitudinal (the direction of the parental hadron) in the 3 direction; the last two is the transverse component.

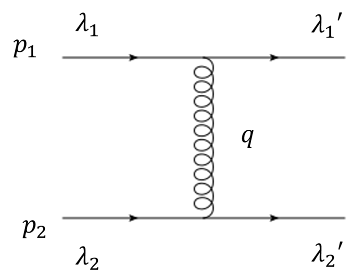


**Figure 1.15.** The born level diagram of the quark-quark elastic scattering.

As in fig. 1.15, the incoming quarks carry the helicities $\lambda_1$, $\lambda_2$, with a gluon exchanged with momentum $q$. The outgoing quarks carry the momentum $p_1 - q$, $p_2 + q$ and helicities $\lambda_{1'}$, $\lambda_{2'}$. To brief the calculation rules, we take the upper line of the fig. 1.15 for an example

$$-ig\overline{u}_{\lambda_1'}(p_1 - q)\gamma^\mu u_{\lambda_1}(p_1)\tau_{ij}^a, \tag{1.52}$$

where $\tau^a$ is the generator of the color group in the fundamental representation and $g^2 = 4\pi\alpha_s$. With the Gordon identity, this yields

$$-\frac{ig}{2m_p}\overline{u}_{\lambda_1'}(p_1 - q)\left[(2p_1 - q)^\mu + 2iS^{\mu\nu}q_\nu\right]u_{\lambda_1}(p_1)\tau_{ij}^a, \tag{1.53}$$

where the normalization is $\overline{u}_{\lambda_1'}(p)u_{\lambda_1}(p) = 2m_p\delta_{\lambda_1'\lambda_1}$ and the spin matrix $S^{\mu\nu} = i[\gamma^\mu, \gamma^\nu]/4$.

The Regge limit, $s \gg -t = -q^2$, implies we can approximate that $p_1^\mu \gg q_1^\mu$, thus

$$-ig\bar{u}_{\lambda_1'}(p_1 - q)\gamma^\mu u_{\lambda_1}(p_1)\tau_{ij}^a \simeq -2igp_1^\mu \delta_{\lambda_1'\lambda_1}\tau_{ij}^a. \tag{1.54}$$

Therefore, we can derive the amplitude of the Born diagram

$$\begin{aligned}\mathcal{A}_0^{(8)} &= 2g^2 p_1^\mu \frac{g_{\mu\nu}}{q^2} 2p_2^\nu \delta_{\lambda_{1'}\lambda_1}\delta_{\lambda_{2'}\lambda_2} G_0^{(8)} \\ &= 8\pi\alpha_s \frac{s}{t}\delta_{\lambda_{1'}\lambda_1}\delta_{\lambda_{2'}\lambda_2} G_0^{(8)},\end{aligned} \tag{1.55}$$

where the coupling on the vertex $g^2 = 4\pi\alpha_s$ and the color octet factor $G_0^{(8)} = \tau^a \otimes \tau^a$. However, the Pomeron is only realized in QCD from color singlet exchanges, which can be achieved in QCD starting from a two-gluon exchange. To regularize the infra-red divergence, we shall abide by the on-shell condition and color confinement of the incoming quarks and thus a colorless state is required.

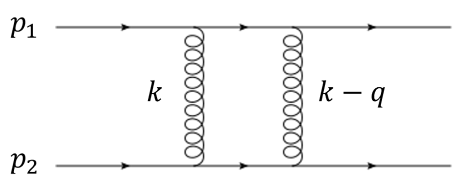


**Figure 1.16.** The $O(\alpha_s)$ box diagram.

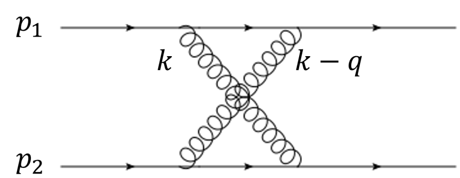


**Figure 1.17.** The $O(\alpha_s)$ crossed box diagram.

The lowest-order contribution to the color singlet exchange comes from the box and crossed-box diagrams with two gluons being exchanged as shown in figs. 1.16 and 1.17.

$$\begin{aligned}\mathcal{A}_1 &= 4i\alpha_s^2 s \delta_{\lambda_{1'}\lambda_1}\delta_{\lambda_{2'}\lambda_2} G_0 \int \frac{\mathrm{d}^2\mathbf{k}}{\mathbf{k}^2 (\mathbf{k} - \mathbf{q})^2} \\ &= \frac{16i\pi^2}{N_C}\alpha_s \frac{s}{t}\delta_{\lambda_{1'}\lambda_1}\delta_{\lambda_{2'}\lambda_2} G_0 \epsilon_G(t)\end{aligned} \tag{1.56}$$

where $\epsilon_G(t)$ is define as

$$\epsilon_G(t) = \frac{N_C\alpha_s}{4\pi^2}\int \frac{\mathrm{d}^2\mathbf{k}\ t}{\mathbf{k}^2 (\mathbf{k} - \mathbf{q})^2}, \quad (t = -\mathbf{q}^2). \tag{1.57}$$

Notice this is infra-red divergent. This divergence arises from the underlying condition that the external quarks are on mass-shell. However, in practice, this is not concerning as the quarks are only scattered while bounded inside hadrons and the quarks are slightly off-shell. Nevertheless, it turns out the integral equation in section 1.4.2.3 of our vital interest is free from singularities. Therefore, we will not regularize this term explicitly. In addition, we note that there is no $\ln s$ term associated in eq. (1.56).

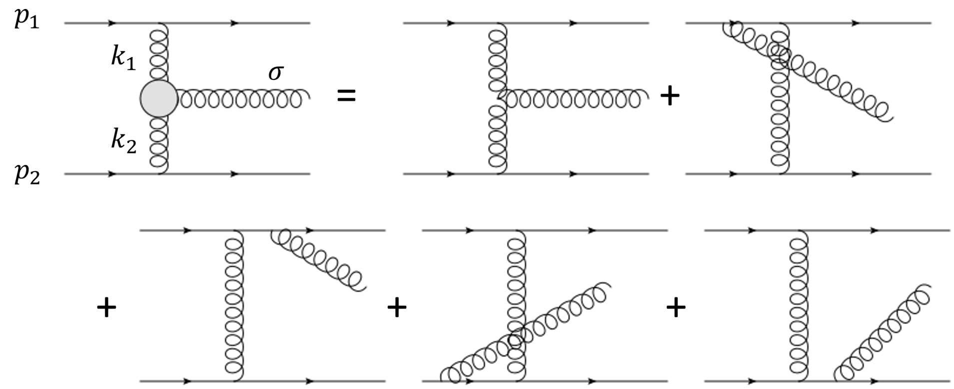


**Figure 1.18.** The $O(\alpha_s^2)$ gluon-splitting diagrams. The blob on the left-hand side represents the effective vertex, it is the summation of all contributions from the ride-hand side diagrams.

The two-loop amplitude with two gluon exchanges consists of 25 ($5 \times 5$) diagrams. From the Cutkosky rule, it is just the product of all five diagrams with an extra gluon emission in the r.h.s of fig. 1.18, and their conjugate (the momentum of the emitted gluon is $\mathbf{q}$). Leaving the color factor aside for now, we can obtain the amplitude from all the diagrams where two incoming particles scatter into three outgoing particles,

$$\mathcal{A}^{\sigma}_{2\to 3} = -2isg^3 \frac{\delta_{\lambda_{1'}\lambda_1} 2p_1^{\mu}}{\mathbf{k}_1^2} \Gamma^{\sigma}_{\mu\nu}(k_1, k_2) \frac{\delta_{\lambda_{2'}\lambda_2} p_2^{\nu}}{\mathbf{k}_2^2} \tag{1.58}$$

The gauge-invariant Lipatov effective vertex $\Gamma^{\sigma}_{\mu\nu}(k_1, k_2)$ sums the effects of all types of gluon emission, as depicted in fig. 1.18

$$\Gamma^{\sigma}_{\mu\nu}(k_1, k_2) = \frac{2p_{2\mu}p_{1\nu}}{s}\left[\left(\frac{2p_2k_1}{s} + \frac{2\mathbf{k}_1^2}{p_1k_2}\right)p_1^{\sigma} + \left(\frac{2p_1k_2}{s} + \frac{2\mathbf{k}_2^2}{p_2k_1}\right)p_2^{\sigma} - (\mathbf{k}_1 + \mathbf{k}_2)^{\sigma}\right] \tag{1.59}$$

The idea of the effective vertex is an important step towards our goal of probing the all order structure of $(\alpha_s \ln s)^n$ series. It helps us reduce the efforts on counting and computing different gluon emission diagrams significantly. It is the starting point of the later discussion on the n-gluon ladder emissions.

From the above one can obtain the imaginary part of the amplitude is

$$\mathcal{A}_{2a} = i\frac{g_{\sigma\tau}}{2}\int \mathrm{d}\left(P.S.^3\right) \mathcal{A}^{\sigma}_{2\to 3}(k_1, k_2) \mathcal{A}^{\dagger\tau}_{2\to 3}(k_1 - q, k_2 - q)$$

$$= -i\frac{2N_c\alpha_s^3}{\pi^2}\delta_{\lambda_{1'}\lambda_1}\delta_{\lambda_{2'}\lambda_2}G_0 s\ln\left(\frac{s}{\mathbf{k}^2}\right)\int \mathrm{d}^2\mathbf{k}_1\mathrm{d}^2\mathbf{k}_2$$
$$\cdot\left[\frac{\mathbf{q}^2}{\mathbf{k}_1^2\mathbf{k}_2^2\left(\mathbf{k}_1-\mathbf{q}\right)^2\left(\mathbf{k}_2-\mathbf{q}\right)^2} - \frac{1}{\mathbf{k}_1^2\left(\mathbf{k}_1-\mathbf{k}_2\right)^2\left(\mathbf{k}_2-\mathbf{q}\right)^2} - \frac{1}{\mathbf{k}_2^2\left(\mathbf{k}_1-\mathbf{k}_2\right)^2\left(\mathbf{k}_1-\mathbf{q}\right)^2}\right]. \tag{1.60}$$

where the color factor is

$$\frac{1}{N}\mathrm{Tr}(\tau_a\tau_b)\mathrm{Tr}(\tau_c\tau_d)f_{acd}f_{bde} = N_c G_0, \tag{1.61}$$

with the $f_{acd}$ the color constants of the SU(3) color group.

The phase-space integral is given by

$$\mathrm{d}\left(P.S.^3\right) = \frac{1}{(2\pi)^5}\left(\frac{s}{2}\right)^2 \mathrm{d}\rho_1\mathrm{d}\rho_2\mathrm{d}\lambda_1\mathrm{d}\lambda_2\delta\left(-\lambda_1 s-\mathbf{k}_1^2\right)\delta\left(\rho s-\mathbf{k}_2^2\right)\delta\left(-\rho_1\lambda_2 s-(\mathbf{k}_1-\mathbf{k}_2)^2\right), \tag{1.62}$$

Note the $\rho$ and $\lambda$ are the Sudakov parameters. It is worth our notice that the amplitude includes $\ln s$ term starting from this order as evident from eq. (1.60).

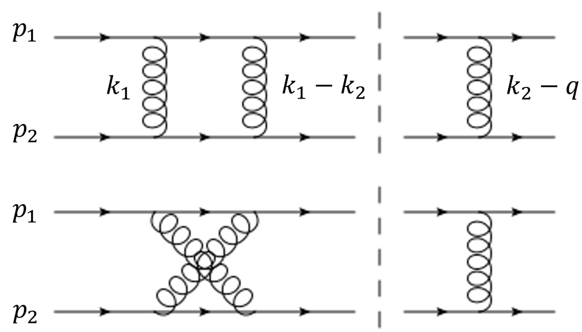


**Figure 1.19.** The $O(\alpha_s^2)$ three gluon exchange diagrams.

In addition to the real emissions, one needs to compute the virtual contributions. The three gluon exchange diagrams in fig. 1.19 give the virtual piece of contribution to the two-loop level

$$\mathcal{A}_{2b} = -i\frac{N_C\alpha_s^3}{\pi^2}\delta_{\lambda_{1'}\lambda_1}\delta_{\lambda_{2'}\lambda_2}G_0 s\ln\left(\frac{s}{\mathbf{k}^2}\right)\int \mathrm{d}^2\mathbf{k}_1\mathrm{d}^2\mathbf{k}_2\frac{1}{\mathbf{k}_1^2\left(\mathbf{k}_1-\mathbf{k}_2\right)^2\left(\mathbf{k}_2-\mathbf{q}\right)^2}. \tag{1.63}$$

The total imaginary amplitude with the above two contributions from real and virtual emissions combined is then

$$\Im m\mathcal{A}_2 = -\frac{2N_C\alpha_s^3}{\pi^2}s\delta_{\lambda_{1'}\lambda_1}\delta_{\lambda_{2'}\lambda_2}G_0 s\ln\left(\frac{s}{\mathbf{k}^2}\right)\int \mathrm{d}^2\mathbf{k}_1\mathrm{d}^2\mathbf{k}_2$$

$$\cdot \left[ \frac{\mathbf{q}^2}{\mathbf{k}_1^2 \mathbf{k}_2^2 \left(\mathbf{k}_1 - \mathbf{q}\right)^2 \left(\mathbf{k}_2 - \mathbf{q}\right)^2} - \frac{1}{2\mathbf{k}_1^2 \left(\mathbf{k}_1 - \mathbf{k}_2\right)^2 \left(\mathbf{k}_2 - \mathbf{q}\right)^2} - \frac{1}{2\mathbf{k}_2^2 \left(\mathbf{k}_1 - \mathbf{k}_2\right)^2 \left(\mathbf{k}_1 - \mathbf{q}\right)^2} \right]. \tag{1.64}$$

It is proven to be convenient to work in the Mellin space with the function $\mathcal{G}(\omega, \mathbf{k}_1, \mathbf{k}_2, \mathbf{q})$ as the Mellin conjugate to the amplitude

$$\int_1^\infty \mathrm{d}\left(\frac{s}{\mathbf{k}^2}\right) \left(\frac{s}{\mathbf{k}^2}\right)^{-\omega-1} \frac{\mathcal{A}\left(s,t\right)}{s} = 4i\alpha_s^2 \delta_{\lambda_{1'}\lambda_1} \delta_{\lambda_{2'}\lambda_2} G_0 \int \frac{\mathrm{d}^2\mathbf{k}_1 \mathrm{d}^2\mathbf{k}_2}{\mathbf{k}_2^2 \left(\mathbf{k}_1 - \mathbf{q}\right)^2} \mathcal{G}(\omega, \mathbf{k}_1, \mathbf{k}_2, \mathbf{q}). \tag{1.65}$$

Therefore, we can derive the leading order result

$$\mathcal{G}^{(0)}(\omega, \mathbf{k}_1, \mathbf{k}_2, \mathbf{q}) = \frac{1}{\omega} \delta^2(\mathbf{k}_1 - \mathbf{k}_2), \tag{1.66}$$

and the next-to-leading order

$$\mathcal{G}^{(1)}(\omega, \mathbf{k}_1, \mathbf{k}_2, \mathbf{q}) = -\frac{\overline{\alpha}_s}{2\pi\omega^2} \left[ \frac{\mathbf{q}^2}{\mathbf{k}_1^2 \left(\mathbf{k}_2 - \mathbf{q}\right)^2} - \frac{1}{2\left(\mathbf{k}_1 - \mathbf{k}_2\right)^2} \left( 1 + \frac{\mathbf{k}_2^2 \left(\mathbf{k}_1 - \mathbf{q}\right)^2}{\mathbf{k}_1^2 \left(\mathbf{k}_2 - \mathbf{q}\right)^2} \right) \right], \tag{1.67}$$

where $\overline{\alpha}_s = \alpha_s N_c / \pi$.

#### 1.4.2.3 The $2 \to n+2$ diagram and the integral equation

We now have all the necessary ingredients to be able to approach the calculation of the higher order diagrams and extract the dominant $(\alpha_s \ln s)^n$ terms.

The small $x$ or high energy limit implies the following strong ordering of the Sudakov parameters in the gluon ladder, see fig. 1.20

$$\begin{gathered} 1 \gg \rho_1 \gg \rho_2 \gg \cdots \gg \rho_{n+1} \gg \mathbf{k}^2/s, \\ 1 \gg |\lambda_{n+1}| \gg |\lambda_n| \gg \cdots \gg |\lambda_1| \gg \mathbf{k}^2/s, \end{gathered} \tag{1.68}$$

The amplitude of the $2 \to 2+n$ amplitude in fig. 1.20 is given by

$$\begin{aligned} \mathcal{A}_{2\to n+2} = i2sg^{n+2} \delta_{\lambda_{1'}\lambda_1} \delta_{\lambda_{2'}\lambda_2} G_0 \frac{i}{\mathbf{k}_1^2} \left(\frac{1}{\rho_1}\right)^{\epsilon_G\left(k_1^2\right)} \\ \cdot \prod_{i=1}^n \frac{2p_1^{\mu_i} p_2^{\nu_{i+1}}}{s} \Gamma^{\sigma_i}_{\mu_i \nu_{i+1}} \left(k_i, k_{i+1}\right) \frac{i}{\mathbf{k}_{i+1}^2} \left(\frac{\rho_i}{\rho_{i+1}}\right)^{\epsilon_G\left(k_{i+1}^2\right)}, \end{aligned} \tag{1.69}$$

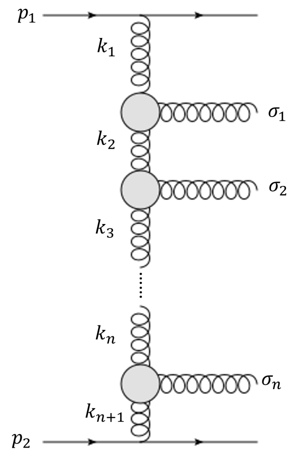


**Figure 1.20.** $2 \to 2 + n$ ladder diagram.

This ladder diagram is a critical step in the derivation. However, the rigorous calculation of this amplitude tends to be challenging and would take a great volume. We only summarize the pivot ideas and show comments as follows:

- In order to take all types of gluon exchanges into account, fig. 1.20 features effective replacements both for the vertices and gluon propagators.
- The blob in the ladder represents the Lipatov effective vertex, as we discussed in the last subsection. The amplitude for the ladder diagram with Lipatov effective vertices and bare gluons are given in [65].
- Furthermore, one also needs to include the loop corrections. The loop corrections are realized by replacing the bare gluon in the ladder with a nested superposition of the ladder with effective vertices and effective gluon propagators. For comparison, the bare gluon propagator in the Feynman gauge is given by

$$D_{\mu\nu}(k_i^2) = -i\frac{g_{\mu\nu}}{k_i^2}. \tag{1.70}$$

The gluon propagator as the $i$th section of the ladder that accounts for the loop corrections is

$$\begin{aligned} \tilde{D}_{\mu\nu}(s_i, k_i^2) &= \frac{ig_{\mu\nu}}{\mathbf{k}_i^2}\left(\frac{s_i}{\mathbf{k}^2}\right)^{\epsilon_G(k_i^2)} \\ &\simeq \frac{ig_{\mu\nu}}{\mathbf{k}_i^2}\left(\frac{\rho_{i-1}}{\rho_i}\right)^{\epsilon_G(k_i^2)}, \end{aligned} \tag{1.71}$$

where we take the approximation

$$\frac{s}{\mathbf{k}^2} = \frac{(k_{i-1} - k_{i+1})^2}{\mathbf{k}^2} \simeq -\frac{-\rho_{i-1}\lambda_{i+1}s}{\mathbf{k}^2} = \frac{\rho_{i-1}}{\rho_i}\frac{(\mathbf{k}_{i+1} - \mathbf{k}_{i-1})^2}{\mathbf{k}^2} \simeq \frac{\rho_{i-1}}{\rho}. \tag{1.72}$$

This above procedure is called the reggeization and corresponding gluons are reggeized gluons.

- The eq. (1.69) is called the multi-Regge exchange amplitude. This calculation is performed in [67] and also outlined in [68].
- Above is a remarkable result, in the sense that every vertex in the gluon ladder is the Lipatov effective vertex and the exchanged gluons in the $t$ channel are all reggeized gluons. It represents an effective summation over a huge number of Feynman diagrams with all sorts of gluon exchanges at the order of $(\alpha_s \ln s)^n$.

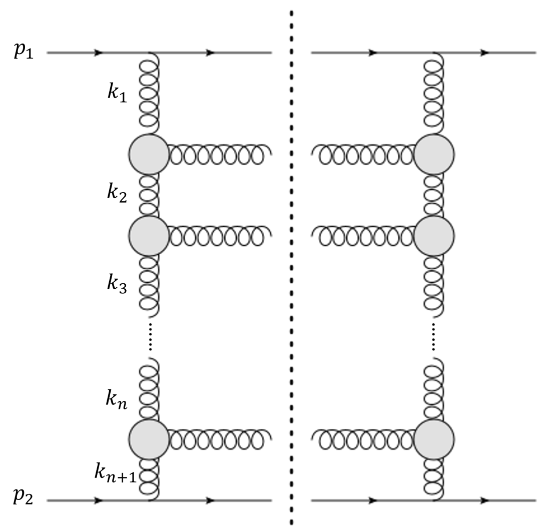


**Figure 1.21.** $2 \to 2 + n$ ladder with its conjugate separated by the Cutkosky cut.

The imaginary part of the $2 \to 2 + n$ amplitude, with a Cutkosky cut and the conjugate of a single ladder as illustrated in fig. 1.21, is then

$$\Im m\mathcal{A} = \frac{1}{2}\sum_{n=0}^{\infty}(-1)^n \int \mathrm{d}\left(P.S.^{(n+2)}\right)\left[\mathcal{A}_{2\to n+2}(k_1, \ldots, k_n)\,\mathcal{A}^{\dagger}_{2\to n+2}(k_1 - q, \ldots, k_n - q)\right], \tag{1.73}$$

where $\mathrm{d}\left(P.S.^{(n+2)}\right)$ means the integral over the phase space of the 2 quark lines and $n$ gluon lines that go through the Cutkosky cut,

$$\int \mathrm{d}\left(P.S.^{(n+2)}\right) = \frac{1}{2^{4n+3}\pi^{3n+2}} \prod_{i=1}^{n} \int_{\rho_i+1}^{1} \frac{\mathrm{d}\rho_i}{\rho_i} \prod_{j=1}^{n+1} \mathrm{d}^2\mathbf{k_j}\, \mathrm{d}\rho_{n+1}\, \delta\left(s\rho_{n+1} - \mathbf{k}^2\right). \tag{1.74}$$

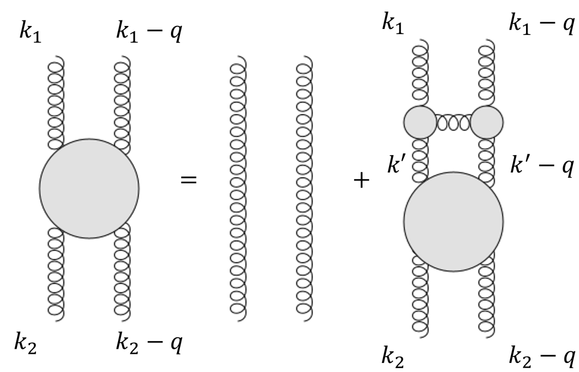


**Figure 1.22.** A Graphical depiction of the integral equation.

Now we are equipped with the knowledge of the contribution from the lowest order to the $n$th order. However, it is not practical to just sum them straightforwardly. Again, it turns out to be useful to work in the Mellin space and construct the integral evolution equation

$$\begin{aligned}
&\left[\omega - \epsilon_G(-\mathbf{k}_1^2) - \epsilon_G(-(\mathbf{k}_1 - \mathbf{q})^2)\right] \mathcal{G}(\omega, \mathbf{k}_1, \mathbf{k}_2, \mathbf{q}) \\
=&\delta^2(\mathbf{k}_1 - \mathbf{k}_2) - \frac{\overline{\alpha}_s}{2\pi} \int \mathrm{d}^2\mathbf{k}' \left[\frac{\mathbf{q}^2}{\mathbf{k}_1^2\left(\mathbf{k}' - \mathbf{q}\right)^2} - \frac{1}{\left(\mathbf{k}_1 - \mathbf{k}'\right)^2}\left(1 + \frac{\mathbf{k}'^2\left(\mathbf{k}_1 - \mathbf{q}\right)^2}{\mathbf{k}_1^2\left(\mathbf{k}' - \mathbf{q}\right)^2}\right)\right] \mathcal{G}(\omega, \mathbf{k}', \mathbf{k}_2, \mathbf{q}).
\end{aligned} \tag{1.75}$$

This integral equation is schematically represented in fig. 1.22. The first term on the right hand side stands for the case with no rungs on the ladder and the second term represents the effect of adding one extra rung to the ladder with the effective vertices embedded. One can check that the cancellation between the $\epsilon_G$ functions eliminates the infrared singularities. With replacing $\mathbf{k}' \to (\mathbf{k}_1 - \mathbf{k}')$, we can rewrite eq. (1.75) as

$$\begin{aligned}
\omega\mathcal{G}(\omega, \mathbf{k}_1, \mathbf{k}_2, \mathbf{q}) = \delta^2(\mathbf{k}_1 - \mathbf{k}_2) + \frac{\overline{\alpha}_s}{2\pi} \int \mathrm{d}^2\mathbf{k}' &\left\{ \frac{-\mathbf{q}^2}{\left(\mathbf{k}' - \mathbf{q}\right)^2 \mathbf{k}_1^2} \mathcal{G}(\omega, \mathbf{k}', \mathbf{k}_2, \mathbf{q}) \right. \\
&+ \frac{1}{\left(\mathbf{k}' - \mathbf{k}_1\right)^2} \left[\mathcal{G}(\omega, \mathbf{k}', \mathbf{k}_2, \mathbf{q}) - \frac{\mathbf{k}_1^2 \mathcal{G}(\omega, \mathbf{k}_1, \mathbf{k}_2, \mathbf{q})}{\mathbf{k}'^2 + \left(\mathbf{k}_1 - \mathbf{k}'\right)^2}\right]
\end{aligned} \tag{1.76}$$

$$+\frac{1}{\left(\mathbf{k}'-\mathbf{k}_1\right)^2}\left[\frac{\left(\mathbf{k}_1-\mathbf{q}\right)^2\mathbf{k}'^2\mathcal{G}(\omega,\mathbf{k}',\mathbf{k}_2,\mathbf{q})}{\left(\mathbf{k}'-\mathbf{q}\right)\mathbf{k}_1^2}-\frac{\left(\mathbf{k}_1-\mathbf{q}\right)^2\mathcal{G}(\omega,\mathbf{k}_1,\mathbf{k}_2,\mathbf{q})}{\left(\mathbf{k}'-\mathbf{q}\right)^2+\left(\mathbf{k}_1-\mathbf{k}'\right)^2}\right]\Bigg\}. \tag{1.77}$$

This is the Balitsky-Fadin-Kuraev-Lipatov (BFKL) equation [13–20] for non-forward scattering ($\mathbf{q}\neq 0$). It is also very useful to show the BFKL in forward scattering ($\mathbf{q}=0$),

$$\begin{aligned}\omega\mathcal{G}(\omega,\mathbf{k}_1,\mathbf{k}_2,\mathbf{0}) &= \delta^2(\mathbf{k}_1-\mathbf{k}_2)+\frac{\overline{\alpha}_s}{\pi}\int\frac{\mathrm{d}^2\mathbf{k}'}{\left(\mathbf{k}_1-\mathbf{k}'\right)^2}\\ &\cdot\left[\mathcal{G}(\omega,\mathbf{k}',\mathbf{k}_2,\mathbf{0})-\frac{\mathbf{k}_1^2}{\mathbf{k}'^2+\left(\mathbf{k}_1-\mathbf{k}'\right)^2}\mathcal{G}(\omega,\mathbf{k}_1,\mathbf{k}_2,\mathbf{0})\right].\end{aligned} \tag{1.78}$$

The above equations can be regarded as equations for the Green's function.

In the following, we shall be mostly interested in the forward case, $\mathbf{q}=0$. It will be useful to introduce the notation which uses the kernel $\mathcal{K}(\mathbf{k}',\mathbf{k}_1)$ in the integral equation, i.e.

$$\omega\mathcal{G}(\omega,\mathbf{k}_1,\mathbf{k}_2,\mathbf{0})=\delta^2(\mathbf{k}_1-\mathbf{k}_2)+\int\mathrm{d}^2\mathbf{k}'\mathcal{K}(\mathbf{k}',\mathbf{k}_1)\mathcal{G}(\omega,\mathbf{k}',\mathbf{k}_2,\mathbf{0}), \tag{1.79}$$

where the kernel includes namely both virtual and real part

$$\begin{aligned}\mathcal{K}(\mathbf{k}',\mathbf{k}_1) &= \mathcal{K}_{\mathrm{virtual}}(\mathbf{k}',\mathbf{k}_1)+\mathcal{K}_{\mathrm{real}}(\mathbf{k}',\mathbf{k}_1)\\ &= \epsilon_G(\mathbf{k}_1)\delta^2(\mathbf{k}_1-\mathbf{k}')+\frac{\overline{\alpha}_s}{\pi}\frac{1}{\left(\mathbf{k}'-\mathbf{k}_1\right)^2}.\end{aligned} \tag{1.80}$$

### 1.4.3 The solution to the BFKL equation

#### 1.4.3.1 The solution formed in the Mellin space

In this subsection, we will show how to obtain the solution of the BFKL equation. But before we start the derivation, we shall introduce the BFKL equation in a slightly different context. The BFKL equation in the last subsection governs over the gluon Green's function $\mathcal{G}$. Whereas we intend to extend the objects to the unintegrated gluon density $f$ which can receive more contribution from process-dependent experimental input.

For a typical two particles ($A$ and $B$) scattering with scales $Q_1, Q_2$ , the high energy factorization allows us to write the cross section, as illustrated in fig. 1.23, in the form

$$\sigma=\int\frac{\mathrm{d}\omega}{2\pi i}\int\frac{\mathrm{d}^2\mathbf{k}_1}{k_1^2}\frac{\mathrm{d}^2\mathbf{k}_2}{k_2^2}\left(\frac{s}{s_0}\right)^{\omega}\phi^A(Q_1,\mathbf{k}_1)\mathcal{G}(\omega,\mathbf{k}_1,\mathbf{k}_2)\phi^B(Q_2,\mathbf{k}_2), \tag{1.81}$$

where $s_0$ is the energy scale by choice (for symmetric choice, $s_0 = Q_1Q_2$). We will elaborate more on the high energy factorization in section 1.4.5. For a quick summary now, the impact factors $\phi^A$ and $\phi^B$ $(A, B = q, \overline{q}, g, \gamma)$ stem from the all the couplings between the Pomeron and the incoming partons, i.e. partons in the incoming hadron. Meanwhile, the Green function $\mathcal{G}(\omega, \mathbf{k}_1, \mathbf{k}_2)$ represents the Pomeron effect, i.e. all the exchanges and emissions of the reggeized gluons. Note we have omitted the possible polarizations of particles A and B here for convenience.

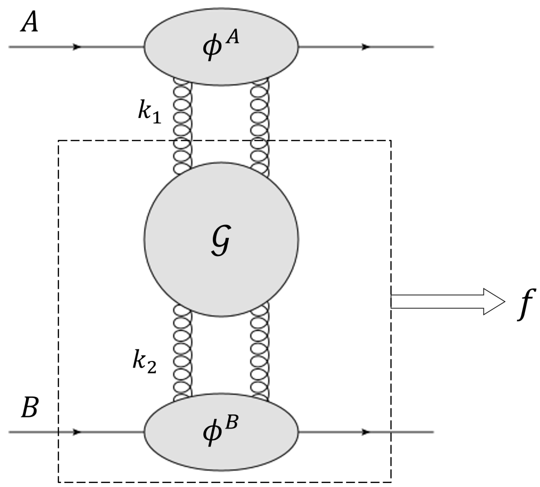


**Figure 1.23.** The high energy factorization cross section for scattering of two particles $A$ and $B$. The unintegrated gluon density $f$ in particle B is the convolution between the gluon Green's function and one of the impact factors.

The unintegrated gluon density $\overline{f}(\omega, \mathrm{k})$ is defined as the convolution between the Green function and one of the impact factors, as depicted by the box in fig. 1.23,

$$\overline{f}(\omega, \mathbf{k}) = \int \frac{\mathrm{d}^2\mathbf{k}_2}{\mathbf{k}_2^2} \mathcal{G}(\omega, \mathbf{k}, \mathbf{k}_2)\phi^B(Q_2, \mathbf{k}_2). \tag{1.82}$$

We can replace the dependency of the center-of-mass energy $s$ in $f$ with $x$ and apply ~~the~~ the Mellin transform,

$$\overline{f}\,(\omega) = \int_0^1 \frac{\mathrm{d}x}{x} x^\omega f(x). \tag{1.83}$$

Rewriting the BFKL equation in $(x, \mathbf{k})$ space, with the assumptions that $f(x, \mathbf{k})$ is independent of the angular position of the transverse momentum k, we get the BFKL equation that appears more frequently in the literature,

$$f(x, k^2) = f^{(0)}(x, k^2) + \overline{\alpha}_s \int_x^1 \frac{\mathrm{d}z}{z} \int \frac{\mathrm{d}^2q}{\pi q^2} \left[ f\left(\frac{x}{z}, k'^2\right) - \Theta(k^2 - q^2) f\left(\frac{x}{z}, k^2\right)\right], \tag{1.84}$$

where $\mathbf{k}' = \mathbf{k} + \mathbf{q}$ as illustrated by the gluon splitting in fig. 1.24, with a notation for the squared transverse momentum $k^2 = \mathbf{k}^2$. $\Theta(k^2 - q^2)$ is the Heaviside function. The $f^{(0)}(x, k^2)$ is a process-dependent input function and is usually fitted to obtain the best description of the experimental data. We shall discuss the forms of the input and the comparison with the experimental data in chapter 3. Note also that sometimes in the literature, one can also encounter the rescaled unintegrated gluon density $\hat{F}(x, k^2) = f(x, k^2)/k^2$.

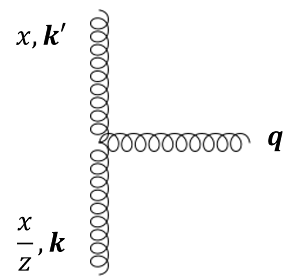


**Figure 1.24.** The gluon splitting on the gluon ladder.

To solve the BFKL equation, we begin by going back to the $(\omega, k^2)$ space,

$$\overline{f}(\omega, k^2) = \overline{f}^{(0)}(\omega, k^2) + \overline{\alpha}_s \int \frac{\mathrm{d}^2 q}{\pi q^2} \int_0^1 \frac{\mathrm{d}z}{z} z^{\omega} \left[ \overline{f}\left(\omega, k'^2\right) - \Theta(k^2 - q^2) \overline{f}\left(\omega, k^2\right) \right]. \quad (1.85)$$

where the integration $\int_0^1 \frac{\mathrm{d}z}{z} z^{\omega}$ in this case simply gives the result $1/\omega$. Similar to $\omega$ is a Mellin conjugate to $x$, we can take the Mellin transform of the $k^2$ and introduce its Mellin conjugate variable $\gamma$,

$$\overline{f}(\omega, k^2) = \frac{1}{2\pi i} \int_{c-i\infty}^{c+\infty} d\gamma \left(k^2\right)^{\gamma - 1} \tilde{f}(\omega, \gamma). \quad (1.86)$$

Consequently, the BFKL equation is unfolded in an algebraic form,

$$\tilde{f}(\omega, \gamma) = \tilde{f}^{(0)}(\omega, \gamma) + \frac{\overline{\alpha}_s}{\omega} \chi(\omega, \gamma) \tilde{f}(\omega, \gamma), \quad (1.87)$$

where the kernel in double Mellin space has the form

$$\chi(\omega, \gamma) = \int \frac{\mathrm{d}^2 q}{\pi q^2} \left[ \left( \frac{k'^2}{k^2} \right)^{\gamma - 1} - \Theta\left(k^2 - q^2\right) \right]. \quad (1.88)$$

Performing the substitution $k^2 = q^2 u$ when $k^2 \geqslant q^2$ and $q^2 = k^2 u$ when $k^2 < q^2$, we get

$$
\begin{aligned}
\chi &= \int \frac{\mathrm{d}\phi}{2\pi} \int_0^1 \frac{\mathrm{d}u}{u} \left[ \left(1 + 2\sqrt{u}\cos\phi + u\right)^{\gamma-1} (1 + u^{1-\gamma}) - 1 \right] \\
&= \int_0^1 \frac{\mathrm{d}u}{u} \left[ {}_2F_1(1-\gamma, 1-\gamma; 1; u)(1 + u^{1-\gamma}) - 1 \right] \\
&= 2\psi(1) - \psi(\gamma) - \psi(1-\gamma). \qquad (1.89)
\end{aligned}
$$

Here, the ${}_2F_1$ is the hypergeometric function and $\psi$ is the polygamma function. This function $\chi(\gamma)$ is the well-known LL BFKL eigenvalue.

Note that the LL BFKL eigenvalue only depends on the variable $\gamma$, since this is the consequence of the fact that the BFKL kernel only depends on the transverse momenta and not the longitudinal momentum fractions. We shall see that if one considers the effects of the energy scale $s_0$ effects or the kinematic constraints on gluon splitting, the $\omega$ dependency will be included in the kernel eigenvalue. We will discuss this in the later chapters when we introduce the concept of the resummation.

The LL solution to the BFKL equation in the Mellin space is thus given by

$$
\tilde{f}(\omega, \gamma) = \frac{\omega \tilde{f}^{(0)}(\omega, \gamma)}{\omega - \overline{\alpha}_s \chi(\gamma)}. \qquad (1.90)
$$

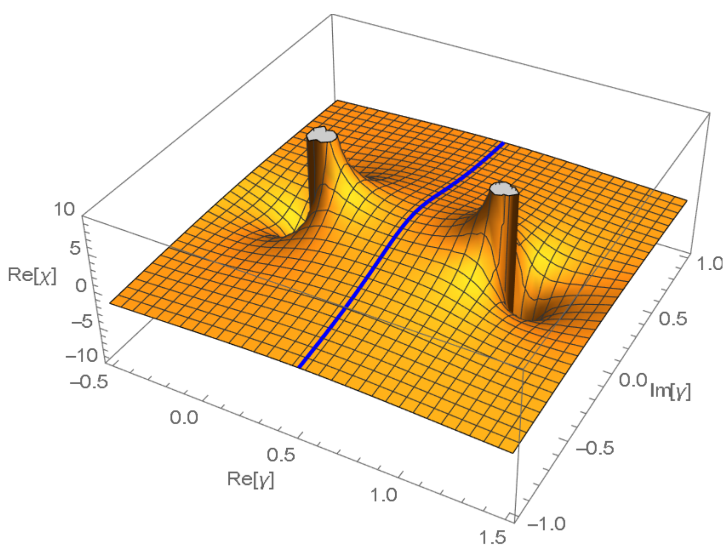


**Figure 1.25.** The real part of the LL BFKL kernel $\chi(\gamma)$ in complex plane of $\gamma$. The blue curve indicates the integration contour through the saddle point.

Realizing that denominator in eq. (1.90) clearly indicates a singularity in the $\omega$

integration, we can inverse the Mellin transform to the $(x, k^2)$ space,

$$f(x,k^2) = \int \frac{\mathrm{d}\gamma}{2\pi i} \exp\left[\overline{\alpha}_s \chi(\gamma) \ln\frac{1}{x} + \gamma \ln\frac{k^2}{s_0}\right] \cdot \overline{\alpha}_s \chi(\gamma) \tilde{f}^{(0)}(\gamma). \tag{1.91}$$

In the small $x$ limit, the $\ln 1/x$ dominates and the saddle point at $\gamma = 1/2$ makes the major contribution to the integration as illustrated in fig. 1.25, thus in the saddle point approximation,

$$f(x,k^2) \sim x^{-\overline{\alpha}_s \chi\left(\frac{1}{2}\right)}. \tag{1.92}$$

This exponential behavior corresponds to the Reggeized cross section in eq. (1.45) The $\omega_0 = \overline{\alpha}_s \chi\left(\frac{1}{2}\right) = 4 \ln 2\, \overline{\alpha}_s$ plays a role as the intercept of the Regge trajectory.

The next-to-leading order kernel in QCD is known, [21, 22]

$$\begin{aligned} \chi_1(\gamma) = & -\frac{b}{2}\chi_0^2(\gamma) - \frac{1}{4}\chi_0''(\gamma) - \frac{1}{4}\left(\frac{\pi}{\sin\pi\gamma}\right)^2 \frac{\cos\pi\gamma}{3(1-2\gamma)} \\ & \cdot \left[11 + 4\frac{T_R N_f}{N_c^3} + \frac{(1 + 2T_R N_f/N_c^3)\gamma(1-\gamma)}{(1+2\gamma)(3-2\gamma)}\right] \\ & + \left(\frac{67}{36} - \frac{\pi^2}{12} - \frac{5 T_R N_f}{9 N_c}\right)\chi_0(\gamma) + \frac{3}{2}\xi(3) + \frac{\pi^2}{4\sin\pi\gamma} - \Phi(\gamma)\,, \end{aligned} \tag{1.93}$$

where

$$b = \frac{11 N_c - 4 T_R N_f}{12\pi} \equiv \frac{C_A}{\pi}\overline{b}\,, \tag{1.94}$$

is the first beta-function coefficient, $N_f$ the number of active quark flavors, $T_R = 1/2$ and

$$\Phi(\gamma) = \sum_{n=0}^{\infty} (-1)^n \left[\frac{\psi(n+1+\gamma) - \psi(1)}{(n+\gamma)^2} + \frac{\psi(n+2-\gamma) - \psi(1)}{(n+1+\gamma)^2}\right]. \tag{1.95}$$

There is no complete calculation on the NNLO kernel in QCD available, but the NNLO kernel in the $N = 4$ super Yang-Mills has been derived in [69–71].

#### 1.4.3.2 The pole structure of the LL BFKL eigenfunction

In this subsection, we will elaborate more on the structure of the BFKL eigenfunction in the Mellin space, especially its poles in the collinear limit. In principle, the BFKL only imposes the strong ordering on the longitudinal momentum fraction $x$ and does not require any strong ordering on the transverse momentum squared $k^2$, like the case in DGLAP. Nevertheless, it won't stop us from analyzing how much the collinear limit contributes to the LL BFKL kernel.

The general form of BFKL equation in $(x, k^2)$ space with kernel $\mathcal{K}(k, k')$ is

$$f(x, k^2) = f^{(0)}(x, k^2) + \overline{\alpha}_s \int_x^1 \frac{\mathrm{d}z}{z} \int \mathrm{d}k'^2 \mathcal{K}(k, k') f\left(\frac{x}{z}, k'^2\right). \tag{1.96}$$

In the collinear limit $k^2 \gg k'^2$, the major contribution to the BFKL kernel is

$$\mathcal{K}(k, k') \simeq \frac{1}{k^2}\Theta(k^2 - k'^2). \tag{1.97}$$

The corresponding Mellin space $\chi(\gamma)$ is given by

$$\chi(\gamma) = \int \mathrm{d}k'^2 \left(\frac{k'^2}{k^2}\right)^{\gamma-1} \mathcal{K}(k, k') \simeq \int \mathrm{d}k'^2 \left(\frac{k'^2}{k^2}\right)^{\gamma-1} \frac{1}{k^2}\Theta(k^2 - k'^2) = \frac{1}{\gamma}. \tag{1.98}$$

On the other hand, the kernel with both the collinear limit $k^2 \gg k'^2$ and the anti-collinear limit $k'^2 \gg k^2$ is

$$\mathcal{K}^{\mathrm{coll}}(k, k') \simeq \frac{1}{k^2}\Theta(k^2 - k'^2) + \frac{1}{k'^2}\Theta(k'^2 - k^2). \tag{1.99}$$

Therefore, the BFKL kernel in Mellin space with complete collinear and anti-collinear limits is

$$\chi^{\mathrm{coll}}(\gamma) = \frac{1}{\gamma} + \frac{1}{1-\gamma}. \tag{1.100}$$

For simplicity, we will refer to both the collinear and anti-collinear limit as the collinear limit in the later text, as the LL BFKL includes both the strong and reverse strong ordering on transverse momentum. In fact, the collinear limit reproduce the poles at $\gamma = 0, 1$ of the LL BFKL kernel $\chi_0(\gamma) = 2\psi(1) - \psi(\gamma) - \psi(1-\gamma)$, see fig. 1.26 for a numerical comparison for the real $\gamma \in (0, 1)$. We comment that the collinear limit makes the major contribution to the LL BFKL kernel.

We note that there are more poles at other integer values of $\gamma$ other than the collinear poles, see fig. 1.27. The LL BFKL kernel $\chi(\gamma)$ has more poles at integer values of the real $\gamma$.

### 1.4.4 Other diagrams

In section 1.4.2, we calculated the amplitude for the gluon ladder and derived the BFKL equation. However, there could be some remaining problems in the computation. At first sight, apparently, some potential diagrams are missing in the computation, e.g., the self-interaction or vertex corrections, and quarks emissions. Additionally, we mentioned the strong ordering on $x$ or the collinear limit many times, how valid are they compared

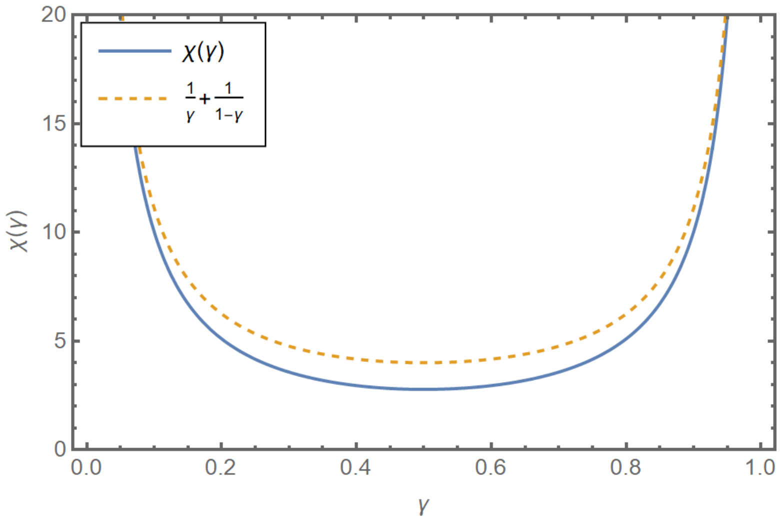


**Figure 1.26.** The complete LL BFKL $\chi(\gamma)$ compared with approximation due to the leading poles at $\gamma = 0, 1$.

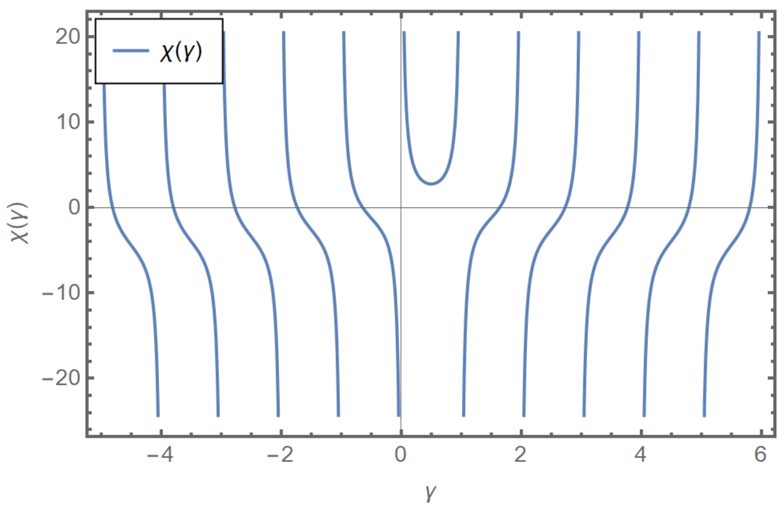


**Figure 1.27.** The LL BFKL $\chi(\gamma)$ in expanded range of real values of $\gamma$.

with a non-strong ordering gluon ladder? We will address these problems in the following subsections briefly.

#### 1.4.4.1 The ordering on the gluon ladder

We imposed the strong ordering on the gluon ladder and saw the amplitude under this limit. But one may ask, how would a non-strong ordering ladder contribute? Here, we argue that for the leading logarithm $\ln(1/x)$ or equivalently $\ln(s/\mathbf{k}^2)$ approximation, a strong ordering gives the dominant contribution and thus can replace any random ordering.

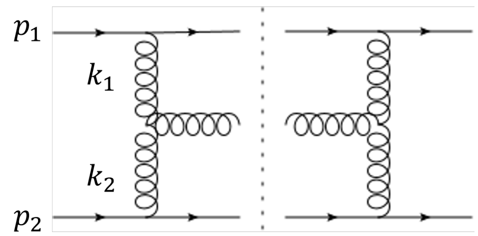


**Figure 1.28.** One rung ladder diagram.

As in the fig. 1.28, we take the one rung ladder as an example. A general form of the ordering stems from the kinematic constraint on the ladder,

$$\begin{aligned} 1 > \rho_1 > \rho_2 > 0, \\ 1 > |\lambda_2| > |\lambda_1| > 0. \end{aligned} \tag{1.101}$$

Note here the $\lambda_1, \lambda_2$ are negative. The three-body phase space integral is

$$\begin{aligned} \int \mathrm{d}\left(P.S.^3\right) =& \frac{s^2}{128\pi^5} \int \mathrm{d}\rho_1 \mathrm{d}\lambda_1 \mathrm{d}^2\mathbf{k}_1 \mathrm{d}\rho_2 \mathrm{d}\lambda_2 \mathrm{d}^2\mathbf{k}_2 \\ & \cdot \delta\left[-s\left(1-\rho_1\right)\lambda_1 - \mathbf{k}_1^2\right] \delta\left[s\left(1+\lambda_1\right)\rho_2 - \mathbf{k}_2^2\right] \\ & \cdot \delta\left[s\left(\rho_1-\rho_2\right)\left(\lambda_1-\lambda_2\right) - \left(\mathbf{k}_1^2 - \mathbf{k}_2\right)^2\right]. \end{aligned} \tag{1.102}$$

Since for the on-shell quarks $p_1^2 = p_2^2 = 0$, we expect the transverse momentum $\mathbf{k}_1, \mathbf{k}_2$ to be in the same order of magnitude. It is usually convenient to approximate

$$\mathbf{k}_1^2 \simeq \mathbf{k}_2^2 \simeq (\mathbf{k}_1 - \mathbf{k}_2)^2 \simeq \mathbf{k}^2. \tag{1.103}$$

Thus under the strong ordering

$$\begin{aligned} 1 \gg \rho_1 \gg \rho_2, \\ 1 \gg |\lambda_2| \gg |\lambda_1|, \end{aligned} \tag{1.104}$$

the phase space integral becomes

$$\begin{aligned} \int \mathrm{d}\left(P.S.^3\right) \simeq& \frac{s^2}{128\pi^5} \int \mathrm{d}\rho_1\ \mathrm{d}\lambda_1\ \mathrm{d}^2\mathbf{k}_1\ \mathrm{d}\rho_2\ \mathrm{d}\lambda_2\ \mathrm{d}^2\mathbf{k}_2 \\ & \cdot \delta\left(-s\lambda_1 - \mathbf{k}^2\right) \delta\left(s\rho_2 - \mathbf{k}^2\right) \delta\left(s\rho_1\lambda_2 - \mathbf{k}^2\right) \\ =& \frac{1}{128\pi^5} \int_{\rho_2}^{1} \frac{\mathrm{d}\rho_1}{\rho_1}\ \mathrm{d}\rho_2\ \mathrm{d}^2\mathbf{k}_1\ \mathrm{d}^2\mathbf{k}_2\ \delta\left(s\rho_2 - \mathbf{k}^2\right). \end{aligned} \tag{1.105}$$

Once we finish the integral over $\rho_2$, the only $\ln s$ term left is

$$\int_{\mathbf{k}^2/s}^{1} \frac{\mathrm{d}\rho_1}{\rho_1}. \tag{1.106}$$

With the strong ordering $1 \gg \rho_1 \gg \mathbf{k}^2/s$, we see that the strong ordering gives the dominant $\ln(s/\mathbf{k}^2)$ contribution in the high energy limit.

#### 1.4.4.2 Quark loops in the ladder

The QCD tells us the allowed strong interaction vertices include not only the gluons vertex, but also the quark-gluon vertex. We will demonstrate the contribution of the diagram with quarks lines, see fig. 1.29, comparing them with the gluon ladder diagram fig. 1.30 with two Lipatov effective vertices.

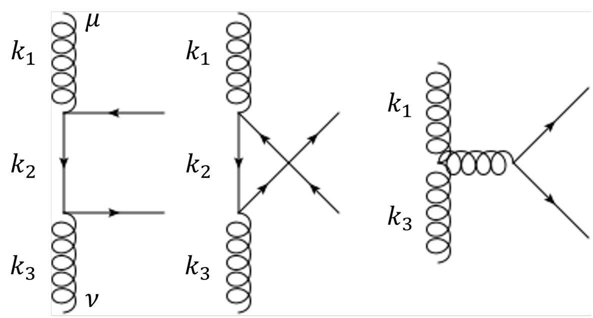


**Figure 1.29.** The ladder diagram with quark lines.

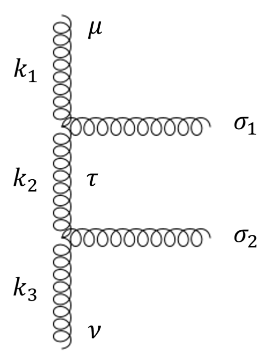


**Figure 1.30.** The ladder diagram with two Lipatov effective vertices.

In fig. 1.30, the two effective gluon vertices gives

$$\Gamma^{\sigma_1}_{\mu\tau}(k_1, k_2)\Gamma^{\tau\sigma_1}_{\nu}(k_2, k_3). \tag{1.107}$$

Its contribution proportional to $k_{1\perp}^{\sigma_1}k_{2\perp}^{\sigma_2}$ is

$$\sim \frac{2p_{2\mu}p_{1\nu}}{s}k_{1\perp}^{\sigma_1}k_{2\perp}^{\sigma_2}. \tag{1.108}$$

Meanwhile, the quark lines can appear in different diagrams as in fig. 1.29. Take the first diagram on the left of the figure for instance. Such a diagram contains terms proportional to

$$\frac{1}{\rho_1\lambda_3 s}\overline{u}(k_1-k_2)\gamma\cdot k_{1\perp}\gamma\cdot k_2\gamma\cdot k_{3\perp}u(k_3-k_2). \tag{1.109}$$

Again we note the scalar products $k_1\cdot k_2 \simeq k_2\cdot k_3 \simeq k_2^2 \simeq \mathbf{k}^2$. Therefore, this produces a term in the order of

$$\frac{\mathbf{k}^2}{\rho_1\lambda_3 s}\mathbf{k}^2. \tag{1.110}$$

Knowing the onshell condition gives

$$\rho_2\lambda_3 s \simeq -\mathbf{k}^2, \tag{1.111}$$

we see the first quark lines diagram comes with a suppression factor $\rho_2/\rho_1 \ll 1$, compared with the gluon ladder contribution eq. (1.108). The second and the third diagrams in fig. 1.29 face similar suppressions. In addition, the crossed and other possible gluon ladder diagrams with Lipatov effective vertices are also suppressed by a least one power of $\rho_2/\rho_1$, see details in [66].

#### 1.4.4.3 Gluon loop corrections to the vertex

The remaining types of diagrams we omitted on leading logarithm approximation BFKL derivation are the vertex correction diagrams, see fig. 1.31.

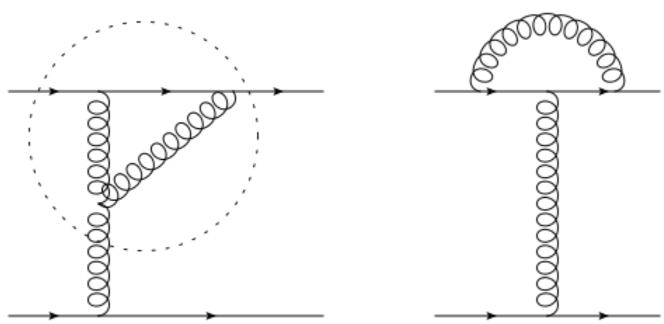

**Figure 1.31.** Gluon loop correction to the vertex diagrams.

For the first diagram in fig. 1.31 in the Feynman gauge, the on-shell condition of the top quark line that goes through the cut prevents the strong ordering of $\rho, \lambda$ on the gluon ladder. In other words, the incoming squared momentum going to the vertex is either 0 or $k^2$, but not $s$. Although a new gluon contributed a power of $\alpha_s$ to the diagram, it does not come with $\ln s$ in the leading logarithm approximation. Therefore, we can neglect this vertex correction. This is exactly the same case for the second diagram in fig. 1.31 and all self-energy insertion diagrams.

### 1.4.5 QCD factorization

In the previous subsection, we introduced the cross section within the framework of the high energy factorization. In this subsection, we aim to provide a clarification of both collinear and high energy factorization theory shortly and offer a brief context of the DGLAP and BFKL equations.

#### 1.4.5.1 Collinear factorization

Collinear factorization, named after the treatment of collinear singularities, arises from field theory calculations in perturbative QCD, where two distinct infra-red divergences (usually $1/k^2$ terms) —soft and collinear singularities—necessitate some careful consideration,

- Soft singularity: emission of gluon with vanishing four-momentum.
- Collinear singularity: emission of massless quarks (or gluons) which are collinear to the incoming parton.

These singularities correspond to the long-range (non-perturbative) interactions. Factorization is then developed to separate (or say factorize) the long- and short-distance effects of QCD.

For scatterings at the hard scale (the momentum transfer $Q^2 \gg \mu^2$ ), the collinear factorization asserts that all long-distance effects can be factorized into process-independent parton densities, so that the observables can be calculated perturbatively. We refer the readers to [59, 72–78] for detailed studies. The structure function in the collinear factorization is given by

$$F_i^{(H)}(x, Q^2) = \sum_a \int_x^1 \mathrm{d}z \, f^{(a/H)} \left(\frac{x}{z}, Q^2\right) \hat{F}_i^{(a)} \left(\frac{x}{z}, \alpha_s(Q^2)\right), \qquad (i = L, 2), \tag{1.112}$$

where $f^{(a/H)}$ is the process-independent parton density, which describes the probability of finding a type $a$ ($a = q, \overline{q}, g$) parton inside the hadron $H$ that carries a fraction $z$ of the parental hadron's longitudinal momentum. The $\hat{F}_i^{(a)}$ is the process-dependent partonic structure function that is available in the perturbative calculations. We note that parton distributions must be taken from experiments, like DIS, and its evolution above the factorization scale $\mu^2$ is governed by the DGLAP equation, as we discussed in section 1.3.3.

#### 1.4.5.2 High Energy (or $k_T$) factorization

In collinear factorization, we require the hard scale $Q^2 \gg \mu^2$. In the high energy limit $s \gg Q^2$, the BFKL formalism emerges as the dominant factorization scheme governing small $x$ physics. To summarize the series resummation in different factorizations:

- In the collinear factorization, the DGLAP resums:
  $(\alpha_s \ln Q^2)^n$, $n = 0, 1, \ldots$ series in the leading-logarithmic (LL) approximation,
  $\alpha_s(\alpha_s \ln Q^2)^n$ series in the next-to-leading-logarithmic (NLL) approximation, etc.
- In the high energy physics, the BFKL resums:
  $(\alpha_s \ln 1/x)^n$ series in L$x$ approximation,
  $\alpha_s(\alpha_s \ln 1/x)^n$ in NL$x$ approximation, etc.

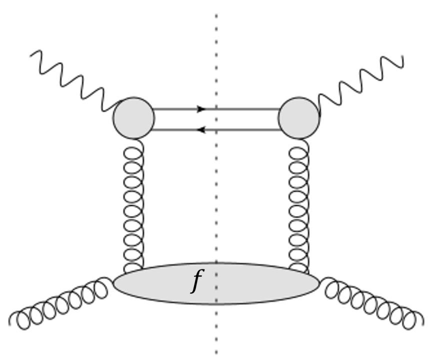


**Figure 1.32.** Factorized structure of the photoproduction cross section in the high energy limit.

The high energy factorization [79] states that the cross section (or consequently, the structure function $F_2(x, Q^2)$) in fig. 1.32 can be written in the following factorized form,

$$F_2(x, Q^2) = \int_x^1 \frac{\mathrm{d}z}{z} \int \mathrm{d}^2\mathbf{k}\ \hat{\sigma}\left(\frac{x}{z}, \frac{\mathbf{k}^2}{Q^2}\right) f(z, \mathbf{k}), \tag{1.113}$$

where the $\hat{\sigma}$ is the high energy partonic cross section for the subprocess $\gamma + g(k) \to q\bar{q}$ and two-momentum $\mathbf{k}$ is the transverse part of the off-shell gluon momentum $k$. The unintegrated gluon density $f$ of the incoming parental hadron, as we introduced shortly at the beginning of the section 1.4, is related to the parton density function $g(x, Q^2)$ by the $k_T$ integration

$$xg(x, Q^2) = \int^{Q^2} \mathrm{d}^2\mathbf{k}\ f(z, \mathbf{k}). \tag{1.114}$$

The evolution of the unintegrated gluon density $f$ is governed by the BFKL equation, while the experimental input shall serve as its initial condition and consequently, the non-perturbative contribution is factorized.

Comparing eq. (1.112) with eq. (1.113), we can get a quick observation that the high energy factorization further decomposes the $\mathbf{k}$ integration of the structure function. Such a factorization is, in a sense, more general than the collinear factorization. However, We note there is a different convention of the high energy factorization used in literature, for instance in [80].

Here the process-dependent function, impact factor $\phi(\omega, \gamma)$, is given by the $k_T$-transform of the partonic cross section $\hat{\sigma}$,

$$\phi(\omega, \gamma) = \gamma \int \frac{\mathrm{d}\mathbf{k}^2}{\mathbf{k}^2} \left(\frac{\mathbf{k}^2}{Q^2}\right)^{\gamma} \int_0^1 \frac{\mathrm{d}z}{z} \left(\frac{x}{z}\right)^{\omega} \hat{\sigma}\left(\frac{x}{z}, \frac{\mathbf{k}^2}{Q^2}\right), \tag{1.115}$$

The leading twist partonic cross section $\hat{\sigma}$ turns to be weakly $\omega$-dependent [81]. We present the well-known LO photon impact factors as follows,

$$\phi_0^{(T)}(\gamma) = \alpha\alpha_{\mathrm{s}}\Big(\sum_q e_q^2\Big) T_R \sqrt{2(N_c^2 - 1)}\, \frac{\pi}{2}\, \frac{(1+\gamma)(2-\gamma)\Gamma^2(\gamma)\Gamma^2(1-\gamma)}{(3-2\gamma)\Gamma(3/2+\gamma)\Gamma(3/2-\gamma)}\,, \tag{1.116a}$$

$$\phi_0^{(L)}(\gamma) = \alpha\alpha_{\mathrm{s}}\Big(\sum_q e_q^2\Big) T_R \sqrt{2(N_c^2 - 1)}\, \pi\, \frac{\Gamma(1+\gamma)\Gamma(2-\gamma)\Gamma(\gamma)\Gamma(1-\gamma)}{(3-2\gamma)\Gamma(3/2+\gamma)\Gamma(3/2-\gamma)}\,, \tag{1.116b}$$

where $\left(\sum_q e_q^2\right)$ sums over the quark flavors involved. We note that there are different conventions on the normalization of the impact factors in the literature [79, 82, 83].

# Chapter 2
# Improvements to the Gluon Evolution in BFKL Equation

In chapter 1, we showed the LL and NLL eigenfunctions of the BFKL equation. It is well known that the LL result is too large and indicates uncontrolled growth [84]. Meanwhile, the NLL eigenfunction can lead to instabilities in the computation [23–25], sometimes even with negative cross sections. A brief illustration of the $\omega$ intercept at LL and NLL is in fig. 2.1.

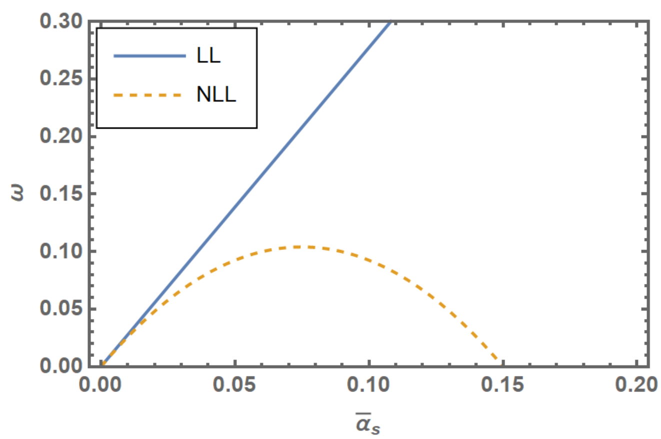


**Figure 2.1.** The LL and NLL $\omega$ intercept in function of $\overline{\alpha}_s$.

In order to better describe the experimental data, one must stabilize these results by higher order calculations or a resummation. There are various resummation approaches developed in the literature [26–40]. In this chapter, we will focus on two types of improvements. Firstly, we introduce the kinematical constraints and compute their effect on the BFKL solution in section 2.1. Secondly, we study the scale effect in the BFKL solution and investigate the renormalization group improvements (RGI) . After that, we proceed to study the analytical structure of the BFKL kernel to different orders in Mellin space with the $\omega$ expansion, in particular, in the context of $N = 4$ sYM. Note that these two types of improvements are well-related. The complete framework of renormalization group improved resummation in QCD, where the idea of $\omega$ expansion that originated from, will be formulated with more details in chapter 3.

## 2.1 Kinematical constraints

First, we recall the BFKL equation eq. (1.84) in $(x, k^2)$ space and the gluon splitting as illustrated in,

$$f(x,k^2) = f^{(0)}(x,k^2) + \overline{\alpha}_s \int_x^1 \frac{\mathrm{d}z}{z} \int \frac{\mathrm{d}^2\mathbf{q}}{\pi q^2} \left[ f\left(\frac{x}{z}, k'^2\right) - \Theta(k^2 - q^2) f\left(\frac{x}{z}, k^2\right) \right], \tag{2.1}$$

with a notation $k^2 = \mathbf{k}^2$.

The momenta are indicated in the diagram fig. 2.2, corresponding to the gluon splitting.

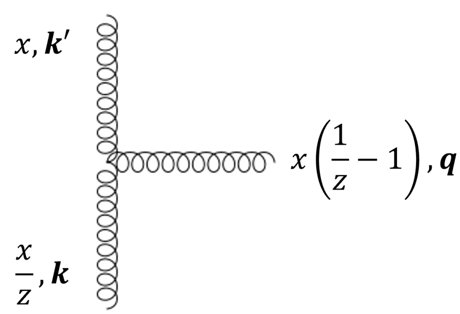


**Figure 2.2.** Gluon splitting in the BFKL diagram. The exchanged gluons carry the longitudinal momentum fractions $x$ and $x/z$ of the parental hadron. $\mathbf{k}$, $\mathbf{k}'$, and $\mathbf{q}$ are the transverse momenta of the exchanged gluons and emitted gluons respectively.

A starting observation is that the integral over the transverse momentum in the above equation is unbounded. However, in reality there needs to be restriction on the integration of the transverse momentum, stemming from the fact that in the high energy limit the virtuality of the exchanged momenta has to be dominated by the transverse components. Also the outgoing gluon should be put on-shell.

The idea of implementing the kinematic constraints to the BFKL evolution was proposed and studied in [41–44]. Meanwhile, the kinematic constraints are also relevant in the studies of Catani-Ciafaloni-Fiorani-Marchesini (CCFM) equation [41,85–88], where the color coherence in the form of angular ordering on the gluon ladder is asserted [89].

We note that there are different types of kinematic constraints used in literature and we will derive them by following the approach in [43]. We start with the light cone and transverse decomposition of a four-momentum $k^\mu$

$$k^\mu = (k^+, k^-, \mathbf{k}), \tag{2.2}$$

where the light cone components $k^\pm = k^0 \pm k^3$. The exchanged gluon virtuality is

$$k^\mu k_\mu = k^+ k^- - k^2. \tag{2.3}$$

In the context of small x physics, we are interested in a domain that the longitudinal components contribute to the gluon virtuality much less than the transverse components, this is translated to

$$k^2 > |k^+ k^-|. \tag{2.4}$$

The strong ordering on the longitudinal momentum fraction of the gluon ladder gives $k \gg k'$, thus,

$$k^- = k'^- - q^- \approx -q^-. \tag{2.5}$$

The last necessary condition is the on-shellness of the gluon emission that goes through the Cutkosky cut,

$$q^\mu q_\mu = q^+ q^- - q^2 = 0 \quad \Longrightarrow \quad q^- = \frac{q^2}{q^+}. \tag{2.6}$$

Using eqs. (2.4) to (2.6), we get

$$k^2 > |k^+ k^-| \approx \left|k^+ q^-\right| = \left|k^+ \frac{q^2}{q^+}\right| = \frac{z}{1-z} q^2, \tag{2.7}$$

or as a limit on $q^2$ integration,

$$q^2 < \frac{1-z}{z} k^2. \tag{2.8}$$

Note there are several approximations appeared in the literature.

- In the small $z$ limit, eq. (2.8) is approximated to

$$q^2 < \frac{1}{z} k^2. \tag{2.9}$$

- For a given $k^2$, the high value of $q^2$ also implies a high value of $k'^2$,

$$k'^2 < \frac{1}{z} k^2. \tag{2.10}$$

A nice feature of eq. (2.10) is that it shifts the BFKL kernel in Mellin space with only a simple change of the argument to one of the Polygamma functions. We will show it in the next subsection.

### 2.1.1 The BFKL kernels with kinematical constraints in Mellin space

In this subsection, we will investigate how the different kinematic constraints affect the BFKL evolution in Mellin space. The BFKL equation in momentum space with the constraint eq. (2.8) is,

$$\begin{aligned} f(x,k^2) &= f^{(0)}(x,k^2) \\ &+ \overline{\alpha}_s \int_x^1 \frac{\mathrm{d}z}{z} \int \frac{\mathrm{d}^2\mathbf{q}}{\pi q^2} \left[ f\left(\frac{x}{z}, k'^2\right) \Theta\left(k^2 - \frac{z}{1-z} q^2\right) - \Theta(k^2 - q^2) f\left(\frac{x}{z}, k^2\right)\right] \,, \end{aligned} \tag{2.11}$$

where the kinematical constraint is implemented onto the real emission term in the form of the Heaviside function. Performing the Mellin transformation as the same procedures in section 1.4.3, we have

$$\begin{aligned} \bar{f}(\omega,k^2) &= \bar{f}^{(0)}(\omega,k^2) \\ &+ \overline{\alpha}_s \int_x^1 \frac{\mathrm{d}z}{z} z^\omega \int \frac{\mathrm{d}^2\mathbf{q}}{\pi q^2} \left[ \bar{f}\left(\omega, k'^2\right) \Theta\left(k^2 - \frac{z}{1-z} q^2\right) - \Theta(k^2 - q^2) \bar{f}\left(\omega, k^2\right)\right] \,. \end{aligned} \tag{2.12}$$

Continuing the other Mellin transformation from $k^2$ to $\gamma$, we arrive at the same algebraic form of the BFKL equation

$$\tilde{f}(\omega,\gamma) = \tilde{f}^{(0)}(\omega,\gamma) + \frac{\overline{\alpha}_s}{\omega} \chi(\gamma,\omega) \tilde{f}(\omega,\gamma)\,, \tag{2.13}$$

where the kernel is now modified to

$$\chi(\gamma,\omega) \;=\; \int \frac{\mathrm{d}^2\mathbf{q}}{\pi q^2} \left[ \left(1 + \frac{q^2}{k^2}\right)^{-\omega} \left(\frac{k'^2}{k^2}\right)^{\gamma-1} - \Theta(k^2 - q^2) \right] . \tag{2.14}$$

Note, that the kernel acquires additional $\omega$ dependence. Performing the angular integration and taking the substitution $k^2 = q^2 u$ when $k^2 \geqslant q^2$ and $q^2 = k^2 u$ when $k^2 < q^2$, we obtain,

$$\chi(\omega,\gamma) = \int_0^1 \frac{\mathrm{d}u}{u} \left[(1+u)^{-\omega}\left(1+u^{\omega+1-\gamma}\right) {}_2F_1(1-\gamma,1-\gamma;1;u) - 1\right] . \tag{2.15}$$

Here ${}_2F_1$ is hypergeometric function. Meanwhile, the BFKL kernel with the constraint $k^2 > zq^2$ is given by, see also [43],

$$\chi(\omega,\gamma) = \int_0^1 \frac{\mathrm{d}u}{u} \left[\left(1+u^{\omega+1-\gamma}\right) {}_2F_1(1-\gamma,1-\gamma;1;u) - 1\right] . \tag{2.16}$$

Unfortunately, we don't find any widely used functions to conclude these integrations into any convenient form. For comparison, the constraint $k^2 > zk'^2$ gives the kernel

$$\chi(\omega,\gamma) = 2\psi(1) - \psi(\gamma) - \psi(1-\gamma+\omega). \tag{2.17}$$

We see the constraint $k^2 > zk'^2$ bring a nice feature that only shifts one Polygamma function and consequently the pole position by $\omega$.

For every option of the kinematical constraints, their leading pole positions are given by the solution to

$$\omega = \overline{\alpha}_s \chi(\omega,\gamma) . \tag{2.18}$$

With the complicated $\omega$ dependence inside the kernel, we cannot solve the transcendental equation analytically. Nevertheless, one can formulate the numerical solution to give a formal 'effective' kernel

$$\omega = \chi_{\text{eff}}(\gamma,\overline{\alpha}_s) . \tag{2.19}$$

These kernels are important as they indicate the residue when we inverse the Mellin transform to compute the solution of unintegrated gluon density in momentum space and similarly the high energy factorization cross section with $\omega$ integration. In order to obtain the $\chi_{\text{eff}}$ we have solved the eq. (2.18) numerically for all three versions of the kernel with constraints eqs. (2.8) to (2.10), as shown in fig. 2.3. Here we choose two different values of the strong coupling constant, $\overline{\alpha}_s = 0.1,\ 0.2$

An obvious observation is that all the effective kernels are strongly reduced in the large $\gamma$ region (corresponding to $k'^2 > k^2$) compared to the standard LL BFKL kernel. Furthermore, we can decipher more information from the behaviors of these functions in different regions.

- The region at $\gamma \to 1$. We find that the results from the constraints eqs. (2.8) and (2.10) are close to each other. This is realized by seeing that at $\gamma = 1$,

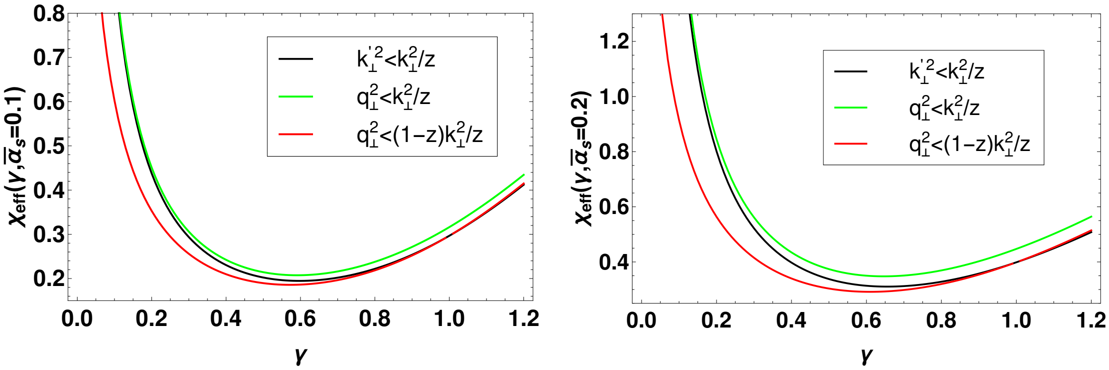


**Figure 2.3.** The effective BFKL kernel $\chi_{\rm eff}$ in Mellin space for the three different versions of the kinematical constraints eqs. (2.8) to (2.10). Left: $\overline{\alpha}_s = 0.1$, right: $\overline{\alpha}_s = 0.2$. The curves are red: $q^2 < (1-z)k^2/z$, green: $q^2 < k^2/x$, black: $k'^2 < k^2/z$.

eq. (2.14) is simplified to

$$\begin{aligned}\chi(\gamma,\omega)|_{\gamma=1} &= \int \frac{\mathrm{d}^2\mathbf{q}}{\pi q^2}\left[\left(1+\frac{q^2}{k^2}\right)^{-\omega}\left(\frac{k'^2}{k^2}\right)^{\gamma-1} - \Theta(k^2-q^2)\right]_{\gamma=1} \\ &= \int_0^1 \frac{\mathrm{d}u}{u}\left[(1+u)^{-\omega}(1+u^{\omega})-1\right] \\ &= \psi(1)-\psi(\omega) \\ &= \left[2\psi(1)-\psi(\gamma)-\psi(1-\gamma+\omega)\right]_{\gamma=1}. \end{aligned} \tag{2.20}$$

We see the kernels from eqs. (2.8) and (2.10) are identical for any value of $\omega$ now. In a more kinematical perspective, for $z \to 1$, both eqs. (2.8) and (2.10) leads to a strong suppression of the anti-collinear phase space ($k^2 < k'^2$), while the eq. (2.9) still give some phase space for the integration.

- The region at at $\gamma \to 0$. We see that the curves from the constraints eqs. (2.9) and (2.10) are close, where eq. (2.8) is smaller in this range. This is understood from the fact that the constraint eq. (2.8) is stronger at the collinear region $k^2 > k'^2$, particularly if $z$ is large. The notable difference here is that compared with the other two constraints, eq. (2.8) lacks the collinear pole in $\gamma$.

Now we can revisit the fig. 2.1 with the kinematically constrained kernel. Note the saddle points are no longer at $\gamma = \frac{1}{2}$ for these shifted kernels. From $\chi_{\rm eff}$, one can compute the leading behavior as $x \to 0$. The intercepts $\omega_0$ are now given by

$$\frac{\mathrm{d}\chi_{\rm eff}(\gamma,\overline{\alpha}_s)}{\mathrm{d}\gamma}|_{\gamma=\gamma_M} = 0\,, \quad \omega_0 = \chi_{\rm eff}(\gamma_M,\overline{\alpha}_s)\,, \tag{2.21}$$

and the results are plotted in Fig. 2.4. We see all three constraints stabilize the intercepts, compared with LL and NLL results in QCD. What's more, for $\overline{\alpha}_s$ up to about 0.2, the discrepancies between the curves are minimal. When $\overline{\alpha}_s$ is larger, the constraint eq. (2.9) is comparably larger than the other two constraints. This is consistent with the shape of the kernel discussed before.

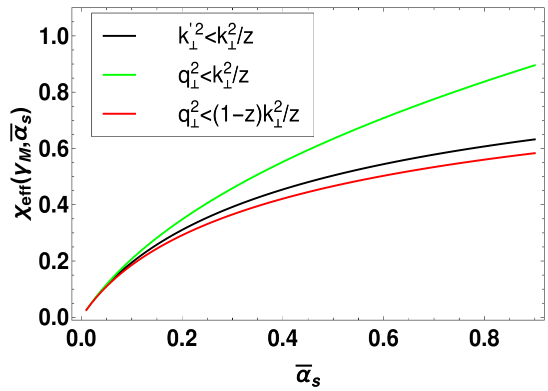


**Figure 2.4.** The values of the intercept $\omega_0 = \chi_{\rm eff}(\gamma_M, \overline{\alpha}_s)$, Eq. (2.21), as a function of $\bar{\alpha}_s$ for different choices of the kinematical constraint.

### 2.1.2 Differential form of the BFKL equation with kinematical constraints

In the previous subsection, we investigated the behaviors of the kernels with kinematical constraints. In this subsection, we will present numerical solutions for the unintegrated gluon density.

There are different techniques utilized to solve the BFKL equation in the past. One approach we have introduced is the inverse Mellin transform. The advantage of this approach is that it empowers more insights into the analytical structure, in particular, the collinear and anti-collinear poles at LL, NLL, or resummed calculation.

The other notable method [34,44,90] is to incorporate an interpolation to the evolution equation in two variables $x$ and $k^2$ with orthogonal polynomials, such that the integral equations can be transformed into a set of linear algebraic equations and solved by simply inverting the large matrix. We will look into more details of the approach in the next section.

In this subsection, we will introduce and utilize another method that transforms the integral equation into a differential equation.

The motivation to differentiate the BFKL equation by $x$ is that it could help reduce the computational complexity of the integral on the right-hand side of the equation. After performing the derivative we find, regardless of the form of the kinematical constraint, the resulting equation can be written in the differential form that shares two terms in common - real emission term with shifted argument $x$ and virtual correction term - under the remaining integral over the emitted momentum $\mathbf{q}$. We take a symbolic representation of different kinematical constraints $\theta\left[k_C\left(\mathbf{q},\mathbf{k}\right)-z\right]$. As a result, the argument of the real emission term is shifted as

$$x \to x\ \max\left\{1, \frac{1}{k_C\left(\mathbf{q},\mathbf{k}\right)}\right\}\ . \tag{2.22}$$

Such reformulation of the BFKL equation with kinematical constraint was first proposed in [42], and similar ideas were also discussed in [91] in the context of the Balitsky-Kovchegov (BK) evolution equation in transverse coordinate space. We derive the differential form of the BFKL equation for each kinematical constraint as follows,

- The kinematical constraint $q^2 < k^2/z$.

  The differential equation in this case is given by

$$\begin{aligned}\frac{\partial f(x,k^2)}{\partial x} = \frac{\partial f^{(0)}(x,k^2)}{\partial x} + \bar{\alpha}_s \frac{\partial}{\partial x}\int_x^1 \frac{\mathrm{d}x'}{x'}\ \int \frac{\mathrm{d}^2\mathbf{q}}{\pi q^2}\Big\{ f\left(x',k'^2\right)\Theta\left(k^2-\frac{x}{x'}q^2\right) \\ -\ \Theta\left(k^2-q^2\right) f\left(x',k^2\right)\Big\}\ .\end{aligned} \tag{2.23}$$

  where we performed the change of variable $z \to x' = x/z$. After performing the direct calculation of the derivatives, we see

$$\begin{aligned}\frac{\partial f(x,k^2)}{\partial x} =& \frac{\partial f^{(0)}(x,k^2)}{\partial x} - \frac{\bar{\alpha}_s}{x}\ \int \frac{\mathrm{d}^2\mathbf{q}}{\pi q^2}\Big\{ f\left(x\ \max\left(1,\frac{q^2}{k^2}\right),k'^2\right)\Theta\left(\frac{k^2}{q^2}-x\right) \\ &- \Theta\left(k^2-q^2\right) f\left(x,k^2\right)\Big\}\ ,\end{aligned} \tag{2.24}$$

  where the expression $x\ \max\left(1,q^2/k^2\right)$ comes from two terms, as we see how derivative acts on the integral on the right-hand side of the (2.23). The first term that comes from derivative on the boundary of the integral generates the term containing $f\left(x,k'^2\right)\Theta\left(k^2-q^2\right)$, while the second term acts on the $\Theta$-function from kinematical constraint and produces a term containing $f\left[xq^2/k^2,|k-q|^2\right]\Theta\left(q^2-k^2\right)$.

Now, rewriting the derivative equation as a derivative by $\ln 1/x$ instead of $x$, we get

$$\begin{aligned}\frac{\partial f(x,k^2)}{\partial \ln 1/x} =& \frac{\partial f^{(0)}(x,k^2)}{\partial \ln 1/x} + \bar{\alpha}_s \int \frac{\mathrm{d}^2\mathbf{q}}{\pi q^2}\left\{ f\left(x \max\left(1, \frac{q^2}{k^2}\right), k'^2\right) \Theta\left(\frac{k^2}{q^2} - x\right)\right. \\ & \left. - \Theta\left(k^2 - q^2\right) f\left(x, k^2\right)\right\}.\end{aligned} \tag{2.25}$$

- The kinematical constraint $k'^2 < k^2/z$.

  The differential equation now is derived in exactly the same way as in the last case,

$$\begin{aligned}\frac{\partial f(x,k^2)}{\partial \ln 1/x} =& \frac{\partial f^{(0)}(x,k^2)}{\partial \ln 1/x} + \bar{\alpha}_s \int \frac{\mathrm{d}^2\mathbf{q}}{\pi q^2}\left\{ f\left(x \max\left(1, \frac{k'^2}{k^2}\right), k'^2\right) \Theta\left(\frac{k^2}{k'^2} - x\right)\right. \\ & \left. - \Theta\left(k^2 - q^2\right) f\left(x, k^2\right)\right\}.\end{aligned} \tag{2.26}$$

  We see that the only difference between the two cases is solely on the factor in the longitudinal component of the unintegrated gluon density $f$.

- The kinematical constraint $q^2 < (1-z)k^2/z$.

  This case is slightly different since now the term originating from the derivative acting on the integral boundary is equal to 0. This is due to the fact that the $\Theta$-function is evaluated at $-\infty$. This is manifested that the constraint $x' > xk'^2/k^2$ is a stronger condition than $x' > x$. Thus the boundary term no longer contributes and the differential equation is eventually given by

$$\begin{aligned}\frac{\partial f(x,k^2)}{\partial \ln 1/x} =& \frac{\partial f^{(0)}(x,k^2)}{\partial \ln 1/x} + \bar{\alpha}_s \int \frac{\mathrm{d}^2\mathbf{q}}{\pi q^2}\left\{ f\left(x \frac{k^2+q^2}{k^2}, k'^2\right) \Theta\left(\frac{k^2}{q^2+k^2} - x\right)\right. \\ & \left. - \Theta\left(k^2 - q^2\right) f\left(x, k^2\right)\right\}.\end{aligned} \tag{2.27}$$

### 2.1.3 Numerical results

In this subsection, we present the numerical results for the solution of the BFKL equation with different kinematical constraints. We propose the boundary condition for the equations,

$$f(x,k) = \exp\left[p_0 \log\left(k/\mu\right)^2 + p_1 \log^2\left(k/\mu\right)^2\right](1-x)^{p_2} \ , \tag{2.28}$$

with $p_0 = p_1 = -0.1$ and $p_2 = 2$ and $\mu = 1\,\text{GeV}$. Note here that we are not fitting the boundary conditions to any experimental data. The following are for demonstration only and not for phenomenology usage.

Our choice of $k$ dependence is motivated by the analytical solution of the LL BFKL equation and is proposed for faster convergence of the numerical solution. The term $(1-x)^{p_2}$ is widely used in the relevant phenomenology studies, as such, the gluon is suppressed for large values of $x$, and as a result, we can safely extend the integral over the kernel to large $x$ values. Additionally, we introduce a lower cutoff onto the transverse momenta $Q_0 = 0.1$ GeV. All results are obtained for the fixed coupling $\overline{\alpha}_s = 0.2$.

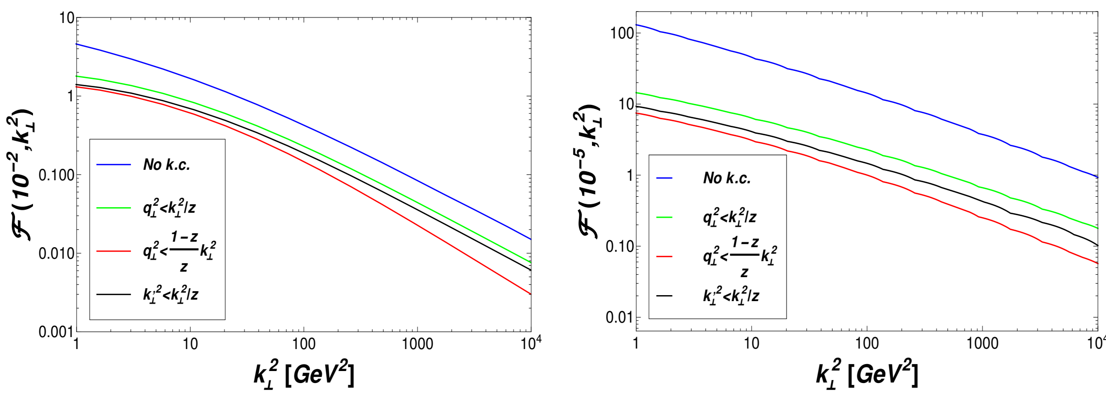


**Figure 2.5.** Solutions of the BFKL equations with different forms of the kinematical constraint as functions of $k_T$ for constant $\bar{\alpha}_S = 0.2$. Left plot: $x = 10^{-2}$, right plot: $x = 10^{-5}$.

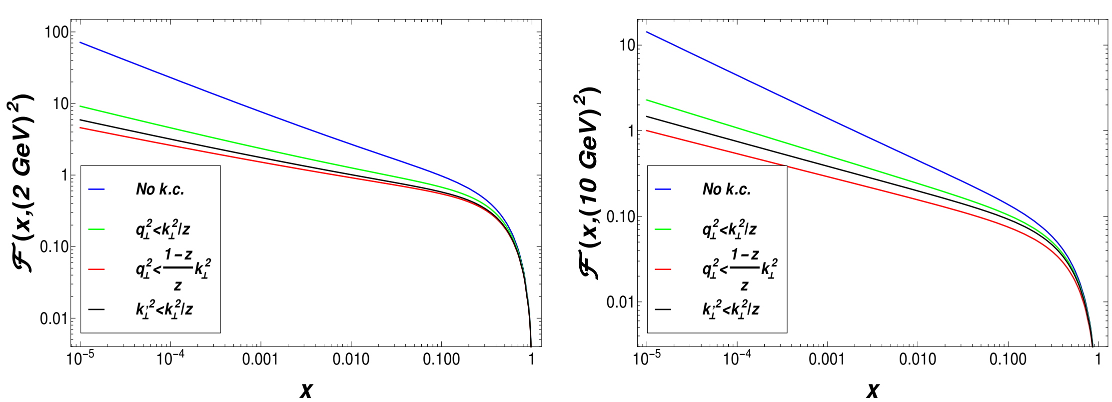


**Figure 2.6.** Solutions to the BFKL equation with three different forms of the constraint as a function of $x$ for constant $\bar{\alpha}_S = 0.2$. Left plot: $k = 2\,\text{GeV}$, right plot $k = 10\,\text{GeV}$.

In figs. 2.5 and 2.6 in logarithm scales on both axes, we present the solutions as a function of the $k^2$ $(x)$ for fixed values of $x$ $(k^2)$ with different kinematical constraints respectively, compared with the standard LL BFKL solution.

A major remark is that all kinematical constraints significantly reduce the solution with respect the the LL BFKL unintegrated gluon solution, while the differences between these kinematical constraints are non-negligible and could reach up to a factor of $2 \sim 3$ depending on the values of $x$ and $k^2$. Their magnitudes decrease in a fixed order for the constraints: $q^2 < k^2/z \;\rightarrow\; k'^2 < k^2/z \;\rightarrow\; q^2 < \frac{1-z}{z}k^2$.

## 2.2 $\omega$ Expansion of the Kernel in QCD and N = 4 sYM

In this section, we review the effect of different choices of energy scale in the high energy factorization cross section and propose the $\omega$ dependent BFKL kernel to abide by the scale invariance requirements. Next, we introduce the technique of $\omega$ expansion in the context of renormalization group constraints to construct the NLL and NNLL kernel and prove an interesting feature of the structure of the collinear poles in $N = 4$ supersymmetric Yang–Mills (sYM) theory.

In $N$ sYM, $N$ represents the number of independent supersymmetric operations that transform the boson field into fermion field, where $N = 4$ is the maximal candidate. Practically, $N = 4$ sYM is a toy model that does not fit into any exact physics. However, N = 4 sYM shares the same gluon sectors with QCD, which includes the complicated Feynman gluon diagrams, so that solutions to $N = 4$ sYM can also shed light into similar problems in QCD. Meanwhile, the properties of the $N = 4$ sYM, e.g., the vanishing beta function, more degrees of symmetries, make the solution more available than QCD. Above all, $N = 4$ sYM is a helpful playground for the study of QCD and other theories.

### 2.2.1 Scale Effect and the $\omega$ Dependent BFKL Kernel in QCD

We start with the general formula in the high energy factorization for the process with two hard scales $Q_1, Q_2$,

$$\sigma = \int \frac{\mathrm{d}\omega}{2\pi i} \int \frac{\mathrm{d}^2\mathbf{k}}{k^2} \frac{\mathrm{d}^2\mathbf{k}'}{k'^2} \left(\frac{s}{s_0}\right)^{\omega} \phi^A(Q_1, \mathbf{k}) \mathcal{G}(\omega, \mathbf{k}, \mathbf{k}') \phi^B(Q_2, \mathbf{k}'). \tag{2.29}$$

As we are interested in the BFKL kernel, we can use the double Mellin transform to write the azimuthally averaged gluon Green's function as

$$\mathcal{G}(s, k, k') = \frac{1}{2\pi k^2} \int \frac{\mathrm{d}\omega}{2\pi i} \left(\frac{s}{s_0}\right)^{\omega} \int \frac{\mathrm{d}\gamma}{2\pi i} \left(\frac{k^2}{k'^2}\right)^{\gamma} \mathcal{G}(\omega, \gamma)\,, \tag{2.30}$$

Here, we can use a symmetric choice of the energy scale $s_0 = kk'$. However, the scale choice can be also asymmetric. For example, the scales on the virtual photon and the proton side are, in principle, very different in the Deep Inelastic Scattering. In this case, the cross section is dominated by either collinear (anticollinear) configurations with $k^2 \gg k'^2$ ($k'^2 \gg k^2$) so that the appropriate Bjorken evolution variable is $k^2/s$ ($k'^2/s$), corresponding to the asymmetric energy scale $s_0 = k^2$ ($s_0 = k'^2$).

An important comment is that such a change of energy scale in eq. (2.30) is equivalent to a shift of $\gamma$ by $\pm\omega/2$, relative to the symmetric energy choice $s_0 = kk'$,

$$\begin{aligned} \left(\frac{s}{kk'}\right)^{\omega}\left(\frac{k^2}{k'^2}\right)^{\gamma} &= \left(\frac{s}{k^2}\right)^{\omega}\left(\frac{k}{k'}\right)^{\omega}\left(\frac{k^2}{k'^2}\right)^{\gamma} = \left(\frac{s}{k^2}\right)^{\omega}\left(\frac{k^2}{k'^2}\right)^{\gamma+\omega/2}, \quad s_0 = k^2, \\ \left(\frac{s}{kk'}\right)^{\omega}\left(\frac{k^2}{k'^2}\right)^{\gamma} &= \left(\frac{s}{k'^2}\right)^{\omega}\left(\frac{k'}{k}\right)^{\omega}\left(\frac{k^2}{k'^2}\right)^{\gamma} = \left(\frac{s}{k'^2}\right)^{\omega}\left(\frac{k^2}{k'^2}\right)^{\gamma-\omega/2}, \quad s_0 = k'^2. \end{aligned} \tag{2.31}$$

These corrections project into the simple LL BFKL kernel $\mathcal{K}(k, k')$ with only collinear and anti collinear poles as

$$\mathcal{K}^{\omega}(k, k') \simeq \overline{\alpha}_s \left[\frac{1}{k^2}\left(\frac{k'}{k}\right)^{\omega}\Theta(k - k') + \frac{1}{k'^2}\left(\frac{k}{k'}\right)^{\omega}\Theta(k' - k)\right]. \tag{2.32}$$

In the Mellin space, it corresponds to $\omega$ shift poles at $\gamma = 0$ or $\gamma = 1$,

$$\chi_0(\omega, \gamma) \simeq \frac{1}{\gamma + \frac{\omega}{2}} + \frac{1}{1 - \gamma + \frac{\omega}{2}}. \tag{2.33}$$

This indicates the scale-invariant LL BFKL kernel in symmetric energy choice $s_0 = kk'$ would gain the $\omega$ dependency,

$$\chi_0^S(\omega, \gamma) = 2\psi(1) - \psi(\gamma + \frac{\omega}{2}) - \psi(1 - \gamma + \frac{\omega}{2}). \tag{2.34}$$

Furthermore, in symmetric energy choice $s_0 = kk'^2$, the $\omega$ shifted LL BFKL kernel reads,

$$\chi_0^A(\omega, \gamma) = 2\psi(1) - \psi(\gamma) - \psi(1 - \gamma + \omega). \tag{2.35}$$

This is exactly the same result we get under the kinematical constraint $k'^2 < k^2/z$.

### 2.2.2 Renormalization group constraints

Now we proceed to see how we extend the $\omega$ dependency into NLL BFKL kernels and in principle, the kernel in an arbitrary order. We follow the approach in [34].

The non-singular part of the singlet gluon anomalous dimension

$$\tilde{\gamma}_\omega = \gamma_{gg} - \frac{\overline{\alpha}_s}{\omega} = \overline{\alpha}_s A_1(\omega), \tag{2.36}$$

where $A_1(\omega) = -11/12 + \mathcal{O}(\omega)$ for $N_f = 0$. The singular part of the $\gamma_{gg}$ has been taken into account by the BFKL iteration itself. This is manifested in the discussion section 1.4 that the singular $1/x$ term from the splitting function $P_{gg}$ contributes to the logarithm $\ln(1/x)$ in the LL BFKL.

The BFKL kernel $\mathcal{K}_\omega(k,k')$ in the collinear limit $k^2 \gg k'^2$ acquires a form [92],

$$\begin{aligned}\mathcal{K}_\omega(k,k') &\approx \frac{\overline{\alpha}_s(k^2)}{k^2} \exp \int_{t_0}^{t} \tilde{\gamma}_\omega(\overline{\alpha}_s(l^2)) \mathrm{d}(\ln l^2) \\ &= \frac{\overline{\alpha}_s(k^2)}{k^2} \left[1 - b\overline{\alpha}_s(k^2) \ln\left(\frac{k^2}{k'^2}\right)\right]^{-A_1(\omega)/b},\end{aligned} \tag{2.37}$$

where $t = \ln(k^2/\mu^2)$ and $t_0 = \ln(k'^2/\mu^2)$. Now with the knowledge of the $\omega$ dependent scale terms, we can construct the BFKL kernel with both collinear and anti-collinear terms

$$\begin{aligned}\mathcal{K}^\omega(k,k') \approx \overline{\alpha}_s(k^2) \Bigg\{ &\frac{1}{k^2}\left(\frac{k'}{k}\right)^\omega \left[\frac{\overline{\alpha}_s(k^2)}{\overline{\alpha}_s(k'^2)}\right]^{-\frac{A_1(\omega)}{b}} \Theta(k-k') \\ &+ \frac{1}{k'^2}\left(\frac{k}{k'}\right)^\omega \left[\frac{\overline{\alpha}_s(k^2)}{\overline{\alpha}_s(k'^2)}\right]^{\frac{A_1(\omega)}{b}-1} \Theta(k'-k)\Bigg\}.\end{aligned} \tag{2.38}$$

Expanding in $\overline{\alpha}_s$, we have the $\omega$ dependent kernel in the form

$$\chi^\omega(\gamma) = \sum_{n=0}^{\infty} \left[\overline{\alpha}_s(k^2)\right]^{n+1} \chi_n^\omega(\gamma). \tag{2.39}$$

Under the symmetric energy scale choice, eq. (2.38) allows us to obtain the

$$\chi_n^\omega(\gamma) = \frac{1 \cdot A_1(A_1+b)\cdots[A_1+(n-1)b]}{\left(\gamma+\frac{\omega}{2}\right)^{n+1}} + \frac{1\cdot(A_1-b)(A_1-2b)\cdots[A_1-nb]}{\left(1-\gamma+\frac{\omega}{2}\right)^{n+1}}. \tag{2.40}$$

In particular, the LL and NLL results are

$$\begin{aligned}\chi_0^\omega &\approx \frac{1}{\gamma+\frac{\omega}{2}} + \frac{1}{1-\gamma+\frac{\omega}{2}},\\ \chi_1^\omega &\approx \frac{A_1(\omega)}{\left(\gamma+\frac{\omega}{2}\right)^2} + \frac{A_1(\omega-b)}{\left(1-\gamma+\frac{\omega}{2}\right)^2}.\end{aligned} \tag{2.41}$$

We note that the second line in eq. (2.41) contributes to the full double poles in the standard NLL BFKL kernel eq. (1.93). This is the effect of the above discussion involving the running coupling effect and non-singular LO DGLAP splitting functions. Furthermore, it indicates the way to construct the $\omega$ dependent NLL BFKL kernel by shifting the double poles.

Next, notice that in the small $\omega$ limit, $\omega \to \overline{\alpha}_s \chi_0^{\omega=0}$. We see that each $\omega$ includes the coefficient of running coupling $\overline{\alpha}_s$. This implies that by expanding the LL BFKL kernel on $\omega$, we can get a new BFKL kernel that features the collinear and anti-collinear poles up to NLL.

$$\begin{aligned}\chi_1^{\text{coll}} &= \left[\overline{\alpha}_s \chi_0^\omega(\gamma)\frac{\partial \chi_0^\omega}{\partial\omega} + \chi_1^\omega\right]_{\omega=0}\\ &= -\frac{1}{2\gamma^3} - \frac{1}{2(1-\gamma)^3} + \frac{A_1(0)}{\gamma^2} + \frac{A_1(0)-b}{(1-\gamma)^2} + \cdots .\end{aligned} \tag{2.42}$$

It turns out this NLL kernel in the collinear approximation reproduces the exact NLL kernel up to 7% [33, 64]. This indicates that the collinear terms are the dominant contribution in the NLL. Now we can propose an $\omega$ shifted NLL kernel [34],

$$\begin{aligned}\chi_1(\omega,\gamma) = {} & \chi_1(\gamma) + \frac{1}{2}\chi_0(\gamma)\frac{\pi^2}{\sin^2\pi\gamma}\\ & - A_1(0)\psi'(\gamma) - \left[A_1(0)-b\right]\psi'(1-\gamma)\\ & + A_1(\omega)\psi'\left(\gamma+\frac{\omega}{2}\right) + \left[A_1(\omega)-b\right]\psi'\left(1-\gamma+\frac{\omega}{2}\right)\\ & - \frac{\pi^2}{6}\left[\chi_0(\gamma)-\chi_0^\omega(\gamma)\right].\end{aligned} \tag{2.43}$$

We shall emphasize the role of every term in the subtraction introduced in eq. (2.43) as follows.

- The first line: standard NLL BFKL $\chi_1(\gamma)$ in QCD with the subtraction terms of the cubic poles. The subtraction term is the outcome of the consideration of the energy scale effect and is straightforwardly generated by

$$\chi_0^\omega(\gamma)\frac{\partial\chi_0^\omega}{\partial\omega}\bigg|_{\omega=0} = \frac{1}{2}\chi_0(\gamma)\frac{\pi^2}{\sin^2\pi\gamma}. \tag{2.44}$$

- The second and third lines: the $\omega$ shifted double poles introduced from the above collinear analysis. Note we only require the shift on the poles. Therefore, the realization is not necessarily done only by subtracting $\psi'$ functions. There is flexibility in the choice of the candidate functions.

- The last line: this shifts the single poles and appears as an artifact of the resummation procedure.

### 2.2.3 NLL and NNLL of N = 4 sYM via $\omega$ expansion

It is certainly of interest to further investigate the NNLL BFKL kernel in QCD. However, as we mentioned in section 1.4.3, there is no complete NNLL result available in QCD. Nevertheless, it does not prevent us from probing the NNLL structure using the $\omega$ expansion technique.

In particular, the $N = 4$ sYM eigenvalue at LL is the same as the QCD case, and at NLL, both theories share identical leading cubic poles [93]. In addition, under the symmetric choice of the energy scale, the $N = 4$ sYM NNLL kernel was derived originally in [69, 70]. It was later re-derived in [71] by investigating the correspondence between the soft-gluon wide-angle radiation in jet physics and the BFKL physics. We are motivated to test $\omega$ shifted kernels in the playground of $N = 4$ sYM and see if they can match the known NLL and NNLL results.

To remain relevant to these existing results, we will keep a symmetric energy scale. In this subsection, we shall perform a detailed comparison of leading and subleading poles in the Mellin space up to NNLL $N = 4$ sYM.

The NLL poles [93] and NNLL poles [69–71] in $N = 4$ sYM at $\gamma = 0$ are

$$\chi_1^{sYM} = -\frac{1}{2\gamma^3} - 1.79 + \mathcal{O}(\gamma)\ , \tag{2.45}$$

$$\chi_2^{sYM} = \frac{1}{2\gamma^5} - \frac{\zeta(2)}{\gamma^3} - \frac{9\zeta(3)}{4\gamma^2} - \frac{29\zeta(4)}{8\gamma} + \mathcal{O}(1)\ . \tag{2.46}$$

Note that, in the symmetric energy scale, the coefficients of the poles around $\gamma = 0$ and $\gamma = 1$ are identical. To keep a simple representation, we only show the expansion at

$\gamma = 0$ in the following. We can retrieve the leading and the vanishing subleading poles of the $N = 4$ sYM case by doing $\omega$ expansion of the shifted eigenvalue eq. (2.34) in the same way as the QCD case,

$$\begin{aligned}\chi(\gamma, \omega) &= 2\psi(1) - \psi(\gamma + \frac{\omega}{2}) - \psi(1 - \gamma + \frac{\omega}{2}) \\ &= \chi_0 + \chi^{(1)}\frac{\omega}{2} + \frac{1}{2!}\chi^{(2)}\left(\frac{\omega}{2}\right)^2 + \dots\,,\end{aligned} \tag{2.47}$$

where the $\chi^{(i)}$ is the i-th derivative of $\chi^{\omega}$ with respect to $\omega$. Provided that the LL relation $\omega_0 = \overline{\alpha}_s\chi_0$, the NLL term is identified to be

$$\chi_1(\gamma) = \frac{1}{2}\chi^{(1)}\chi_0 = \frac{1}{2}\left[\psi^{(1)}(\gamma) + \psi^{(1)}(1-\gamma)\right]\left[2\psi(1) - \psi(\gamma) - \psi(1-\gamma)\right]\,. \tag{2.48}$$

Expanding around $\gamma = 0$, one obtains the following NLL pole structure

$$\chi_1(\gamma) = -\frac{1}{2\gamma^3} - \frac{\zeta(2)}{\gamma} + O(1)\,. \tag{2.49}$$

Similarly, we can calculate the term contributing at NNLL from the $\omega$ expansion to the second order by taking $\omega_1 = \overline{\alpha}_s\chi_0 + \overline{\alpha}_s^2\chi_1$, where the subscript on $\omega$ indicates the order of expansion that we are interested in. Now we substitute $\omega_1$ into (2.47) and extract the $\overline{\alpha}_s^2$ terms

$$\chi_2 = \frac{1}{4}\left[\chi^{(1)}\right]^2\chi_0 + \frac{1}{8}\chi^{(2)}\left(\chi_0\right)^2\,. \tag{2.50}$$

Expanding at $\gamma = 0$ , we see the NLL pole structure

$$\chi_2 = \frac{1}{2\gamma^5} + \frac{\zeta(2)}{\gamma^3} + \frac{2\zeta(3)}{\gamma^2} + O\left(\frac{1}{\gamma}\right)\,. \tag{2.51}$$

We observe that the leading pole $-1/2\gamma^3$ in eq. (2.49) coincides with the exact result at NLL in $N = 4$ SYM and in QCD. The NNLL leading pole $1/2\gamma^5$ in eq. (2.51) reproduces the NNLL $N = 4$ SYM in eq. (2.46). This structure is consistent with the principle of maximal transcendentality (complexity) [93], meaning that all special functions at the NNLL correction contain only sums of the terms $1/\gamma^i$ (i= 3, 5).

In addition, another interesting feature is the absence of subleading poles, i.e. $1/\gamma^2$ and $1/\gamma^4$ vanish at NLL and NNLL respectively in both our expanded result and exact $N = 4$ sYM (2.46). It is worth mentioning that we have checked numerically the coefficients of the poles in $1 - \gamma$ for the BFKL kernels with kinematic constraints in the asymmetric scale. We found agreement between different forms of constraints in the leading poles $\sim 1/(1-\gamma)^{2k+1}$ and subleading poles $\sim 1/(1-\gamma)^{2k}$ when the kernels are expanded out to NLL ($k=1$) and NNLL ($k=2$).

We shall see later soon in the next subsection that the pattern in the symmetric scale of the leading and sub-leading poles holds to all orders in $\overline{\alpha}_s$ from the $\omega$ expansion. In contrast, there are double poles $1/\gamma^2$ in NLL QCD, originating from the non-singular parts of the QCD DGLAP anomalous dimension and the running coupling [21, 22].

### 2.2.4 Leading and subleading poles to all orders in $\omega$ expansion

We see an interesting pattern on the leading and sub-leading poles in the NLL and NNLL $\omega$ expansion kernel in the context of $N=4$ sYM. In fact, this pattern is valid for any arbitrary order of expansion, i.e., the $\chi_k$ has the leading pole $\sim \frac{1}{\gamma^{2k+1}}$, while the subleading pole $\sim \frac{1}{\gamma^{2k}}$ vanishes. At NLL and NNLL order, both $N=4$ sYM results and QCD the kernel with kinematical constraint $k'^2 < k^2/z$ agrees with the pattern. This pattern can be proved by mathematical induction.

Let us assume that the kernel $\chi_k$ features the above-discussed properties, and we will prove that the kernel $\chi_{k+1}$ in one order higher also possesses the same properties. We begin with writing the solution for the BFKL equation in Mellin space up to $k+1$'th power in $\overline{\alpha}_s$ (again, this is indicated by the subscript on $\omega$)

$$\omega_k = \overline{\alpha}_s \left[\chi_0 + \overline{\alpha}_s\chi_1 + \overline{\alpha}_s^2\chi_2 + ... + \overline{\alpha}_s^k\chi_k\right] \,. \tag{2.52}$$

Note that we are working under the context of $\omega$ dependent BFKL kernel,

$$\omega = \overline{\alpha}_s \chi^{\omega}(\gamma)\,, \tag{2.53}$$

where it is always possible to introduce the $\omega$ dependency with the kinematical constraint. We now move on to expand the kernel in $\omega$ and keep the format of the terms to find $\omega_{k+1}$

$$\omega_{k+1} = \overline{\alpha}_s \left[\chi^{(0)} + \chi^{(1)}\omega_k + \frac{1}{2!}\chi^{(2)}\omega_k^2 + ... + \frac{1}{k!}\chi^{(k)}\omega_k^k + \frac{1}{(k+1)!}\chi^{(k+1)}\omega_k^{k+1}\right] \,, \tag{2.54}$$

with the $\chi^{(i)}$ is the $i$'th derivative of $\chi^{\omega}$ on $\omega$ set at $\omega=0$ and obviously $\chi_0 = \chi^{(0)}$. Next, we proceed to extract the $\overline{\alpha}_s^{k+2}$ term from (2.54). We note that one needs to keep the terms up to $\omega_k$ on the r.h.s which will contribute to $\omega_{k+1}$.

For an arbitrary term in the $[\dots]$ bracket of (2.54) we can substitute the $\omega_k$ and see

$$\frac{\chi^{(i)}}{i!}\omega_k^i = \frac{\overline{\alpha}_s^i \chi^{(i)}}{i!}\left(\chi_0 + \overline{\alpha}_s\chi_1 + \overline{\alpha}_s^2\chi_2 + \cdots + \overline{\alpha}_s^k\chi_k\right)^i \ . \tag{2.55}$$

In order to find the $\overline{\alpha}_s^{k+2}$ term in (2.54), we need to locate the $\overline{\alpha}_s^{k+1-i}$ term in

$$\left(\chi_0 + \overline{\alpha}_s\chi_1 + \overline{\alpha}_s^2\chi_2 + \cdots + \overline{\alpha}_s^k\chi_k\right)^i \ . \tag{2.56}$$

A general expansion of (2.56) could be formidably complicated. However, by just ignoring their coefficients, we can express an arbitrary term in (2.56) in the following form

$$\prod_{l=0}^{k}\chi_l^{j_l} = \chi_0^{j_0}\chi_1^{j_1}...\chi_k^{j_k} \ , \tag{2.57}$$

with automatically, a constraint associated with the powers $\{j_l\}$

$$\sum_{l=0}^{k} j_l = i. \tag{2.58}$$

Meanwhile, since a single $\chi_l$ term would bring a power of $\overline{\alpha}_s^l$. If we ought to identify the term with the order $\overline{\alpha}_s^{k+1-i}$ in (2.57) , we need a new constraint on that powers $\{j_l\}$, which reads,

$$\sum_{l=0}^{k} j_l l = k+1-i\, . \tag{2.59}$$

Therefore, for a term like eq. (2.57), provided that the leading pole of $\chi_l \sim \frac{1}{\gamma^{2l+1}}$ together with the constraints (2.58), (2.59), its leading pole is given by

$$\prod_{l=0}^{k}\left(\frac{1}{\gamma^{2l+1}}\right)^{j_l} = \left(\frac{1}{\gamma}\right)^{\sum_{l=0}^{k}(2l+1)j_l} = \left(\frac{1}{\gamma}\right)^{(2k+2-i)} \ . \tag{2.60}$$

Furthermore, knowing that every $\chi_l$ in (2.57) doesn't have a subleading pole, we conclude that the subleading pole of this $\overline{\alpha}_s^{k+1-i}$ term also vanishes.

Above all, we can get back to expression (2.55). Seeing that the derivative $\chi^{(i)}$ has the leading pole $\sim \gamma^{-(1+i)}$ and a vanishing subleading pole, we proved that the leading pole in $\chi_{k+1}$ is $\sim \gamma^{-(2k+3)}$, and its $\gamma^{-(2k+2)}$ pole vanishes.

### 2.2.5 Scale changing transformation at NLL and NNLL

In section 2.2.1, we introduced the energy scale effect from the BFKL kernel in the $(\omega, k^2)$ space and formulated the symmetric and asymmetric LL BFKL kernel in the $(\omega, \gamma)$ space,

$$\chi^{\omega,A}(\gamma) = 2\psi(1) - \psi(\gamma) - \psi(1-\gamma+\omega) \;, \tag{2.61}$$

$$\chi^{\omega,S}(\gamma) = 2\psi(1) - \psi\left(\gamma + \frac{\omega}{2}\right) - \psi\left(1-\gamma+\frac{\omega}{2}\right) \;, \tag{2.62}$$

where $A$ and $S$ stand for symmetric and asymmetric respectively. It is rather obvious to implement the scale changing transformation in the $k^2$ space, see eq. (2.31). However, it is worth more effort to investigate the scale changing transformation in the $\omega, \gamma$ space.

Before proceeding to NNLL, we shall see how the scale changing works at NLL. In the following, we assume that the additional dependence on $\omega$ in the $\chi$ function. From a symmetric case to an asymmetric case, we propose a shift to the argument $\gamma \to \gamma - \omega/2$ similar to the LL kernel,

$$\chi_0\left(\gamma - \frac{\omega}{2}\right) + \overline{\alpha}_s \chi_1\left(\gamma - \frac{\omega}{2}\right). \tag{2.63}$$

Using $\omega$ expansion and keeping terms up to NLL, we have

$$\chi_0(\gamma) - \frac{\omega}{2}\frac{\partial\chi_0}{\partial\gamma} + \overline{\alpha}_s\chi_1(\gamma)\,. \tag{2.64}$$

Comparing eq. (2.63) with eq. (2.64), we obtain the scale changing part as

$$T^{\mathrm{NLL}}(\gamma) = -\frac{\omega}{2}\frac{\partial\chi_0}{\partial\gamma} \;, \tag{2.65}$$

At this order, we only need to take leading order $\omega = \overline{\alpha}_s\chi_0(\gamma)$, therefore scale changing transformation in the argument of $\gamma$ is

$$T^{\mathrm{NLL}}(\gamma) = -\frac{1}{2}\overline{\alpha}_s\chi_0(\gamma)\frac{\partial\chi_0}{\partial\gamma} \;, \tag{2.66}$$

see [21, 22, 93]. In the following, we will focus only on the leading collinear and anti-collinear poles in $\gamma$. The pole structure of the scale changing transformation at NLL is given by

$$T^{\mathrm{NLL}}(\gamma) = -\frac{1}{2}\overline{\alpha}_s\chi_0(\gamma)\frac{\partial\chi_0}{\partial\gamma} \sim \frac{\overline{\alpha}_s}{2\gamma^3} - \frac{\overline{\alpha}_s}{2(1-\gamma)^3} \;. \tag{2.67}$$

This scale change (2.67) agrees with the difference between the leading poles of symmetric and asymmetric NLL kernels generated from the $\omega$ expansion of eq. (2.61) and eq. (2.62),

$$\chi_1^S \sim -\frac{1}{2\gamma^3} - \frac{1}{2(1-\gamma)^3} \,, \tag{2.68}$$

$$\chi_1^A \sim \frac{0}{2\gamma^3} - \frac{1}{(1-\gamma)^3} \,. \tag{2.69}$$

In NNLL order, it is necessary to expand (2.63) to the second order in $\omega$ of $\chi_0$ and the first order in $\omega$ in $\chi_1$. We see

$$\chi_0(\gamma) - \frac{\omega}{2}\frac{\partial\chi_0}{\partial\gamma} + \frac{1}{2}\left(\frac{\omega}{2}\right)^2\frac{\partial^2\chi_0}{\partial\gamma^2} + \overline{\alpha}_s\chi_1(\gamma) - \overline{\alpha}_s\frac{\omega}{2}\frac{\partial\chi_1}{\partial\gamma}. \tag{2.70}$$

Now to find NNLL scale changing terms, we need to keep terms in the solution for the $\omega$ at least up to NLL, i.e.,

$$\omega = \overline{\alpha}_s\left[\chi_0\left(\gamma - \frac{\omega}{2}\right) + \overline{\alpha}_s\chi_1\left(\gamma - \frac{\omega}{2}\right)\right] \approx \overline{\alpha}_s\chi_0(\gamma) - \frac{1}{2}\overline{\alpha}_s^2\chi_0\frac{\partial\chi_0}{\partial\gamma} + \overline{\alpha}_s^2\chi_1. \tag{2.71}$$

Substituting the above expansion of $\omega$ into (2.70) and keeping terms up to NNLL, we get for the scale changing transformation at NNLL (see also [94])

$$T^{\mathrm{NNLL}}(\gamma) = -\frac{1}{2}\frac{\partial\chi_0}{\partial\gamma}\left(-\frac{1}{2}\overline{\alpha}_s^2\chi_0\frac{\partial\chi_0}{\partial\gamma}\right) - \frac{1}{2}\overline{\alpha}_s^2\chi_1\frac{\partial\chi_0}{\partial\gamma} + \frac{1}{8}(\overline{\alpha}_s\chi_0)^2\frac{\partial^2\chi_0}{\partial\gamma^2} - \frac{1}{2}\overline{\alpha}_s^2\chi_0\frac{\partial\chi_1}{\partial\gamma} \,. \tag{2.72}$$

We expand the $T^{\mathrm{NNLL}}(\gamma)$ in $\gamma$ and see its pole structure at $\gamma = 0$ and $\gamma = 1$ is

$$T(\gamma) \sim -\frac{1}{2\gamma^5} + \frac{0}{\gamma^4} + \mathcal{O}(\frac{1}{\gamma^3}) \,, \tag{2.73}$$

$$T(\gamma) \sim \frac{3}{2(1-\gamma)^5} + \frac{0}{(1-\gamma)^4} + \mathcal{O}(\frac{1}{(1-\gamma)^3}) \,. \tag{2.74}$$

This result is unchanged whenever we use $\chi_1$ either from the exact N=4 sYM NLL kernel or the NLL kernel derived from $\omega$ expansion. Note the scale changing does not introduce any subleading poles $1/\gamma^4, 1/(1-\gamma)^4$ at NNLL. This is also consistent with the pattern of vanishing subleading poles which was discussed in the last subsection.

The scale changing at NNLL (2.74) is consistent with the difference of the leading poles of $N = 4$ sYM NNLL kernels. We can easily verify that by expanding (2.61) and

(2.62)

$$\chi_2^A \sim \frac{0}{2\gamma^5} + \frac{2}{(1-\gamma)^5}\ , \tag{2.75}$$

$$\chi_2^S \sim \frac{1}{2\gamma^5} + \frac{1}{2(1-\gamma)^5}\ . \tag{2.76}$$

We note that despite it seems it is easier to apply a scale change in the momentum space of $k$ than the Mellin space of $\gamma$, as in eq. (2.31), the above scale transformation can help us explore and verify the poles structure especially when the properties of the kernel can be better understood in the Mellin space.

# Chapter 3
# Structure Functions from the small x Evolution

In this section, we focus on Ciafaloni-Colferai-Salam-Staśto (CCSS) resummation and recap some basic elements from [22, 33, 34]. We will compute the unintegrated gluon density and structure function and perform the fits to HERA data based on CCSS resummation.

As we discussed briefly in the last section, the CCSS resummation features the renormalization group improved (RGI) small $x$ equation. The CCSS resummation is constructed based on the DGLAP collinear splitting function and the exact BFKL up to the NLL accuracy. It contains the contribution from the kinematical constraint and appropriate subtractions to avoid double counting. The above modifications ensure the momentum conservation in this framework. The subtraction in the CCSS resummation is introduced in the Mellin space and later realized in the momentum space. The sequential computation of the unintegrated gluon density is formulated as an interpolation on the expansion of the BFKL equation with triangular functions. The calculations of the structure function and its charm component are carried out, using the perturbative component from the box diagrams and supplemented by the non-perturbative inputs.

## 3.1 The CCSS resummation

### 3.1.1 Construction in the Mellin space

We have introduced some basis for the idea of the CCSS resummation in the last section. However, we have not concluded them in a complete resummed "LL + NLL" form. We will start the construction by resumming the collinear contribution and then move on to incorporate the exact BFKL NLL results with subtractions. This section is essentially a recap of the resummation proposed in [34].

For an easier reach, we present the collinear contributions here again,

$$\chi_n^\omega(\gamma) = \frac{1 \cdot A_1(A_1+b)\cdots[A_1+(n-1)b]}{\left(\gamma+\frac{\omega}{2}\right)^{n+1}} + \frac{1 \cdot A_1(A_1-b)\cdots[A_1-nb]}{\left(1-\gamma+\frac{\omega}{2}\right)^{n+1}}. \tag{3.1}$$

At the LL and NLL, we note

$$\begin{aligned}\chi_0^\omega &\approx \frac{1}{\gamma+\frac{\omega}{2}} + \frac{1}{1-\gamma+\frac{\omega}{2}},\\ \chi_1^\omega &\approx \frac{A_1(\omega)}{\left(\gamma+\frac{\omega}{2}\right)^2} + \frac{A_1(\omega-b)}{\left(1-\gamma+\frac{\omega}{2}\right)^2}.\end{aligned} \tag{3.2}$$

We define

$$\chi_c^\omega = \frac{\chi_1^\omega}{\chi_0^\omega} \simeq \frac{A_1(\omega)}{\gamma+\frac{\omega}{2}} + \frac{A_1(\omega)}{1-\gamma+\frac{\omega}{2}}. \tag{3.3}$$

where the second approximation is derived in the sense for collinear poles ($\gamma+\frac{\omega}{2}\to 0$ and $1-\gamma+\frac{\omega}{2}\to 0$). Note that we have ignored the running of the coupling at this point and apply the frozen $\overline{\alpha}_s$ where $b=0$. The $n$th order collinear contribution is

$$\chi_n^\omega \simeq \chi_0^\omega \left(\chi_c^\omega\right)^n. \tag{3.4}$$

Thus this allows us to resum the all-order collinear contribution

$$\begin{aligned}\chi_\omega &\simeq \sum_{n=0}^{\infty} \overline{\alpha}_s^n \chi_0^\omega \left(\chi_c^\omega\right)^n\\ &= \chi_0^\omega \frac{1}{1-\overline{\alpha}_s\chi_c^\omega}\\ &\simeq \chi_0^\omega + \omega\chi_c^\omega,\end{aligned} \tag{3.5}$$

where we have used the replacement $\omega = \overline{\alpha}_s\chi_0^\omega$. This is the collinear contribution we shall apply to the complete resummed LL + NLL kernel.

Now we proceed to incorporate the exact NLL BFKL kernel in the resummation. To take a better care of running coupling, we first propose a general form in the momentum space of the resummed kernel $\mathcal{K}_\omega$

$$\mathcal{K}_\omega = \overline{\alpha}_s(q^2)\mathcal{K}_0^\omega + \omega\overline{\alpha}_s(k_>^2)\mathcal{K}_c^\omega + \overline{\alpha}_s^2(k_>^2)\tilde{\mathcal{K}}_1^\omega, \tag{3.6}$$

with $k_> = \max(k, k')$ and $k_< = \min(k, k')$. The argument $q^2 = |\mathbf{k} - \mathbf{k}'|^2$ of the running coupling of the LL kernel is the usual choice from the LL BFKL equation. The correspondence between the kernels in the momentum and Mellin space is $\chi_0^\omega \to \mathcal{K}_0^\omega$, $\chi_c^\omega \to \mathcal{K}_c^\omega$, while $\tilde{\mathcal{K}}_1^\omega$ represents everything else that shall be introduced in the resummation and will be determined later.

Now we expand the eq. (3.6) at $\omega = 0$ and adjust the running coupling to the same argument $k^2$,

$$\mathcal{K}_\omega \simeq \overline{\alpha}_s(k^2)\left(\mathcal{K}_0^\omega|_{\omega=0} + \omega\frac{\partial\mathcal{K}_0^\omega}{\partial\omega}\bigg|_{\omega=0} + \omega\mathcal{K}_c^\omega|_{\omega=0}\right) + \overline{\alpha}_s^2(k^2)\left(\tilde{\mathcal{K}}_1^0 + \mathcal{K}_0^{\mathrm{run}}\right), \tag{3.7}$$

where we have taken $\tilde{\mathcal{K}}_1^0 = \tilde{\mathcal{K}}_1^\omega|_{\omega=0}$ as we do not have an explicit form of the $\omega$ dependency of $\tilde{\mathcal{K}}_1^\omega$ yet. The $\mathcal{K}_0^\omega|_{\omega=0} = \mathcal{K}_0^0$ corresponds to the standard LL BFKL kernel in Mellin space $\chi(\gamma) = 2\psi(1) - \psi(\gamma) - \psi(1-\gamma)$. The running coupling term $\mathcal{K}_0^{\mathrm{run}}$ is

$$\mathcal{K}_0^{\mathrm{run}}(\mathbf{k}, \mathbf{k}') = -b\left[\ln\frac{q^2}{k^2}\mathcal{K}_0(\mathbf{k}, \mathbf{k}')\right]. \tag{3.8}$$

The corresponding $\chi_0^{\mathrm{run}}$ in Mellin space is given by

$$\chi_0^{\mathrm{run}} = -\frac{b}{2}(\chi_0' + \chi_0^2). \tag{3.9}$$

This term is given in the sense of regularization [22, 95, 96] (also see more comments for this term in [34]). The last condition we need is to ensure our resummation can lead back to $\omega$-independent LL and NLL gluon Green's function which we have inversed for convenience,

$$\mathcal{G}_\omega^{-1} = \omega - \mathcal{K}_\omega = \omega - \overline{\alpha}_s(k^2)\left(\mathcal{K}_0^0 + \omega\frac{\partial\mathcal{K}_0^\omega}{\partial\omega}\bigg|_{\omega=0} + \omega\mathcal{K}_c^\omega|_{\omega=0}\right) + \overline{\alpha}_s^2(k^2)\left(\tilde{\mathcal{K}}_1^0 + \mathcal{K}_0^{\mathrm{run}}\right). \tag{3.10}$$

For comparison, the inverse of the $\omega$-independent LL and NLL gluon Green's function is simply

$$\mathcal{G}^{-1} = \omega - \overline{\alpha}_s(k^2)\mathcal{K}_0 + \overline{\alpha}_s^2(k^2)\mathcal{K}_1, \tag{3.11}$$

where $K_0$ and $K_1$ are the LL and NLL $\omega$-independent BFKL kernel respectively. Now, we can recognize the resummed kernel $\mathcal{K}_0^0$ and $\mathcal{K}_1^0$ accordingly,

$$\mathcal{K}_0^0 = \mathcal{K}_0,$$

$$\tilde{\mathcal{K}}_1^0 = \mathcal{K}_1 - \mathcal{K}_0^0 \left( \left.\frac{\partial \mathcal{K}_0^\omega}{\partial \omega}\right|_{\omega=0} + \mathcal{K}_c^\omega|_{\omega=0} \right) - \mathcal{K}_0^{\mathrm{run}}. \tag{3.12}$$

In Mellin space, the resumed NLL kernel is

$$\tilde{\chi}_1(\gamma) \;=\; \chi_1(\gamma) + \frac{1}{2}\chi_0(\gamma)\frac{\pi^2}{\sin^2(\pi\gamma)} - \chi_0(\gamma)\frac{A_1(0)}{\gamma(1-\gamma)} + \frac{b}{2}(\chi_0' + \chi_0^2) \;, \tag{3.13}$$

### 3.1.2 The CCSS kernel in the momentum space

With the Mellin transformation,

$$\overline{f}(\omega, k^2) = \int_0^1 \frac{\mathrm{d}x}{x}\, x^\omega\, f(x, k^2)\,, \tag{3.14}$$

$$\tilde{f}(\omega, \gamma) = \int_0^\infty \mathrm{d}k^2 \left(k^2\right)^{-\gamma}\, \overline{f}(\omega, k^2)\,. \tag{3.15}$$

we summarize the CCSS resummed kernel with three main contributions in $(x, k^2)$ space,

$$\begin{aligned} &\mathcal{K}_0^{\mathrm{kc}}(z; \mathbf{k}, \mathbf{k}') \overset{z,\mathbf{q}}{\otimes} f(\frac{x}{z}, k'^2) + \mathcal{K}_0^{\mathrm{coll}}(z; \mathbf{k}, \mathbf{k}') \overset{z,\mathbf{k}'}{\otimes} f(\frac{x}{z}, k'^2) \\ &+ \mathcal{K}_1^{\mathrm{subtr}}(z; \mathbf{k}, \mathbf{k}') \overset{z,\mathbf{k}'}{\otimes} f(\frac{x}{z}, k'^2) \;, \end{aligned} \tag{3.16}$$

where $\mathcal{K}_0^{\mathrm{kc}}$ is the LL BFKL kernel with kinematical constraint, $\mathcal{K}_0^{\mathrm{coll}}$ is the collinear contribution, and $\mathcal{K}_1^{\mathrm{subtr}}$ is the NLL part with subtractions. The convolution with transverse momentum is performed by either $\mathbf{q}$ or $\mathbf{k}'$ for computational convenience.

- The first term in eq. (3.16) is

$$\begin{aligned} &\mathcal{K}_0^{\mathrm{kc}}(z; \mathbf{k}, \mathbf{k}') \overset{z,\mathbf{q}}{\otimes} f(\frac{x}{z}, k'^2) \\ &= \int_x^1 \frac{dz}{z} \int \frac{d^2\mathbf{q}}{\pi \mathbf{q}^2}\, \bar{\alpha}_s(\mathbf{q}^2) \left[ f(\frac{x}{z}, |\mathbf{k}+\mathbf{q}|^2)\, \Theta(\frac{k^2}{z} - k'^2) \,-\, \Theta(k-q) f(\frac{x}{z}, k^2) \right] \;, \end{aligned} \tag{3.17}$$

  with the kinematical constraint in DIS

$$k'^2 \leq \frac{k^2}{z} \;. \tag{3.18}$$

- The second term in eq. (3.16) is

$$\mathcal{K}_0^{\mathrm{coll}}(z; \mathbf{k}, \mathbf{k}') \overset{z,\mathbf{k}'}{\otimes} f(\frac{x}{z}, k'^2) = \int_x^1 \frac{dz}{z} \int_0^{k^2} \frac{dk'^2}{k^2}\, \bar{\alpha}_s(k^2) z \tilde{P}_{gg}(z) f(\frac{x}{z}, k'^2)$$

$$+\int_x^1 \frac{dz}{z} \int_{k^2}^{k^2/z} \frac{dk'^2}{k'^2}\ \bar{\alpha}_s(k'^2) z \frac{k'^2}{k^2} \tilde{P}_{gg}(z\frac{k'^2}{k^2}) f(\frac{x}{z}, k'^2)\ . \tag{3.19}$$

It is responsible for the collinear and anti-collinear contributions with the non-singular part of the splitting function to avoid double counting, since the $1/z$ term in DGLAP has already been incorporated in the LL BFKL,

$$\tilde{P}_{gg}^{(0)} = P_{gg}^{(0)} - \frac{1}{z}\ , \tag{3.20}$$

where the $P_{gg}^{(0)}$ is the DGLAP gluon-gluon splitting function in LO.

- The last term in eq. (3.16) is the NLL part of the BFKL with appropriate subtractions (corresponding to expression in eq. (3.13)),

$$\begin{aligned}
&\int_x^1 \frac{dz}{z} \int dk'^2\ \bar{\alpha}_s^2(k_>^2) \mathcal{K}_1^{\text{subtr}}(z; \mathbf{k}, \mathbf{k}') f(\frac{x}{z}, k'^2) \\
&= \frac{1}{4} \int_x^1 \frac{dz}{z} \int dk'^2\ \bar{\alpha}_s^2(k_>^2) \Bigg\{ \left( \frac{67}{9} - \frac{\pi^2}{3} \right) \frac{1}{|k'^2 - k^2|} \left[ f(\frac{x}{z}, k'^2) - \frac{2k_<^2}{(k'^2 + k^2)} f(\frac{x}{z}, k^2) \right] \\
&\quad + \Bigg[ -\frac{1}{32} \left( \frac{2}{k'^2} + \frac{2}{k^2} + \left( \frac{1}{k'^2} - \frac{1}{k^2} \right) \log \left( \frac{k^2}{k'^2} \right) \right) + \frac{4\text{Li}(1 - k_<^2/k_>^2)}{|k'^2 - k^2|} \\
&\quad -4A_1(0)\text{sgn}(k^2 - k'^2) \left( \frac{1}{k^2} \log \frac{|k'^2 - k^2|}{k'^2} - \frac{1}{k'^2} \log \frac{|k'^2 - k^2|}{k^2} \right) \\
&\quad - \left( 3 + \left( \frac{3}{4} - \frac{(k'^2 + k^2)^2}{32 k'^2 k^2} \right) \right) \int_0^\infty \frac{dy}{k^2 + y^2 k'^2} \log |\frac{1+y}{1-y}| + \frac{1}{k'^2 + k^2} \\
&\quad \left( \frac{\pi^2}{3} + 4\text{Li} \left( \frac{k_<^2}{k_>^2} \right) \right) \Bigg] f(\frac{x}{z}, k'^2) \Bigg\} + \frac{1}{4} 6\zeta(3) \int_x^1 \frac{dz}{z}\ \bar{\alpha}_s^2(k^2) f(\frac{x}{z}, k^2)\ ,
\end{aligned} \tag{3.21}$$

where the $\text{sgn}(k^2 - k'^2)$ is the sign function that returns the sign of its argument.

We further note that the subtracted kernel eq. (3.13) is free of cubic and double poles in $\gamma = 0, 1$. However, there are still some residual single poles that come from the expansion of

$$-\frac{1}{2}\chi_0(\gamma) \frac{\pi^2}{\sin^2(\pi\gamma)} - \chi_0(\gamma) \frac{A_1(0)}{\gamma(1-\gamma)} = \chi_0(\gamma) \left[ -\frac{1}{2\gamma^2} + \frac{A_1(0)}{\gamma} + A_1(0) - \frac{\pi^2}{6} + \mathcal{O}(\gamma) \right]. \tag{3.22}$$

The $\mathcal{O}(1)$ term in the $[\dots]$ in the above expression eq. (3.22) corresponds to the single pole $\mathcal{O}(1/\gamma)$ in NLL subtracted kernel $\tilde{\chi}_1(\gamma)$,

$$\left[A_1(0) - \frac{\pi^2}{6}\right]\frac{1}{\gamma}, \tag{3.23}$$

together with the $\mathcal{O}(1)$ term in the expansion of the LL kernel

$$\chi_0^\omega + \omega\chi_c^\omega \simeq \frac{1+\omega A_1}{\gamma+\frac{\omega}{2}} - \omega C(\omega) + \mathcal{O}(\gamma+\frac{\omega}{2}). \tag{3.24}$$

By defining

$$\begin{aligned} C(\omega) &= -\frac{A_1(\omega)}{\omega+1} + \frac{\psi(1+\omega)-\psi(1)}{\omega}, \\ C(0) &= \frac{\pi^2}{6} - A_1(0), \end{aligned} \tag{3.25}$$

we have the two-loop anomalous dimension $\gamma^{\mathrm{NLL}}$,

$$\begin{aligned} \gamma^{\mathrm{NLL}} &\simeq \frac{\overline{\alpha}_s^2}{\omega}C(0) - \overline{\alpha}_s C(\omega)\gamma^{\mathrm{LL}} \\ &\simeq \frac{\overline{\alpha}_s^2}{\omega}\left\{C(0) - C(\omega)\left[1+\omega A_1(\omega)\right]\right\}, \end{aligned} \tag{3.26}$$

where we have used the LL anomalous dimension $\gamma^{\mathrm{LL}} = \overline{\alpha}_s\left[1+\omega A_1(\omega)\right]/\omega$ from the LO DGLAP anomalous dimension. This shows a violation of the momentum sum rule $\gamma^{\mathrm{NLL}}(\omega=1)=0$. Therefore, we introduce the following subtraction to the NLL kernel,

$$\tilde{\chi}_1^\omega(\gamma) = \tilde{\chi}_1(\gamma) - \left(\frac{1}{\gamma}+\frac{1}{1-\gamma}\right)C(0) + \left(\frac{1}{\gamma+\frac{\omega}{2}}+\frac{1}{1-\gamma+\frac{\omega}{2}}\right)C(\omega)\left[1+\omega A_1(\omega)\right]. \tag{3.27}$$

where its form in the momentum space is calculated in eq. (3.27). We note there is another subtraction scheme introduced to cancel the single pole in the NLL in [34]. We shall apply the scheme above in eq. (3.27) for the following calculations.

The solution to the unintegrated gluon density in the resumed BFKL equation is formed with the interpolation with triangular functions on variables $x$ and $k^2$ as in [34]. We leave the relevant transformation and definitions to the appendix A, together with some details on dealing with boundary terms.

## 3.2 Structure function from the CCSS resummation

Prepared with the calculation of the unintegrated gluon density in the CCSS resummation, we proceed to obtain the structure function $F_2$ to test if we can fit the DIS experimental data well. The $k_T$ factorization theorem, which involves an off-shell matrix element and the unintegrated gluon density, gives the perturbative part of the structure function $F_2$. We present the general expressions of the perturbative contribution in the section 3.2.1.

Meanwhile, the non-perturbative, or soft, regime contribution to the structure function $F_2$ tends to be large and necessary. We parametrize it as the calculation in low momenta of the gluon $k^2$ with the addition of the soft Pomeron contribution. The setup is, in general, similar to the [44], without however the matrix formulation that involves the evolution of quarks (see also [97]). The main difference and improvement with respect to the calculation in [44] and [97] is the implementation of the CCSS resummation in the unintegrated gluon density. For clearer clarification, in [44] and [97], the gluon density was computed from the unified DGLAP and BFKL evolution with kinematical constraint. The CCSS resummation features the improvements by further including the full NLL BFKL with appropriate subtractions.

### 3.2.1 Perturbative contribution

The perturbative contribution to the structure function is given by the $k_T$ factorization theorem [81, 98, 99], with the unintegrated gluon density from section 3.1 being served as the input. The general expressions for the structure function $F_2$ from the $k_T$ factorization is

$$F_2(x, Q^2) = \sum_q e_q^2 \, S_q(x, Q^2) \; , \tag{3.28}$$

where the sum is over the quark flavors involved and $S_q(x, Q^2)$ is given by

$$S_q(x, Q^2) \;=\; \int_x^1 \frac{dz}{z} \int \frac{dk^2}{k^2} \, S^q_{\text{box}} \left(z, m_q^2, k^2, Q^2\right) f\left(\frac{x}{z}, k^2\right) \; , \tag{3.29}$$

where $S^q_{\text{box}}$ is an off-shell photon-gluon partonic cross section. By convoluting with the unintegrated gluon density $f\left(\frac{x}{z}, k^2\right)$, the $S^q_{\text{box}}$ is obtained [44, 100](see also for detailed derivation in [101]),

$$S_q(x, Q^2) = \frac{Q^2}{4\pi^2} \int \frac{dk^2}{k^4} \int_0^1 d\beta \int d\kappa' \alpha_s \left\{ \left[\beta^2 + (1-\beta^2)\right]\right.$$

$$\left(\frac{\boldsymbol{\kappa}}{D_{1q}} - \frac{\boldsymbol{\kappa} - \boldsymbol{k}}{D_{2q}}\right)^2 + \left[m_q^2 + 4Q^2\beta^2(1-\beta)^2\right]$$
$$\left.\left(\frac{1}{D_{1q}} - \frac{1}{D_{2q}}\right)^2\right\} f\left(\frac{x}{z}, k^2\right)\Theta\left(1 - \frac{x}{z}\right). \tag{3.30}$$

Here, the $\boldsymbol{\kappa}$ and $\boldsymbol{k}$ are quark and gluon transverse momenta respectively, and $\beta$ is the variable defined in the Sudakov decomposition of the quark momentum (longitudinal momentum fraction of the photon carried by the quark, see [100]). In addition, it is useful to define the shifted quark transverse momentum $\boldsymbol{\kappa}' = \boldsymbol{\kappa} - (1-\beta)\boldsymbol{k}$. The energy denominators are defined as

$$D_{1q} = \kappa^2 + \beta(1-\beta)Q^2 + m_q^2 \,, \tag{3.31}$$
$$D_{2q} = (\boldsymbol{\kappa} - \boldsymbol{k})^2 + \beta(1-\beta)Q^2 + m_q^2 \,. \tag{3.32}$$

The unintegrated gluon density $f$ is evaluated from Eqs. (3.16),(3.17),(3.19),(3.21). The argument of the unintegrated gluon density is equal to $x/z$ with

$$z = \left[1 + \frac{\kappa'^2 + m_q^2}{\beta(1-\beta)Q^2} + \frac{k^2}{Q^2}\right]^{-1} \,. \tag{3.33}$$

This stems from the exact kinematics in the photon-gluon fusion process, see [100]. The argument of the strong coupling $\alpha_s$ is taken to be $(k^2 + \kappa^2 + m_q^2)$ in our calculation. The masses of quarks are taken to be $m_u = m_d = m_s = 0$ GeV and $m_c = 1.4$ GeV.

In principle, the integration over the transverse momenta in the $k_T$ factorization formula formally extends down to zero into the non-perturbative region. However, it is usually beneficial in phenomenology studies [44, 97] to separate perturbative and non-perturbative regions by introducing the cutoff boundary $k_0^2$. We propose the validity of the formula (3.29) and (3.30) only for the transverse momenta $k^2, \kappa^2 > k_0^2$. The contributions in other regions are introduced in the next subsection. We took the typical cutoff value of $k_0^2 = 1.\,\mathrm{GeV}^2$.

### 3.2.2 Non-perturbative contribution

The structure function $F_2$ receives large soft contribution which is analyzed and modeled in different literature. For instance, [102] simply parametrizes the soft contribution as a constant background term in addition to the perturbative small $x$ part. Meanwhile, in the dipole model, the non-perturbative contribution is usually included automatically by an integration over the large dipole sizes with the flat dipole cross section, for example, [103, 104].

Here we follow the approach of [44]. The non-perturbative contribution is from the low gluon and quark transverse momenta can be parametrized according to the relation between $k^2, \kappa'^2$ and $k_0^2$.

- When both quark momenta and gluon momenta are small $k^2, \kappa'^2 < k_0^2$, we assume that light quark contribution is phenomenologically evaluated as the soft Pomeron exchange [105]. The soft Pomeron contribution for $u, d, s$ quark flavors is modeled,

$$S^{(a)} \;=\; S_u^p \,+\, S_d^p \,+\, S_s^p \;, \tag{3.34}$$

with

$$S_u^p \;=\; S_d^p \;=\; 2S_s^p \;=\; C_p \, x^{-\lambda} \, (1-x)^8, \tag{3.35}$$

where coefficient $C_p$ is a free parameter independent of $Q^2$ and $0 \lesssim \lambda \lesssim 0.1$ is the soft-Pomeron power.

- When the quark momenta are still high but the gluon momenta are rather low, i.e., $k^2 < k_0^2 < \kappa'^2$, we propose the strong ordering approximation at quark-gluon vertex and make use of the collinear approximation

$$S_{\rm box} \;\to\; S_{\rm box}^{(b)} \, (z, k^2 = 0, Q^2), \tag{3.36}$$

therefore,

$$\begin{aligned} S^{(b)} \;&=\; \int_x^1 \frac{{\rm d}z}{z} \, S_{\rm box}^{(b)} \, (z, k^2 = 0, Q^2) \int_0^{k_0^2} \frac{{\rm d}k^2}{k^2} \, f\left(\frac{x}{z}, k^2\right) \\ &=\; \int_x^1 \frac{{\rm d}z}{z} \, S_{\rm box}^{(b)} \, (z, k^2 = 0, Q^2) \, \frac{x}{z} \, g\left(\frac{x}{z}, k_0^2\right) \;, \end{aligned} \tag{3.37}$$

where $xg(x, k_0^2)$ is the non-perturbative input collinear gluon density at the scale $k_0^2$. We will specify the form of its parametrization in section 3.3.

In summary, the complete contribution of the light quarks is,

$$S_q^{(a)} + S_q^{(b)} + S_q^{(c)} \;, \tag{3.38}$$

where the last, perturbative contribution $S_q^{(c)}$ is computed as the eq. (3.30).

### 3.2.3 Charm quark contribution

Besides the light quarks, one needs to include the contribution from the charm quark. The evaluation is again from the $k_T$ factorization.

For the gluon transverse momenta larger than the cutoff $k^2 > k_0^2$, we compute the charm contributions perturbatively in eq. (3.30). In the region $k^2 < k_0^2$, we use on-shell approximation $k^2 = 0$ and obtain

$$\begin{aligned} S_c^{(b)} &= \int_x^a \frac{\mathrm{d}z}{z} S_{\mathrm{box}}(z, k^2 = 0, Q^2; m_c^2) \int_0^{k_0^2} \frac{\mathrm{d}k^2}{k^2} f\left(\frac{x}{z}, k_0^2\right) \\ &= \int_x^a \frac{\mathrm{d}z}{z} S_{\mathrm{box}}(z, k^2 = 0, Q^2; m_c^2) \frac{x}{z} g\left(\frac{x}{z}, k_0^2\right) , \end{aligned} \tag{3.39}$$

where $a = (1 + 4m_c^2/Q^2)^{-1}$ and from [106],

$$\begin{aligned} & S_{\mathrm{box}}(z, k^2 = 0, Q^2; m_c^2) \\ & = \frac{z\alpha_s}{2\pi} \left\{ \ln \frac{1+\xi}{1-\xi} \left[ z^2 + (1-z)^2 + z(1-3z)\frac{4m_c^2}{Q^2} - z^2 \frac{8m_c^4}{Q^4} \right] \right. \\ & \left. + \xi \left[ -1 + 8z(1-z) - z(1-z)\frac{4m_c^2}{Q^2} \right] \right\} , \end{aligned} \tag{3.40}$$

where $\xi^2 = 1 - (4m_c^2/Q^2)z(1-z)^{-1}$. There are two contributions from the charm quark that are dynamically generated from the photon-gluon fusion. We do not consider any contributions from the additional charm quark that are not generated from the gluon.

## 3.3 Fits to HERA data

In this subsection, we present the results of the fits to the structure functions and the properties of the extracted unintegrated gluon distribution function. We perform the fits to the DIS HERA $F_2$ [107] and its charm component data $F_2^c$ [108], as they have already extracted the structure functions from the reduced cross sections.

### 3.3.1 General setup

In this analysis we focus on high energy or low-$x$ physics, therefore we impose the cuts on the data: $Q^2 > 2\ \mathrm{GeV}^2,\ x < 0.01$. With these cuts, we include 170 points for $F_2$ data and 24 points for $F_2^c$ data.

The initial condition $f^{(0)}(x, k^2)$ for the BFKL equation with the CCSS resummation is given by the convolution of the integrated gluon density with the DGLAP splitting function as in [44]

$$f^{(0)}(x,k^2) \;=\; \frac{\alpha_S(k^2)}{2\pi}\int_x^1 dz P_{gg}(z)\frac{x}{z}g\left(\frac{x}{z},k_0^2\right)\;, \tag{3.41}$$

where the $P_{gg}$ is the LO DGLAP splitting function and $xg\,(x,k_0^2)$ is the integrated gluon density at scale $k_0^2$. The scale is fixed to avoid explicit parametrization of the initial term for the unintegrated gluon density in the non-perturbative region $k^2 < k_0^2$. In the case of the unified DGLAP and BFKL calculation, it proved to be very successful and the input could be parametrized with only a few free parameters [44].

The fitted parameters come from either the input gluon distribution $xg$, or the soft Pomeron contribution $S_q^{(a)}$. For the integrated input gluon distribution we consider the form

$$xg(x,k_0^2) = N(1-x)^\beta\left[1 + D\,(x+\epsilon)^\alpha\right]\;, \tag{3.42}$$

where $\epsilon$ is manually set to be a small positive number, to prevent potential negativity of the gluon input function when $D < 0$ and $\alpha < 0$.

The detailed approach of the solution to the resummed BFKL equation is presented in the appendix A, see also [34]. The fitting parameters are powers $\alpha$ and $\beta$, the normalizations $N$ and $D$ in the input gluon distribution eq. (3.42) and the power $\lambda$ and normalization $C_p$ for the soft Pomeron part in eq. (3.34).

The powers $\alpha$ and $\beta$ in the gluon distribution enter non-linearly in eq. (3.42), as a result, their variation requires resolving the resummed equation. The fitting to the powers $\alpha$ and $\beta$ is thus most time consuming. Meanwhile, other parameters are either normalizations or in the modeled soft contribution which does not need integration. Notice that the BFKL equation is in fact additive to the input integrated gluon density $xg\,(x,k_0^2)$. Consequently, the fitting of the parameters other than the non-linear powers is performed quickly.

The charm quark mass $m_c$ is not a free fit parameter in principle. Nevertheless, we have tested the sensitivity of the results to their value by performing several fits with different charm quark masses. We found that the best description of the data is achieved with the charm quark mass $m_c = 1.4\,\text{GeV}$.

### 3.3.2 The fit to the structure function

We are interested in two different scenarios for our fitting.

- In the first one, the fit has been performed to both $F_2$ and $F_2^c$ data simultaneously.
- In the second one, we fit only $F_2$ data, thus the charm structure function $F_2^c$ is left as a prediction.

The resulting parameters of the fit are shown in table 3.1[1] with the chi-squared ($\chi^2$) of the fit. We see that the quality of the fits is great and similar in both scenarios. In addition, the values of the parameters in different scenarios tend to be very close, which demonstrates the stability of the approach.

**Table 3.1.** Fitting parameters for the gluon distribution input and the soft Pomeron contribution.

| Data Range | $\chi^2$ | $C_p$ | $\lambda$ | $N$ | $\beta$ | $\alpha$ | $D$ | $\epsilon$ |
|---|---|---|---|---|---|---|---|---|
| Fit $F_2$,$F_2^c$ | 0.9900 | 0.4420 | 0.01562 | 3.894 | 4.951 | -0.4402 | -0.0281 | 0.0003 |
| Fit $F_2$ | 1.052 | 0.4427 | 0.01557 | 3.887 | 4.950 | -0.4413 | -0.0279 | 0.0003 |

As the fitting results of the two scenarios are very close, in the following, we only present the results obtained when both $F_2$ and $F_2^c$ are fitted.

In fig. 3.1, we plot the structure function $F_2(x, Q^2)$ as a function of $x$ for selected values of $Q^2 = 2, 15, 35, 90, 150, 250$ GeV$^2$. We see that the fit agrees with the experimental data very well. In fig. 3.2, the calculation is shown for the charm structure function $F_2^c$. The red points are the charm component extracted from the experiment assuming extrapolating factors to the full phase space in the HVQDIS scheme and black points in the CASCADE scheme, as proposed in [108]. Again, we see the successful description of the experimental data on the charm structure function. As mentioned earlier, the quality of this description is comparable to the case when the charm is not fitted, but is a prediction.

Note that we only include the data with low inelasticity $y$, when the longitudinal structure function contribution is negligible. In principle, One can include the data on $F_L$ in the calculation. Although their error bars are much larger, we expect them to be much less significant in the fitting. Nevertheless, $F_L$ is still important in further investigation, especially for the low $x$ dynamics of the gluon density. See [109], the improved description of $F_L$ was achieved with low $x$ resummation.

In figs. 3.3 to 3.5, we show the structure function with its separate components $F_2^{(a)}, F_2^{(b)}, F_2^{(c)}$ as in eq. (3.38) as a function of $x$ for selected values of $Q^2 = 150, 15, 5$ GeV$^2$ respectively. The perturbative component, indicated as $F_2^{(c)}$ in figures 3.4 and 3.3

[1]The value of $D$ is corrected compared with our publication [49], where the $D$ is mistaken and the presented value is actually $ND$.

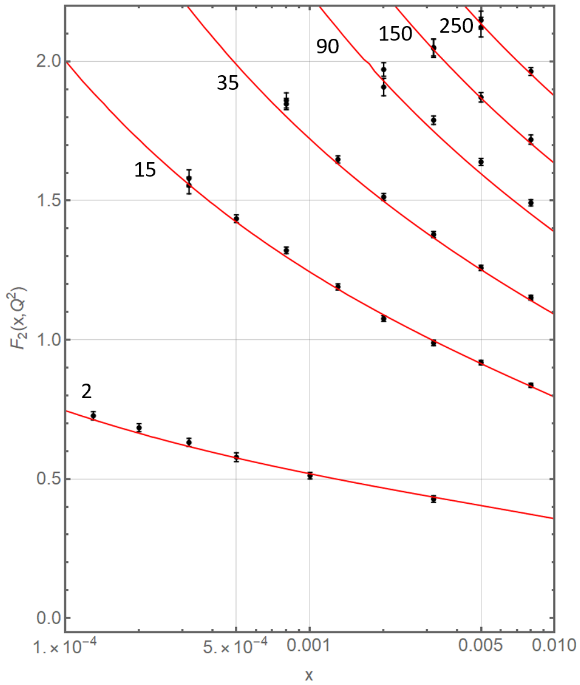


**Figure 3.1.** Structure function $F_2(x, Q^2)$ as a function of $x$ for fixed values of $Q^2 = 2, 15, 35, 90, 150, 250\,\mathrm{GeV}^2$ (with the vertical offsets 0.2 between each curve), indicated next to the curves. Solid red lines correspond to a fit with the CCSS resummed scheme. Experimental data are from Ref. [107].

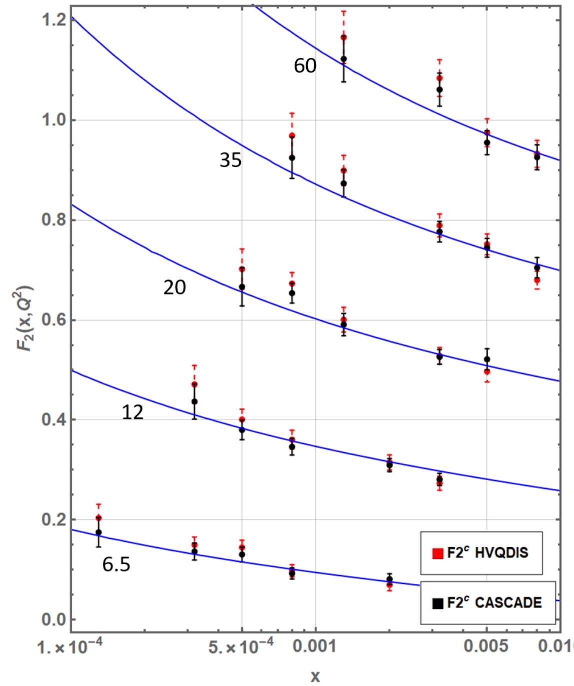


**Figure 3.2.** Charm structure function $F_2^c(x, Q^2)$ as a function of $x$ for fixed values of $Q^2 = 6.5, 12, 20, 35, 60\,\mathrm{GeV}^2$ (with the vertical offsets 0.2 between each curve), indicated next to the curves. Solid blue curve indicates a fit using the CCSS resummed scheme. The experimental data using different phase space extrapolations based on theoretical calculations CASCADE and HVQDIS are from Ref. [108].

dominates at large values of $Q^2$ and small $x$. The two non-perturbative components have very flat dependence on $x$ and contribute to most of the cross section at moderate $x$ and lower $Q^2$. We see that the non-perturbative contribution due to the soft Pomeron is also substantial. For example, it is about 25% at small $x \simeq 5 \times 10^{-4}$ and $Q^2 = 15$ GeV$^2$. Even at high $Q^2$ the soft component is still non-negligible. In the low $Q^2$ region, see fig. 3.5, the non-perturbative components dominate the structure function in a very wide range of $x$, down to $x \sim 3 \times 10^{-4}$. Meanwhile, the perturbative component starts to dominate only at the smallest $x$ for low $Q^2 = 5\,\mathrm{GeV}^2$.

### 3.3.3 The extracted unintegrated gluon density

In figs. 3.6 and 3.7 we show the unintegrated gluon distribution for two fixed values of $x = 0.01, 0.001$ as a function of transverse momentum squared $k^2$. The present calculation

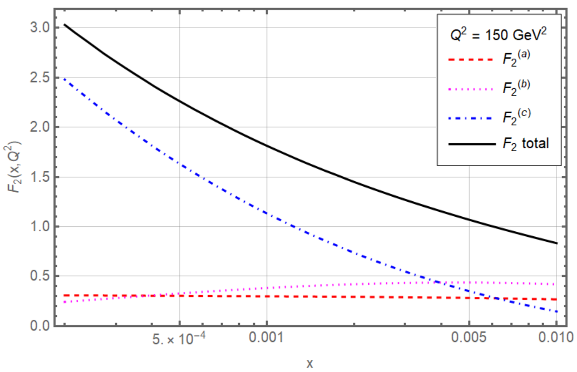


**Figure 3.3.** Structure function $F_2(x, Q^2)$ as a function of $x$ for fixed value of $Q^2 = 150\,\mathrm{GeV}^2$ broken down into various contributions. Red dashed: $F_2^{(a)}$, Eq. (3.34); pink dotted $F_2^{(b)}$, Eq. (3.37); blue dashed-dotted $F_2^{(c)}$, Eq. (3.29). Finally, black solid indicates the sum of all contributions.

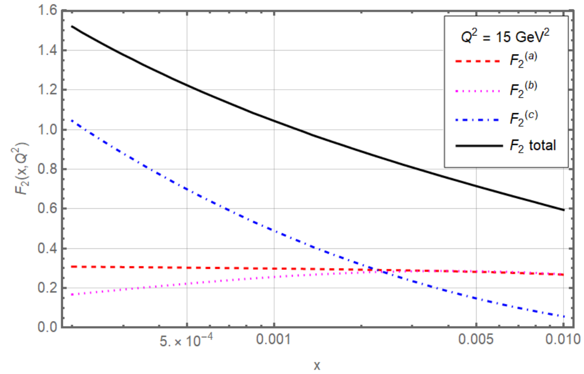


**Figure 3.4.** Structure function $F_2(x, Q^2)$ as a function of $x$ for fixed value of $Q^2 = 15\,\mathrm{GeV}^2$ broken down into various contributions. Red dashed: $F_2^{(a)}$, Eq. (3.34); pink dotted $F_2^{(b)}$, Eq. (3.37); blue dashed-dotted $F_2^{(c)}$, Eq. (3.29). Finally, black solid indicates the sum of all contributions.

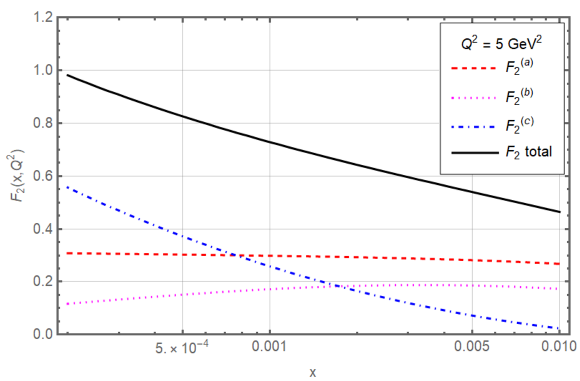


**Figure 3.5.** Structure function $F_2(x, Q^2)$ as a function of $x$ for fixed value of $Q^2 = 5\,\mathrm{GeV}^2$ broken down into various contributions. Red dashed: $F_2^{(a)}$, Eq. (3.34); pink dotted $F_2^{(b)}$, Eq. (3.37); blue dashed-dotted $F_2^{(c)}$, Eq. (3.29). Finally, black solid indicates the sum of all contributions.

based on the CCSS resummation is compared with the extracted gluon distribution from Kutak-Sapeta calculation [97] (called KS for short here) in the linear and non-linear case. The non-linear case refers to the scenarios in which the additional gluon recombinations lead to the non-linear term of the gluon density in the gluon evolution. The KS calculation is similar in its philosophy to the one presented here and is widely used in phenomenology, and thus it is interesting to compare it with the current extraction. The KS calculation is based on the LL BFKL with kinematical constraint and includes DGLAP terms, so the main difference is the NLL part of the BFKL and the type of subtractions performed.

The overall shape in $k^2$ is similar to the CCSS and KS calculation.

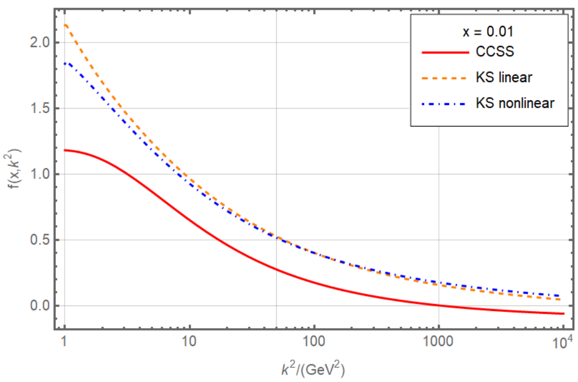


**Figure 3.6.** Unintegrated gluon distribution function extracted from the fit as a function of the transverse momentum squared $k^2$ for fixed $x = 0.01$. Unintegrated gluon from this work based on CCSS resummation (red solid) is compared with the other two models, from Ref. [97], KS linear (dashed orange) and KS non-linear (dashed-dotted blue).

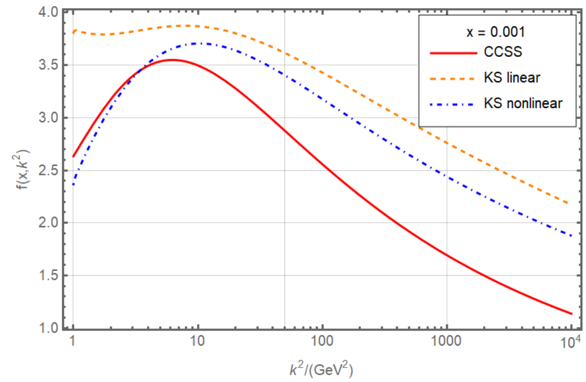


**Figure 3.7.** Unintegrated gluon distribution function extracted from the fit as a function of the transverse momentum squared $k^2$ for fixed $x = 0.001$. Unintegrated gluon from this work based on CCSS resummation (red solid) is compared with the other two models, from Ref. [97], KS linear (dashed orange) and KS non-linear (dashed-dotted blue).

In figs. 3.8 and 3.9 the unintegrated gluon density is shown as a function of $x$ for fixed values of $k^2 = 10, 100, 1000$ GeV$^2$, again compared with the KS-linear and KS-nonlinear calculation. Unsurprisingly, the small $x$ behavior of the CCSS calculation is very close to the KS-linear, whereas both calculations differ substantially from the nonlinear calculation at low $x$ and low $Q^2$ where the saturation corrections are the strongest. There are however some subtle differences between the KS-linear and CCSS calculations which indicate somewhat stronger small $x$ behavior in the CCSS scenario.

The differences between linear and non-linear scenarios are also visualized by taking the ratios between the calculations shown in figs. 3.10 to 3.12. To be precise the ratios CCSS/KS-linear and CCSS/KS-nonlinear are shown as a function of $x$ for three different values of the momentum squared $k^2 = 10, 100, 1000$ GeV$^2$. We see that the CCSS/KS-linear ratio is close to unity, for most values of $x$, whereas the ratio to the calculation which includes the nonlinear effects deviates substantially from unity at low $x$ and low $k^2$. Still, we see again a marked difference, the CCSS calculation tends to have a slightly faster rise towards small $x$. The small $x$ behavior is also illustrated in Figs. 3.13, 3.14 and 3.15, where the effective Pomeron intercept is shown by performing the logarithmic

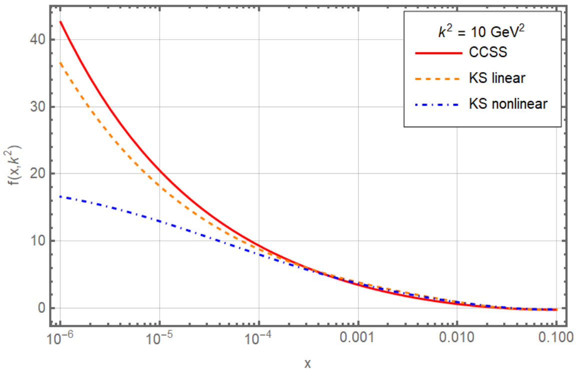


**Figure 3.8.** Unintegrated gluon distribution function extracted from the fit as a function of $x$ for a fixed value of the transverse momentum squared $k^2 = 10\,\mathrm{GeV}^2$. Unintegrated gluon from this work based on CCSS resummation (red solid) is compared with the other two models, from Ref. [97], KS linear (dashed orange) and KS non-linear (dashed-dotted blue).

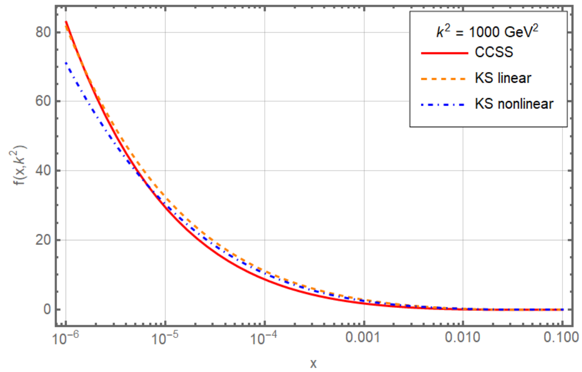


**Figure 3.9.** Unintegrated gluon distribution function extracted from the fit as a function of $x$ for a fixed value of the transverse momentum squared $k^2 = 1000\,\mathrm{GeV}^2$. Unintegrated gluon from this work based on CCSS resummation (red solid) is compared with the other two models, from Ref. [97], KS linear (dashed orange) and KS non-linear (dashed-dotted blue).

derivative of the unintegrated gluon distribution

$$\lambda_{\mathrm{eff}} = \frac{\partial \ln f(x,k^2)}{\partial \ln 1/x} \,. \tag{3.43}$$

It is seen from all plots that the effective power is very close, especially at low $x$ to the linear KS calculation, which is expected, and differs from the non-linear KS, for low $x$ and lowest value of $k^2$. We also see that the power is larger for the CCSS calculation than for the linear KS calculation, which is consistent with previous observations. Asymptotically, for low $x$ and low to moderate $k^2$ the value of the power approaches about 0.3 which is the power observed in HERA data.

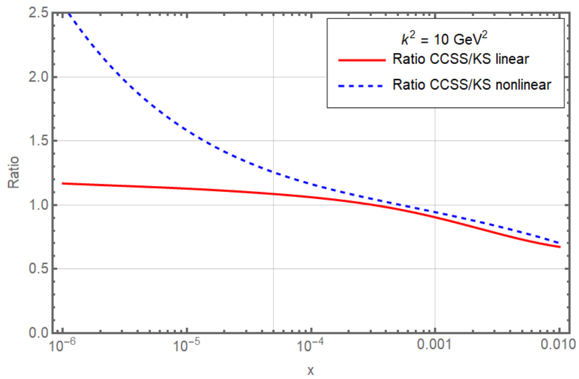


**Figure 3.10.** Ratios of unintegrated gluon distributions as a function of $x$ for fixed value of the transverse momentum $k^2 = 10$ GeV$^2$. Red solid: ratio of the gluon extracted in this work to the KS linear; blue dashed, ratio of the gluon extracted in this work to the KS non-linear.

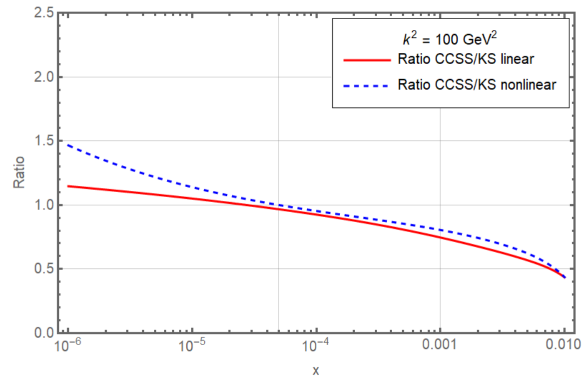


**Figure 3.11.** Ratios of unintegrated gluon distributions as a function of $x$ for fixed value of the transverse momentum $k^2 = 100$ GeV$^2$. Red solid: ratio of the gluon extracted in this work to the KS linear; blue dashed, ratio of the gluon extracted in this work to the KS non-linear.

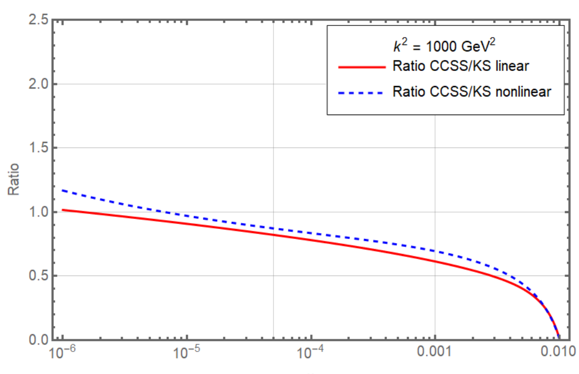


**Figure 3.12.** Ratios of unintegrated gluon distributions as a function of $x$ for fixed value of the transverse momentum $k^2 = 1000$ GeV$^2$. Red solid: ratio of the gluon extracted in this work to the KS linear; blue dashed, ratio of the gluon extracted in this work to the KS non-linear.

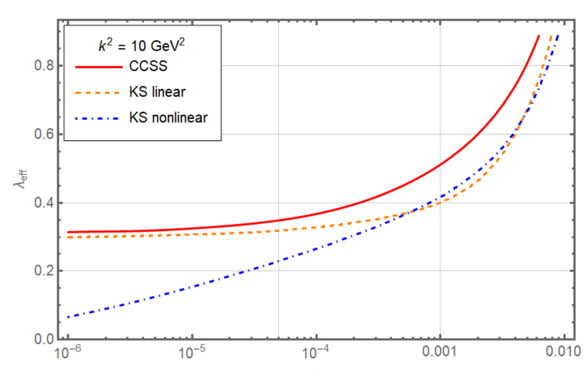


**Figure 3.13.** Effective power $\lambda_{\text{eff}}$ from Eq. (3.43) of unintegrated gluon distribution as a function of $x$ for fixed value of the transverse momentum squared $k^2 = 10$ GeV$^2$. Solid red, this work; orange dashed, KS linear; blue dashed-dotted KS non-linear.

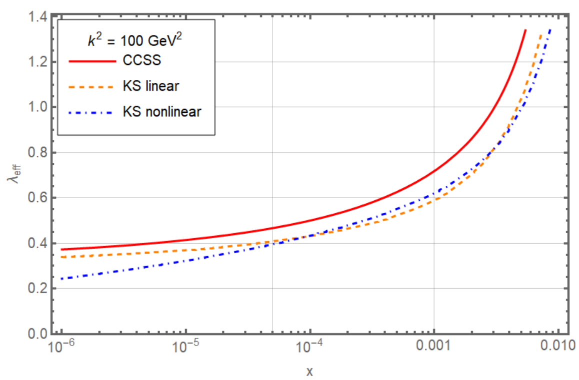


**Figure 3.14.** Effective power $\lambda_{\text{eff}}$ from Eq. (3.43) of unintegrated gluon distribution as a function of $x$ for fixed value of the transverse momentum squared $k^2 = 100\ \text{GeV}^2$. Solid red, this work; orange dashed, KS linear; blue dashed-dotted KS non-linear.

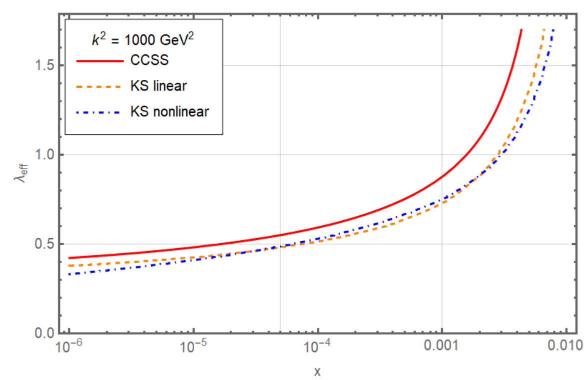


**Figure 3.15.** Effective power $\lambda_{\text{eff}}$ from Eq. (3.43) of unintegrated gluon distribution as a function of $x$ for fixed value of the transverse momentum squared $k^2 = 1000\ \text{GeV}^2$. Solid red, this work; orange dashed, KS linear; blue dashed-dotted KS non-linear.

# Chapter 4
# Resummation of Impact Factors

In chapter 2, we introduced the idea of renormalization group improvements (RGI) motivated by the observation of the dependence on the energy scale choice $s_0$ in the high energy factorization. The scale effect makes up the leading poles contribution $\sim 1/\gamma^3$ to the NLL BFKL eigenfunction in the Mellin space. Later in chapter 3, we further formulated the complete CCSS resummation, which incorporates the kinematical constraints and exact NLL BFKL kernel.

In this chapter, we will consider extending the renormalization group improved resummation to the impact factors $\phi$. This generalization is realized as we notice that the energy scale choice $s_0$ enters the whole high energy factorization cross section integration with both the impact factors and gluon Green's function(GGF).

In particular, we investigate the photon impact factors from the virtual photon-photon scattering. Currently, the photon impact factor is known up to NLO [80, 110] and the corresponding NLO cross section computed has underestimated the experimental data from LEP $e^+e^-$ collider, especially at high rapidity region [83, 110, 111]. In this chapter, we will focus on the improvements to the virtual photon-photon scattering cross section using small $x$ resummation and construct the resummed impact factors accordingly.

## 4.1 From the $e^+e^-$ to $\gamma^*\,\gamma^*$ scattering

The experimental data we shall use later are from L3 and OPAL collaboration at LEP collider [46, 47]. Although we are interested in the high energy factorization of virtual photon-photon scattering cross section, it is beneficial to see the general picture of scattering in these experiments.

In [46, 47], the incoming positron $e^+(p_1)$ and electron $e^-(p_2)$ with the center of mass energy $\sqrt{s_{e^+e^-}} = 189 - 209$ GeV, scatter into the outgoing positron $e^+(p_1')$, electron

$e^-(p_2')$, and the hadron state $X$, as depicted in fig. 4.1.

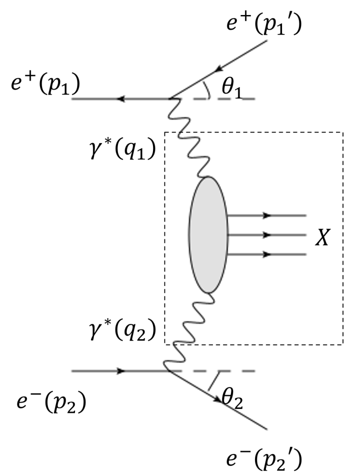


**Figure 4.1.** Diagrammatic representation of the $e^+\, e^- \to e^+\, e^-\, X$ scattering.

Some important kinematics are as follows:

- The virtual photons $\gamma^*$ are emitted from the positron and electron. They undergo scattering into the hadron state $X$. It is this subprocess $\gamma^*\, \gamma^* \to X$ that is of particular interest here, as depicted by the box in fig. 4.1. The momenta of the photons are $q_1$ and $q_2$ and the minus virtualities of the photons are defined as

$$Q_1^2 = -q_1^2, \quad Q_2^2 = -q_2^2. \tag{4.1}$$

- Taking the direction of the electron beam (with the energy $E_b$) as the $z$ axis, we label the polar angles of the outgoing positron (with energy $E_1'$) and electron (with energy $E_2'$) as $\theta_1$ and $\theta_2$, i.e., the scattering is double-tagged.

- We use a convention that defines

$$\begin{aligned} y_1 &= \frac{q_1 q_2}{p_1 q_2} = 1 - \frac{E_1'}{2E_b}\cos^2\frac{\theta}{2}, \\ y_2 &= \frac{q_1 q_2}{p_2 q_1} = 1 - \frac{E_2'}{2E_b}\cos^2\frac{\theta}{2}, \end{aligned} \tag{4.2}$$

  where the masses of the positron and electron are ignored. Note there are different conventions used in literature, we use the same convention as see [112].

- We denote the hadronic invariant mass squared by $s_{\gamma^*\gamma^*} = (q_1 + q_2)^2$. The rapidity $Y$ that measures the length of the gluon ladder in the BFKL approach is defined as

$$Y = \ln\left(\frac{s_{e^+e^-}y_1y_2}{s_0}\right) \simeq \ln\left(\frac{s_{\gamma^*\gamma^*}}{s_0}\right) \tag{4.3}$$

  where a symmetric choice of the energy scale is again $s_0 = Q_1Q_2$. The second approximation is taken with the limit $s_{\gamma^*\gamma^*} \gg Q_1^2,\ Q_2^2$.

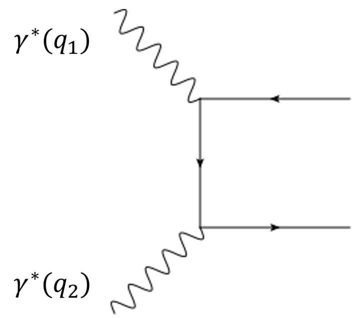


**Figure 4.2.** The lowest order diagram that contributes the subprocess $\gamma^*\ \gamma^*$ scattering.

The lowest order diagram of $\gamma^*\ \gamma^* \to X$ scattering is realized as in fig. 4.2, where it only emits a quark and an antiquark. This diagram is computed with the Cutkosky rule that we introduced in section 1.4.2.1, see fig. 4.3. We refer to the contribution from

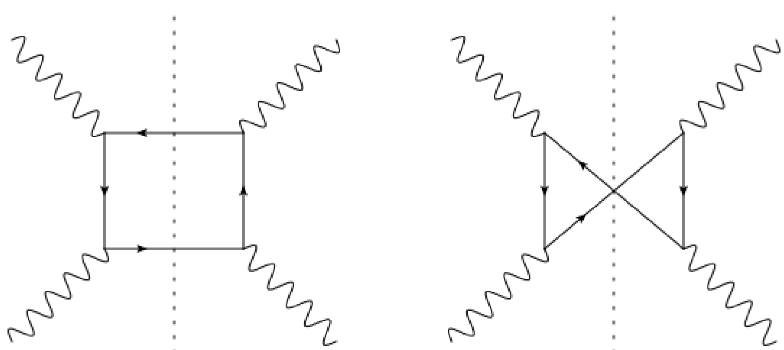

**Figure 4.3.** The lowest order diagram computed with the Cutkosky cut.

these diagrams as the quark box contribution in the later text. The expression for this contribution was derived in [113], see also [114].

Nevertheless, we emphasize the phases characterized by the scales involved in the scattering:

- $Q_1^2 \sim Q_2^2 \gg \mu^2$, when $s_{\gamma^*\gamma^*}$ is not a hard scale,:

Here, the typical hadronic scale $\mu^2$ straightly indicates that this is a perturbative process. We note that the comparable virtualities $Q_1^2 \sim Q_2^2$ yield no large logarithm $\ln(Q_1^2/Q_2^2)$ in the fixed order calculation. The same goes for the energy $s_{\gamma^*\gamma^*}$ and corresponding the logarithm $\ln s_{\gamma^*\gamma^*}$, when $s_{\gamma^*\gamma^*}$ is not hard scale. Therefore, the resummation of the higher order terms is less considered in this regime. The dominant contribution comes from the quark box diagrams in fixed orders.

- $Q_1^2 \gg Q_2^2 \gg \mu^2$:

  $Q_1^2 \gg Q_2^2$ characterizes the collinear limit of the process (or anti-collinear when $Q_2^2 \gg Q_1^2$). Fixed order calculation comes with the large logarithm $\ln(Q_1^2/Q_2^2)$, and thus renormalization group improvements and DGLAP shall be considered to resum the all-order terms.

- $s_{\gamma^*\gamma^*} \gg Q_1^2,\ Q_2^2 \gg \mu^2$:

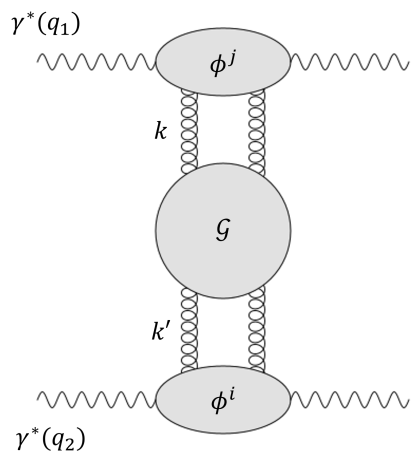


**Figure 4.4.** Diagrammatic representation of high energy factorization of the virtual photon-photon scattering.

The high energy limit (or the high rapidity $Y$) signals the large logarithm $\ln s_{\gamma^*\gamma^*}$ and thus the BFKL dynamics. This is the part we shall focus on and improve in the rest of this chapter. For simplicity, we note $s = s_{\gamma^*\gamma^*}$. The cross section in the high energy factorization can be written into the form of the impact factors $\phi$ and gluon Green's function $\mathcal{G}$, as illustrated in fig. 4.4,

$$\sigma^{(ji)}(s, Q_1, Q_2) = \int \mathrm{d}^2\mathbf{k}\ \mathrm{d}^2\mathbf{k}'\ \phi^{(j)}(Q_1, \mathbf{k})\, \mathcal{G}(s, \mathbf{k}, \mathbf{k}')\, \phi^{(i)}(Q_2, \mathbf{k}') \ , \tag{4.4}$$

where $j, i$ is the polarization of the external photons and $\mathbf{k}$, $\mathbf{k}'$ denotes the transverse momenta of the internal upper and lower gluons. Again, we use the notation $k^2 = \mathbf{k}^2$.

The related Mellin transform of the azimuthally averaged gluon Green's function is given by

$$\mathcal{G}(s,\mathbf{k},\mathbf{k}') = \frac{1}{2\pi k^2}\int \frac{\mathrm{d}\omega}{2\pi i}\left(\frac{s}{s_0}\right)^{\omega}\int \frac{\mathrm{d}\gamma}{2\pi i}\left(\frac{k^2}{k_0^2}\right)^{\gamma}\mathcal{G}(\omega,\gamma)\,, \tag{4.5}$$

- Other regimes, for example, the non-perturbative regime, see discussions in [114].

Besides the quark box and BFKL contributions, the Bremsstrahlung QED radiation diagrams also contribute to the total cross section, as depicted in fig. 4.5. Note that the

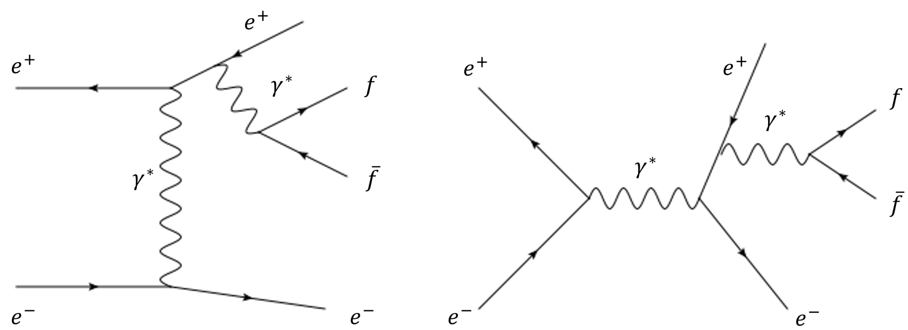


**Figure 4.5.** The Bremsstrahlung radiation $e^+\,e^- \to e^+\,e^-\,f\,\overline{f}$ diagram in the $t$-channel (left) and $s$-chennel (right). $f$ is a fermion and $\overline{f}$ is an anti-fermion.

radiation in fig. 4.5 is allowed on any leg in the diagram. QED radiation is an important factor in the double-tagged $e^+e^-$ scattering in the experiment, especially at the high rapidity. However, it is well modeled and has been subtracted from the experimental group and thus not our focus.

## 4.2 BFKL vs RGI factorization formula

In this section, we shall compare the factorization formulae of the cross section between the pure BFKL formalism and the RGI approach. We aim to derive the compatibility conditions on the respective impact factors and gluon Green's functions, thus preparing us with the prerequisite for the derivation of the RGI impact factors.

The high energy factorization formula for $\gamma^*\gamma^*$ scattering in the Mellin representation with respect to transverse momenta (or virtualities) $Q_1, Q_2$ and the energy scale $s_0$:

$$\begin{aligned}\sigma^{(ji)}(s,Q_1,Q_2) =& \frac{1}{2\pi Q_1 Q_2}\int \frac{\mathrm{d}\omega}{2\pi\mathrm{i}}\left(\frac{s}{s_0(p)}\right)^{\omega}\int \frac{\mathrm{d}\gamma}{2\pi\mathrm{i}}\left(\frac{Q_1^2}{Q_2^2}\right)^{\gamma-\frac{1}{2}} \\ & \phi^{(j)}(\gamma;p)\,\mathcal{G}(\omega,\gamma;p)\,\phi^{(i)}(1-\gamma;-p)\,,\end{aligned} \tag{4.6a}$$

$$\mathcal{G}(\omega, \gamma; p) = \frac{1}{\omega - \bar{\alpha}_s \chi(\gamma; p)} \ , \tag{4.6b}$$

we introduce an additional parameter $p$ to characterize the variance of the energy scale choice $s_0(p) = Q_1^{1+p} Q_2^{1-p}$. By changing the parameter $p$ from -1 to 1, we can switch from the symmetric scale $s_0 = Q_1 Q_2$ $(p = 0)$, to the asymmetric "upper" scale $s_0 = Q_1^2$ $(p = 1)$ or to "lower" scale $s_0 = Q_2^2$ $(p = -1)$.

In eq. (4.6), both impact factors $\phi$ and eigenvalue function $\chi$ are computed perturbatively with the expansion in running coupling $\alpha_{\mathrm{s}}$. In principle, from next-to-leading order on, they also depend on the choice of the energy scale $s_0$:

$$\phi^{(j)}(\gamma; p) = \phi_0^{(j)}(\gamma) + \bar{\alpha}_s \phi_1^{(j)}(\gamma; p) + \mathcal{O}(\bar{\alpha}_s^2) \, , \tag{4.7}$$

$$\chi(\gamma; p) = \chi_0(\gamma) + \bar{\alpha}_s \chi_1(\gamma; p) + \mathcal{O}(\bar{\alpha}_s^2) \ . \tag{4.8}$$

In contrast, the renormalization-group improved (RGI) high-energy factorization is

$$\sigma^{(ji)}(s, Q_1, Q_2) = \frac{1}{2\pi Q_1 Q_2} \int \frac{\mathrm{d}\omega}{2\pi \mathrm{i}} \left( \frac{s}{s_0(p)} \right)^{\omega} \int \frac{\mathrm{d}\gamma}{2\pi \mathrm{i}} \left( \frac{Q_1^2}{Q_2^2} \right)^{\gamma - \frac{1}{2}} \Phi^{(j)}(\omega, \gamma; p) \, G(\omega, \gamma; p) \, \Phi^{(i)}(\omega, 1 - \gamma; -p) \tag{4.9a}$$

$$G(\omega, \gamma; p) = \frac{1}{\omega - \bar{\alpha}_s X(\omega, \gamma; p)} \ . \tag{4.9b}$$

Notice that we introduced some new notations to differentiate the objects in the BFKL and RGI approach, see summary in table 4.1.

**Table 4.1.** Notations of the objects in the standard BFKL and RGI approach respectively.

| | BFKL eigenfunction | gluon Green's function | impact factor |
|---|---|---|---|
| BFKL | $\chi$ | $\mathcal{G}$ | $\phi$ |
| RGI | $X$ | $G$ | $\Phi$ |

The new notation $\omega$-dependent BFKL kernel $X(\omega, \gamma)$ in the RGI factorization (4.9b) is introduced to clearly distinguish it from the BFKL kernel $\chi(\gamma)$ in the standard high-energy factorization, eq. (4.6b). Compared with the standard BFKL expansion, both resummed impact factors $\Phi$ and eigenfunction $X$ are $\omega$-dependent, for two purposes:

- to agree with the known results of $\chi$ and $\phi$ in the collinear limit, at least in the leading logarithmic $\log(Q_1/Q_2)$ approximation;

- to resum into a smoother behavior of the subleading contributions which are singular in some region of the complex $\gamma$-plane.

Actually, the two issues are strictly related, as explained in [34].

Following the scale changing effect illustrated in the LL BFKL kernel eqs. (2.61) and (2.62), a change of the asymmetric energy scale $s_0$ to the symmetric scale with $p = 0$ leaves the cross section (4.9a) invariant under the transformation of the RGI impact factor $\Phi$ and eigenfunction $X$,

$$\Phi^{(j)}(\omega,\gamma;p) = \Phi^{(j)}\Big(\omega,\gamma-\frac{\omega}{2}p;0\Big)\,, \qquad X(\omega,\gamma;p) = X\Big(\omega,\gamma-\frac{\omega}{2}p;0\Big)\,. \tag{4.10}$$

For the $\omega$-independent BFKL impact factors $\phi$ and eigenfunction $\chi$ of eq. (4.6), the scale change would feature more complicated changes.

### 4.2.1 The equivalence between the two factorizations

Prepared with the two factorization formulas, we shall establish the consistency condition between the two approaches. The first step is to evaluate the $\omega$-integrals and require the remaining $\gamma$-integrand to be equivalent (up to higher order terms suppressed by powers of $s$).

In eq. (4.6a) the $\omega$ integration is straightforward: for $s/s_0 > 1$, one can finish the $\omega$-integration via residue theorem and pick up the simple pole of the gluon Green's function $\mathcal{G}$ at $\omega = \bar{\alpha}_s\chi(\gamma)$

$$\sigma^{(ji)}(s,Q_1,Q_2) = \frac{1}{2\pi Q_1Q_2}\int\frac{\mathrm{d}\gamma}{2\pi\mathrm{i}}\left(\frac{s}{s_0}\right)^{\bar{\alpha}_s\chi(\gamma)}\left(\frac{Q_1^2}{Q_2^2}\right)^{\gamma-\frac{1}{2}}\phi^{(j)}(\gamma)\,\phi^{(i)}(1-\gamma)\,. \tag{4.11}$$

In eq. (4.9a), in principle, there can be many $\omega$-poles. The position of the rightmost pole is derived in the same way as in section 2.1.2. It provides the leading high-energy behavior of the cross section and again is determined by,

$$\omega = \bar{\alpha}_s X(\omega,\gamma) \equiv \omega^{\mathrm{eff}}(\gamma,\bar{\alpha}_s) \equiv \bar{\alpha}_s\chi^{\mathrm{eff}}(\gamma,\bar{\alpha}_s)\,, \tag{4.12}$$

where the last expressions $\omega^{\mathrm{eff}} = \bar{\alpha}_s\chi^{\mathrm{eff}}$ represent the solution as effective function $\chi^{\mathrm{eff}}$ of $\gamma$ and $\bar{\alpha}_s$. Therefore, the $\omega$-integral singles out the residue from the gluon Green's function $G$,

$$\mathrm{Res}_{\omega=\omega^{\mathrm{eff}}}[\omega-\bar{\alpha}_s X(\omega,\gamma)]^{-1} = [1-\bar{\alpha}_s\partial_\omega X(\omega^{\mathrm{eff}},\gamma)]^{-1}\,, \tag{4.13}$$

Consequently, the leading term of the cross section with the effective $\chi^{\text{eff}}$ is

$$\sigma^{ji}(s, Q_1, Q_2) = \frac{1}{2\pi Q_1 Q_2} \int \frac{\mathrm{d}\gamma}{2\pi \mathrm{i}} \left(\frac{s}{s_0}\right)^{\bar{\alpha}_s X(\omega^{\text{eff}},\gamma)} \left(\frac{Q_1^2}{Q_2^2}\right)^{\gamma-\frac{1}{2}} \frac{\Phi^{(j)}(\omega^{\text{eff}},\gamma)\,\Phi^{(i)}(\omega^{\text{eff}},1-\gamma)}{1-\bar{\alpha}_s \partial_\omega X(\omega^{\text{eff}},\gamma)} + \cdots \ , \tag{4.14}$$

where the dots indicate the higher order terms suppressed by powers of $s$. Therefore, for any choice of energy scale,

$$\chi(\gamma) = X(\omega^{\text{eff}}, \gamma) \tag{4.15a}$$

$$\phi^{(j)}(\gamma)\phi^{(i)}(1-\gamma) = \frac{\Phi^{(j)}(\omega^{\text{eff}},\gamma)\Phi^{(i)}(\omega^{\text{eff}},1-\gamma)}{1-\bar{\alpha}_s\partial_\omega X(\omega^{\text{eff}},\gamma)} \ . \tag{4.15b}$$

By expanding eq. (4.15) in $\bar{\alpha}_s$ as in eqs. (4.7) and (4.8), we obtain the consistency condition that relates the RGI eigenvalue and impact factors (with their derivatives in $\omega$) at $\omega = 0$ with the BFKL ones:

$$\omega^{\text{eff}} = \bar{\alpha}_s\chi_0(\gamma) + \mathcal{O}(\bar{\alpha}_s^2) \tag{4.16}$$

$$\chi_0(\gamma) = X_0(0,\gamma) \tag{4.17}$$

$$\chi_1(\gamma) = X_1(0,\gamma) + \chi_0(\gamma)\partial_\omega X_0(0,\gamma) \tag{4.18}$$

$$\phi_0^{(j)}(\gamma)\phi_0^{(i)}(1-\gamma) = \Phi_0^{(j)}(0,\gamma)\Phi_0^{(i)}(0,1-\gamma) \tag{4.19}$$

$$\begin{aligned}\phi_0^{(j)}(\gamma)\phi_1^{(i)}(1-\gamma) + \phi_1^{(j)}(\gamma)\phi_0^{(i)}(1-\gamma) = {} & \Phi_0^{(j)}(0,\gamma)\left[\Phi_1^{(i)}(0,1-\gamma) + \chi_0(1-\gamma)\partial_\omega\Phi_0^{(i)}(0,1-\gamma)\right] \\ & + \left[\Phi_1^{(j)}(0,\gamma) + \chi_0(\gamma)\partial_\omega\Phi_0^{(j)}(0,\gamma)\right]\Phi_0^{(i)}(0,1-\gamma) \\ & + \Phi_0^{(j)}(0,\gamma)\Phi_0^{(i)}(0,1-\gamma)\partial_\omega X_0(0,\gamma) \ .\end{aligned} \tag{4.20}$$

We note that eqs. (4.16) to (4.18) are well known from the first studies on RGI BFKL [34]. Equation (4.19) simply gives $\phi_0^{(j)}(\gamma) = \Phi_0^{(j)}(0,\gamma)$ for any polarization $j$.

### 4.2.2 Known results and conventions

To reduce the confusion on the conventions, we note that eqs. (4.6a) and (4.9a) comes with the following normalization for the LO impact factors, compared to those in different literature [79, 82, 83]:

$$\phi_0^{(j)}(\gamma) = \frac{2\pi\sqrt{2(N_c^2-1)}\alpha}{N_f}\left(\sum_q e_q^2\right)\gamma\, h_j(\gamma) \qquad (h_T = \frac{h_2}{\gamma} - h_L) \quad \text{ref [79] Catani et al.} \tag{4.21}$$

$$= \frac{T_R\sqrt{2(N_c^2-1)}}{2}F_j(\nu) \qquad (\gamma = \tfrac{1}{2} + \mathrm{i}\nu) \qquad \text{ref [83] Ivanov et al.} \tag{4.22}$$

$$= \frac{T_R\sqrt{2(N_c^2-1)}}{\pi}\left(\sum_q e_q^2\right) S_j(N=0,\gamma) \quad (N=\omega) \qquad \text{ref [82] Białas et al. ,} \tag{4.23}$$

where $\sum_q$ denotes the sum over quark flavors and $e_q$ is the electric charge of quark $q$ in units of the minus electron charge.

It is worth noting that the values of $N_c = 3$ and $T_R = 1/2$ are usually substituted in. However, we will try to keep them as it can help keep track of the color structure in the later collinear analysis. We present the explicit form of the LO impact factors

$$\phi_0^{(T)}(\gamma) = \alpha\alpha_s\Big(\sum_q e_q^2\Big)T_R\sqrt{2(N_c^2-1)}\,\frac{\pi}{2}\,\frac{(1+\gamma)(2-\gamma)\Gamma^2(\gamma)\Gamma^2(1-\gamma)}{(3-2\gamma)\Gamma(3/2+\gamma)\Gamma(3/2-\gamma)}\,, \tag{4.24a}$$

$$\phi_0^{(L)}(\gamma) = \alpha\alpha_s\Big(\sum_q e_q^2\Big)T_R\sqrt{2(N_c^2-1)}\,\pi\,\frac{\Gamma(1+\gamma)\Gamma(2-\gamma)\Gamma(\gamma)\Gamma(1-\gamma)}{(3-2\gamma)\Gamma(3/2+\gamma)\Gamma(3/2-\gamma)}\,, \tag{4.24b}$$

Both LO impact factors have poles at $\gamma = 0$ and $\gamma = 1$, similarly to the eigenvalue functions $\chi_0$ and $\chi_1$, provided with the $\Gamma$ functions in the numerators.

These poles emerge from the QCD dynamics which, in the collinear limit $Q_1 \gg Q_2$ (o anti-collinear limit $Q_1 \ll Q_2$), generates the logarithmic term $\sim \ln^n(Q_1^2/Q_2^2)$. They correspond to poles of $n+1$th order at $\gamma = 0$ ($\gamma = 1$) in Mellin space. More precisely, the RGI impact factors and eigenvalue function have poles whose order increases as the perturbative order, also see example eq. (2.40),

$$\Phi_n^{(T)}(\omega,\gamma;1) \sim \frac{1}{\gamma^{2+n}}\,, \qquad \Phi_n^{(L)}(\omega,\gamma;1) \sim \frac{1}{\gamma^{1+n}}\,, \qquad X_n(\omega,\gamma;1) \sim \frac{1}{\gamma^{1+n}}\,, \tag{4.25}$$

On the contrary, the corresponding quantities in the standard BFKL with the symmetric energy scale choice $s_0 = Q_1Q_2$ have poles that increase twice as much:

$$\phi_n^{(T)}(\gamma;0) \sim \frac{1}{\gamma^{2+2n}}\,, \qquad \phi_n^{(L)}(\gamma;0) \sim \frac{1}{\gamma^{1+2n}}\,, \qquad \chi_n(\gamma;0) \sim \frac{1}{\gamma^{1+2n}}\,. \tag{4.26}$$

This has been already observed at leading and next-to-leading order for the eigenvalue functions $\chi_0$ and $\chi_1$ in section 2.2. The collinear poles of the NLO impact factors can be derived from the expressions computed in [83]:

$$\begin{aligned}
\frac{\phi_1^{(T)}(\gamma;0)}{\phi_0^{(T)}(\gamma)} &= \frac{\chi_0(\gamma)}{2}\ln\frac{s_0}{Q^2} + \bar{b}\ln\frac{\mu_R^2}{Q^2} \\
&+ \frac{3C_F}{4N_C} - \frac{5}{9}\frac{T_R N_f}{N_C} + \frac{\pi^2}{4} + \frac{85}{36} - \frac{\pi^2}{\sin^2(\pi\gamma)} - \frac{1}{\gamma(\gamma-1)} + \frac{3\chi_0(\gamma)}{2(\gamma+1)(2-\gamma)} \\
&+ \frac{1}{4(1-\gamma)} - \frac{1}{4\gamma} - \frac{7}{36(1+\gamma)} + \frac{5}{3(1+\gamma)^2} - \frac{25}{36(\gamma-2)} \\
&+ \frac{1}{2}\chi_0(\gamma)\left[\psi(1-\gamma) + 2\psi(2-\gamma) - 2\psi(4-2\gamma) - \psi(2+\gamma)\right], \qquad (4.27)\\
\frac{\phi_1^{(L)}(\gamma;0)}{\phi_0^{(L)}(\gamma)} &= \frac{\chi_0(\gamma)}{2}\ln\frac{s_0}{Q^2} + \bar{b}\ln\frac{\mu_R^2}{Q^2} \\
&+ \frac{3C_F}{4N_C} - \frac{5}{9}\frac{T_R N_f}{N_C} + \frac{\pi^2}{4} + \frac{85}{36} - \frac{\pi^2}{\sin^2(\pi\gamma)} - \frac{1-4\gamma}{2\gamma^2(\gamma^2-1)} + \frac{1}{1-\gamma^2}\chi_0(\gamma) \\
&+ \frac{1}{2}\chi_0(\gamma)\left[\psi(1-\gamma) + 2\psi(2-\gamma) - 2\psi(4-2\gamma) - \psi(2+\gamma)\right], \qquad (4.28)
\end{aligned}$$

where $\bar{b}$ is defined in eq. (1.94), $\mu_R$ is the argument of the running coupling $\alpha_s$, and $Q^2 = Q_1 Q_2$.

## 4.3 Resummation of the LO transverse impact factor

We shall make use of eq. (4.20) to derive the NLO RGI impact factors. However, the standard BFKL does not provide the LO $\omega$-dependent eigenvalue and impact factors as well as their derivatives on $\omega$. In this section, we shall use the collinear analysis to obtain the improved LO eigenvalue and impact factors.

### 4.3.1 LO TT cross section in the collinear limits

Collinear analysis can help us find the collinear poles of the cross section, even with $\omega$ dependency as we will see later. The collinear limit of the $\gamma * \gamma *$ scattering is realized with two photons with vastly different virtualities, e.g., $Q_1 \gg Q_2$. This dynamics is well described by effective ladder diagrams, as illustrated in fig. 4.6, where the intermediate propagators are strongly ordered in virtuality (without losing any generality, we assume they decrease from left to right).

We brief the rules of calculation at each QCD vertex as follows:

- The strong coupling is evaluated at a scale given by the largest virtuality of the connected propagators;
- A splitting function $P_{ba}(z_b/z_a)$ describes the fragmentation of the parent parton $a$ (to the right) into a child parton $b$ (to the left) and an emitted on-shell parton (vertical line).

The integrals over the ordered longitudinal momentum fractions $x$ are convolutions, which can be cast into products by a Mellin transform in $1/x = s/Q_1^2 = s/s_0$ for $p = 1$,

$$\sigma^{(ji)}(s, Q_1, Q_2) = \frac{1}{2\pi Q_1 Q_2} \int \frac{\mathrm{d}\omega}{2\pi\mathrm{i}} \left( \frac{s}{Q_1^{1+p} Q_2^{1-p}} \right)^{\omega} \tilde{\sigma}^{(ji)}(\omega, Q_1, Q_2; p) \; . \tag{4.29}$$

which agrees with the structure of eqs. (4.6a) and (4.9a).

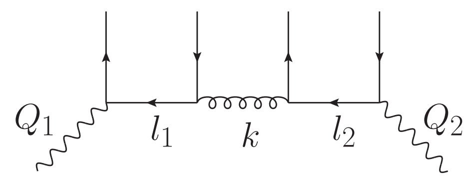


**Figure 4.6.** Ladder diagram depicting collinear limit contributing to the LO BFKL factorization.

The collinear integrand $\tilde{\sigma}^{(TT)}$ for two transverse photons at $\mathcal{O}(\alpha^2\alpha_\mathrm{s}^2)$ — corresponding to the four-rungs LO BFKL diagram with two QCD vertices and two QED vertices — is obtained as

$$\begin{aligned}\tilde{\sigma}^{(TT)}(\omega, Q_1, Q_2; 1) = (2\pi)^3 \alpha \Big( 2 \sum_{q\in A} e_q^2 \Big) \times \\ \int_{Q_2^2}^{Q_1^2} \frac{\mathrm{d}l_1^2}{l_1^2} \frac{\alpha_\mathrm{s}(l_1^2)}{2\pi} P_{qg}(\omega) \int_{Q_2^2}^{l_1^2} \frac{\mathrm{d}k^2}{k^2} \frac{\alpha_\mathrm{s}(k^2)}{2\pi} P_{gq}(\omega) \int_{Q_2^2}^{k^2} \frac{\mathrm{d}l_2^2}{l_2^2} \frac{\alpha}{2\pi} \Big( 2 \sum_{q\in B} e_q^2 \Big) P_{q\gamma}(\omega) \; .\end{aligned} \tag{4.30}$$

where $l_1$, $k$, and $l_2$ are the momenta of the $t$-channel quark, gluon, and quark respectively, as depicted from left to right in fig. 4.6, $A$ and $B$ denote the sets of active quarks of momenta $l_1$ and $l_2$ respectively, while $P_{ab}(\omega)$ denotes the one-loop splitting function in the Mellin space. The running coupling at scale $k^2$ can be expressed in terms of the renormalized coupling $\alpha_\mathrm{s}$ at the given scale $\mu_R$:

$$\alpha_\mathrm{s}(k^2) = \frac{\alpha_\mathrm{s}(\mu_R^2)}{1+\alpha_\mathrm{s}(\mu_R^2) b \ln \frac{k^2}{\mu_R^2}} \simeq \alpha_\mathrm{s}(\mu_R^2)\left(1-\alpha_\mathrm{s}(\mu_R^2) b \ln \frac{k^2}{\mu_R^2} + \cdots\right) , \tag{4.31}$$

Substituting the above expansion for $\alpha_\mathrm{s}(l_1^2)$ and $\alpha_\mathrm{s}(k^2)$ in eq. (4.30) and using the following logarithmic variables $L_i := \ln \frac{Q_i^2}{\mu_R^2}$, $\lambda_i := \ln \frac{l_i^2}{\mu_R^2}$, $\lambda_k := \ln \frac{k^2}{\mu_R^2}$, we have

$$\begin{aligned}\tilde{\sigma}^{(TT)} &= (2\pi)^3 \frac{\alpha^2}{2\pi}\left(\frac{\alpha_\mathrm{s}(\mu_R^2)}{2\pi}\right)^2 \Big(2\sum_{q\in A} e_q^2\Big)\Big(2\sum_{q\in B} e_q^2\Big) P_{qg}(\omega)P_{gq}(\omega)P_{q\gamma}(\omega) \\ &\times \int_{L_2}^{L_1} \mathrm{d}\lambda_1 \int_{L_2}^{\lambda_1} \mathrm{d}\lambda_k \int_{L_2}^{\lambda_k} \mathrm{d}\lambda_2 \,\Big[1-\alpha_\mathrm{s}(\mu_R^2) b(\lambda_1+\lambda_k) + \mathcal{O}(\alpha_\mathrm{s}^2)\Big] \;. \end{aligned} \tag{4.32}$$

The 3-dimension integral in the second line of eq. (4.32) can be calculated up to $\mathcal{O}(\alpha_\mathrm{s})$,

$$\iiint = \frac{(L_1-L_2)^3}{3!}\Big[1-\alpha_\mathrm{s}(\mu_R^2) b(L_1+L_2)\Big] - \alpha_\mathrm{s}(\mu_R^2) b \frac{(L_1-L_2)^4}{4!} + \mathcal{O}(\alpha_\mathrm{s}^2) \;.$$

Notice that

$$\alpha_\mathrm{s}^2(\mu_R^2)\Big[1-\alpha_\mathrm{s}(\mu_R^2) b(L_1+L_2)\Big] = \alpha_\mathrm{s}^2(Q_1Q_2) + \mathcal{O}(\alpha_\mathrm{s}^4) \;,$$

by including the $\alpha_\mathrm{s}^2(\mu_R^2)$ in the first line of eq. (4.32) with 3-dimension integral, we obtain

$$\alpha_\mathrm{s}^2(\mu_R^2)\iiint \simeq \alpha_\mathrm{s}^2(Q_1Q_2)\left[\frac{(L_1-L_2)^3}{3!} - \alpha_\mathrm{s} b \frac{(L_1-L_2)^4}{4!} + \mathcal{O}(\alpha_\mathrm{s}^4)\right] , \tag{4.33}$$

$$\simeq \alpha_\mathrm{s}^2(Q_1Q_2)\left[\frac{1}{3!}\log^3\frac{Q_1^2}{Q_2^2} - \alpha_\mathrm{s} b \frac{1}{4!}\log^4\frac{Q_1^2}{Q_2^2} + \mathcal{O}(\alpha_\mathrm{s}^4)\right] \;. \tag{4.34}$$

Knowing that $(L_1-L_2)^n = \ln^n \frac{Q_1^2}{Q_2^2}$ becomes $\frac{n!}{\gamma^{n+1}}$ under Mellin transform, we have

$$\alpha_\mathrm{s}^2(Q_1Q_2)\frac{1}{\gamma^4}\left[1-\alpha_\mathrm{s} b\frac{1}{\gamma}\right] \;. \tag{4.35}$$

The first term $\mathcal{O}(\alpha_\mathrm{s}^2/\gamma^4)$ could have been obtained even if we use a fixed coupling constant in eq. (4.30). The running coupling is then responsible for the second ($b$-dependent) term $\mathcal{O}(\alpha_\mathrm{s}^3/\gamma^5)$. This will be important term in the later analysis of the NLO impact factors.[1]

Finally, by restoring all the factors of eq. (4.32), i.e., the splitting functions and other

[1] If one chooses a different scale for the running coupling, the coefficient of the $b$-dependent term in eq. (4.35) would change accordingly.

coefficients, we obtain $\tilde{\sigma}^{(TT)}$ in the Mellin space of eq. (4.30) (the Mellin transform with respect to the variable $Q_1^2/Q_2^2$), expanded at order $\alpha_s^2$,

$$
\begin{aligned}
\tilde{\tilde{\sigma}}_0^{(TT)}(\omega,\gamma;1)\Big|^{\text{coll}} &= \Phi_0^{(T)}\,\mathcal{G}_0\,\Phi_0^{(T)}\Big|_{p=1}^{\text{coll}} \\
&= (2\pi)^3\alpha\Big(2\sum_{q\in A}e_q^2\Big)\frac{1}{\gamma}\;\cdot\;\frac{\alpha_s}{2\pi}\frac{P_{qg}(\omega)}{\gamma}\;\cdot\;\frac{\alpha_s}{2\pi}\frac{P_{gq}(\omega)}{\gamma}\;\cdot\;\frac{\alpha}{2\pi}\Big(2\sum_{q\in B}e_q^2\Big)\frac{P_{q\gamma}(\omega)}{\gamma}\,.
\end{aligned}
\tag{4.36}
$$

This is the integrand of the RGI factorization formula (4.9a) in the collinear limit $\gamma\to 0$.

Some remarks are as follows:

*(i)* The collinear analysis of the cross section is essentially based on the DGLAP chain, from the above analysis, it singles out the leading logarithmic behavior in the ratio $Q_1/Q_2$. As we expected, eq. (4.36) agrees with the leading $\gamma$-pole structure of the RGI integrand at $\gamma\to 0$.

*(ii)* The above pole structure correspond to $p=1$, i.e., energy scale $s_0=Q_1^2$. If we adopt the symmetric energy scale $s_0=Q_1Q_2$ ($p=0$), according to eq. (4.10), we need to shift the pole at $\gamma=0$ to $\gamma=-\omega/2$, while the coefficient remains unchanged.

*(iii)* In the anti-collinear limit $Q_1\ll Q_2$, one can obtain the same result of eq. (4.36), with the replacement of $\gamma\to 1-\gamma$ and $p\to -1$, i.e., $s_0=Q_2^2$.

At the symmetric energy scale $s_0=Q_1Q_2$, the pole at $\gamma=1$ is shifted at $\gamma=1+\omega/2$.

In collinear limit $p=1$, i.e., $s_0=Q_1^2$, the pole at $\gamma=1$ is shifted at $\gamma=1+\omega$.

*(iv)* The two sums with electric charges $e_q$ are over quark flavors ($q\in\{u,d,\dots\}$), while a factor of 2 is associated with each sum to take account of both the quark and antiquark contributions.

Therefore, with energy scale $s_0=Q_1^2$ ($p=1$) and including both collinear and anti-collinear contributions, the pole structure at LO of the RGI improved cross section is

$$
\begin{aligned}
\tilde{\tilde{\sigma}}_0^{(TT)}(\omega,\gamma;1)\Big|^{2\times\text{coll}} = {}&(2\pi)^3\alpha\Big(2\sum_q e_q^2\Big)\frac{1}{\gamma}\cdot\frac{\alpha_s}{2\pi}\frac{P_{qg}(\omega)}{\gamma}\cdot\frac{\alpha_s}{2\pi}\frac{P_{gq}(\omega)}{\gamma}\cdot\frac{\alpha}{2\pi}\Big(2\sum_q e_q^2\Big)\frac{P_{q\gamma}(\omega)}{\gamma} \\
&+\Big(\gamma\to 1+\omega-\gamma\Big)\,.
\end{aligned}
\tag{4.37}
$$

We present the expressions of the splitting functions in Mellin space with powers expansion series in $\omega$ as follows:

$$P_{qq}(\omega) = C_F\left(\frac{5}{4} - \frac{\pi^2}{3}\right)\omega + \mathcal{O}(\omega^2) \tag{4.38}$$

$$P_{gq}(\omega) = \frac{2C_F}{\omega}\left[1 + \omega A_{gq}(\omega)\right] \qquad A_{gq}(0) = -\frac{3}{4} \tag{4.39}$$

$$P_{qg}(\omega) = \frac{2}{3}T_R\left[1 + \omega A_{qg}(\omega)\right] \qquad A_{qg}(0) = -\frac{13}{12} \tag{4.40}$$

$$P_{gg}(\omega) = \frac{2C_A}{\omega}\left[1 + \omega A_{gg}(\omega)\right] \qquad A_{gg}(0) = -\frac{11}{6} + \bar{b}\,, \quad \bar{b} = \frac{11}{12} - \frac{T_R N_f}{3N_c} \tag{4.41}$$

$$P_{q\gamma}(\omega) = \frac{N_c}{T_R}P_{qg}(\omega)\,. \tag{4.42}$$

Note that $P_{qg}$ refers to the process where a gluon produces a single quark emitting an antiquark, or vice versa. Therefore, a gluon splitting into a quark or antiquark of a given flavor requires a factor of 2. If the (anti-) quark splits into a gluon, an additional factor $N_f$ shall be present accounting for the sum over flavors. On the other hand, if the (anti-)quark couples to a photon, the sum over flavors gives a factor $\sum_q e_q^2$. eq. (4.42) stems from the fact that, if a gluon of color $c$ splits into a quark-antiquark pair with colors $a, b$, then the squared matrix element contains $\sum_{ab} t^c_{ab} t^{d*}_{ab} = \mathrm{tr}(t^c t^d) = T_R \delta_{cd}$, where $t$ is the matrix in the fundamental and adjoint representations of the SU(3) color group. Meanwhile, when a photon splits into a quark-antiquark pair, the sum over colors is $\sum_{ab}\delta_{ab}\delta_{ab} = \sum_a \delta_{aa} = N_c$.

By substituting eqs. (4.39) to (4.42) and $C_F N_c = (N_c^2-1)T_R$, we can rewrite eq. (4.37) as

$$\begin{aligned}\tilde{\tilde{\sigma}}_0^{(TT)}(\omega,\gamma;1) = \Bigg[&\alpha\alpha_{\mathrm{s}}\Big(\sum_q e_q^2\Big)2P_{qg}(\omega)\sqrt{2(N_c^2-1)}\left(\frac{1}{\gamma^2} + \frac{1}{(1+\omega-\gamma)^2}\right)\Bigg]^2 \\ &\times \frac{1}{\omega}\Big(1 + \omega A_{gq}(\omega)\Big) + \mathcal{O}(\gamma^{-3}) + \mathcal{O}((1+\omega-\gamma)^{-3})\,,\end{aligned} \tag{4.43}$$

where we are only interested in the quartic poles in $\gamma$.

The term in square brackets agrees exactly with the $\omega$-dependent LO impact factor derived from eq. (4.23) in the collinear limit, i.e., it represents the double poles of Białas, Navelet and Peschanski (BNP) impact factor [82] for a transverse photon with their *full $\omega$-dependent coefficient*:

$$\Phi^{(T)}_{\mathrm{BNP}}(\omega,\gamma) = \alpha\alpha_{\mathrm{s}}\Big(\sum_q e_q^2\Big)T_R\sqrt{2(N_c^2-1)}\,\frac{\pi\Gamma(\gamma+\delta)\Gamma(\gamma)}{\Gamma(\omega)}\,\frac{1}{(\delta^2-1)\,(\delta^2-4)}$$

$$
\cdot \left\{ \frac{\psi(\gamma+\delta)-\psi(\gamma)}{\delta} \frac{\omega^2 \left[3(\omega+1)^2+9\right] - 2\omega\left(\delta^2-1\right) + \left(\delta^2-1\right)\left(\delta^2-9\right)}{4\omega} \right.
$$

$$
\left. - \frac{3(\omega+1)^2+3+(\delta^2-1)}{2} \right\} \tag{4.44}
$$

$$
= C_0 \left[ \frac{1+\omega A_{qg}}{\gamma^2} + \frac{D(\omega)}{\gamma} + \mathcal{O}(\gamma^0) \right] + (\gamma \to 1+\omega-\gamma) \tag{4.45}
$$

$$
C_0 = \alpha\alpha_{\mathrm{s}} \Big( \sum_q e_q^2 \Big) \frac{4}{3} T_R \sqrt{2(N_c^2-1)},
$$

$$
D(\omega) = \frac{7}{6} + \mathcal{O}(\omega) \ , \quad \delta \equiv \omega + 1 - 2\gamma \ . \tag{4.46}
$$

The factor $1/\omega$ — stemming from $P_{gq}(\omega)$ — in the second line of eq. (4.43) represents the gluon Green's function eq. (4.9b) at lowest order ($\alpha_{\mathrm{s}} \to 0$), while the finite part $\propto A_{gq}$ provides an NLL correction, to be taken into consideration later.[2]

Above all, the pole structure of the integrand reads,

$$
\tilde{\tilde{\sigma}}_0^{(TT)}(\omega,\gamma;1) = C_0^2 \frac{1}{\omega} \left[ \frac{(1+\omega A_{qg})^2 \, (1+\omega A_{gq})}{\gamma^4} + \mathcal{O}(\gamma^{-3}) \right] + (\gamma \to 1+\omega-\gamma) \ . \tag{4.47}
$$

### 4.3.2 LO RGI transverse impact factor

With the knowledge of the pole structure in the last subsection, we proceed to construct "full" LO impact factors. By "full", we mean that we shall supplement the lower order terms besides the poles, possibly by topping the known result with the improvements from the collinear analysis.

The improved term is evident from eq. (4.43). If we expand the LO transverse BNP impact factors [82] times the LL gluon Green's function in the collinear limit, we see that it is exactly the same as eq. (4.43) expect for an extra factor $P_{gq}(\omega)/P_{gq}(0) = (1+\omega A_{gq})$. Thus the full integrand of the resummed cross section can be constructed as

$$
(1+\omega A_{gq}) \Phi_{\mathrm{BNP}}^{(T)} \, \mathcal{G} \, \Phi_{\mathrm{BNP}}^{(T)}. \tag{4.48}
$$

The next step is to attribute the improvement term $(1+\omega A_{gq})$ to either impact factors or the gluon Green's function. Since this factor stems from the quark-gluon interaction, while the LL GGF is determined by pure gluon dynamics in BFKL, it is natural to associate such a factor to the impact factors. For each resummed impact factor, with the

[2] In the $\omega \to 0$ limit, eq. (4.43) reduces to the product of the LL GGF $1/\omega$ with the LO impact factors $\phi_0^{(T)}(\gamma)\phi_0^{(T)}(1-\gamma)$ of Catani et al. as in eq. (4.21) — restricting $\phi_0^{(T)}$ to the double poles in $\gamma$.

improving factor expanded up to $\mathcal{O}(\omega)$, we can build the resummed transverse impact factor in the simplest way,

$$\Phi_0^{(T)}(\omega,\gamma;1) = \Phi_{\rm BNP}^{(T)}(\omega,\gamma)\left[1+\frac{\omega}{2}A_{gq}(\omega)\right] \tag{4.49}$$

However, it shall be noted that the attribution of the improvements is, in principle, ambiguous. We shall explore the general rules for the flexibility as the collinear analysis only provides constraints for the leading twist poles, i.e., for $\gamma \simeq 0$ and $\gamma \simeq 1+\omega$, of their products. We start by parametrizing the leading-twist poles of $\Phi_0^{(T)}$ as follows:[3]

$$\Phi_0^{(T)}(\omega,\gamma;1) = C_0\left[\frac{1+\omega B(\omega)}{\gamma^2}+\frac{D(\omega)}{\gamma}+\frac{1+\omega\bar{B}(\omega)}{(1+\omega-\gamma)^2}+\frac{\bar{D}(\omega)}{1+\omega-\gamma}\right]+r(\omega,\gamma)\ . \tag{4.50}$$

Here $r(\omega,\gamma)$ collects the remaining terms and has no leading-twist poles. The integrand for the cross section, for $\gamma \simeq 0$, is then

$$\begin{aligned}\tilde{\tilde{\sigma}}_0^{(TT)}(\omega,\gamma;1) &= \Phi_0^{(T)}(\omega,\gamma;1)\,\frac{1}{\omega}\,\Phi_0^{(T)}(\omega,1+\omega-\gamma;1)\\ &= C_0^2\frac{1}{\omega}\left[\frac{(1+\omega B)(1+\omega\bar{B})}{\gamma^4}+\mathcal{O}(\gamma^{-3})\right]+(\gamma\to 1+\omega-\gamma)\ .\end{aligned} \tag{4.51}$$

Comparing the above expression with eq. (4.47) we get a constraint from our parametrization

$$(1+\omega B)(1+\omega\bar{B}) = (1+\omega A_{qg})^2(1+\omega A_{gq}) \tag{4.52a}$$

$$\Longrightarrow \quad B+\bar{B} = 2A_{qg}+A_{gq}+\mathcal{O}(\omega)\ . \tag{4.52b}$$

In the following, we often neglect the subleading terms $\mathcal{O}(\omega)$ in eq. (4.52b) for simplicity.

Unfortunately, the coefficients $D(\omega)$ and $\bar{D}(\omega)$ of the simple poles are not available in the present LO collinear analysis. However, their value at $\omega=0$ can be determined from the explicit expression of eq. (4.24a) in ref. [79]: $D(0)=\bar{D}(0)=7/6$ [cfr. eq. (4.46)]. The simplest and more natural choice for us is to adopt $D(\omega)=\bar{D}(\omega)$ as in the impact factor $\Phi_{\rm BNP}^{(T)}$ of eq. (4.44).

According to the constraints previously derived, we present some possible choices of the transverse LO RGI impact factor, whose differences have to be considered a

[3]We use the convention of parametrizing coefficients of the collinear and anti-collinear poles with the same letter, but with a bar over the coefficients of the anti-collinear poles.

resummation-scheme ambiguity: [4]

$$\Phi_0^{(T)}(\omega,\gamma;1) = \Phi_{\rm BNP}^{(T)}(\omega,\gamma)\left[1+\frac{\omega}{2}A_{gq}(\omega)\right] \qquad \text{(scheme I)} \tag{4.53a}$$

$$\Phi_0^{(T)}(\omega,\gamma;1) = \Phi_{\rm BNP}^{(T)}(\omega,\gamma) + C_0\frac{\omega}{2}A_{gq}(\omega)\left[\frac{1}{\gamma^2}+\frac{1}{(1+\omega-\gamma)^2}\right] \qquad \text{(scheme II)} \tag{4.53b}$$

$$\Phi_0^{(T)}(\omega,\gamma;1) = \Phi_{\rm BNP}^{(T)}(\omega,\gamma) + C_0\,\omega A_{gq}(\omega)\frac{1+\omega A_{qg}}{(1+\omega-\gamma)^2} \qquad \text{(scheme III)}\ . \tag{4.53c}$$

The remarks about these schemes are as follows:

- Scheme I is an overall renormalization of the impact factor, as we introduced earlier for an example.
- Scheme II just modifies the coefficient of the (leading-twist) double poles.
- Scheme III is motivated by the fact that the $P_{gq}$ vertex is attached to the impact factor to the right, thus providing a $1/\gamma$ pole only to $\Phi_0(\omega, 1-\gamma)$.
- The Schemes I and II preserve the $\gamma \leftrightarrow 1-\gamma$ symmetry of the impact factor, while scheme III does not. In particular $B = \bar{B} = A_{qg} + A_{gq}/2$ in schemes I and II, while $B = A_{qg}$, $\bar{B} = A_{qg} + A_{gq} + \omega A_{qg} A_{gq}$ in scheme III (which fulfills exactly eq. (4.52a)).

## 4.4 Resummation of the NLO transverse impact factor

### 4.4.1 NLO TT cross section in the collinear limit

In this section, we shall determine the transverse impact factors at NLO. Specifically, we want to construct a function $\Phi_1^{(T)}(\omega,\gamma)$ such that

- the RGI cross section (4.9a) agrees with the NLL BFKL one (4.6a);
- the same RGI cross section agrees with the DGLAP cross section in the collinear limits $Q_1 \gg Q_2$ and $Q_1 \ll Q_2$ up to $\alpha_s^\ni$.

The first condition has already been considered by comparing the equivalence of the BFKL and RGI approaches. It is formulated as the constraint in eq. (4.20) at $\omega = 0$.

The second condition determines the structure of the collinear poles ($\gamma \simeq 0$ and $\gamma \simeq 1+\omega$) of the impact factors where we have chosen the asymmetric energy scale. We

[4] Other schemes can be considered, see sec. 4.4.1.

start by investigating the $\mathcal{O}(\alpha_s^3)$ integrand, i.e., generalizing the eq. (4.37) with diagrams with more emissions. The relevant ladder diagrams with five splittings between the

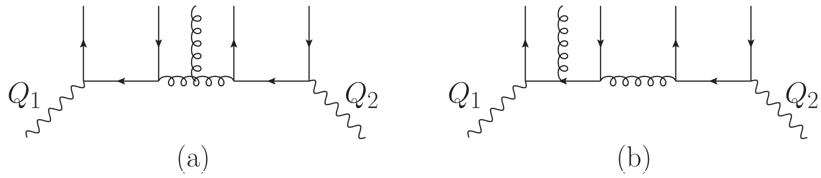


**Figure 4.7.** Relevant ladder diagrams in the collinear limit in the NLO BFKL factorization. We omit the third diagram that is the left-right symmetric of (b), i.e., with the gluon emitted from the quark line on the right.

photons are illustrated in fig. 4.7. The vertices at the external photons are QED couplings as in the LO case. Such diagrams, together with the running-coupling term of eq. (4.35), provide the integrand of the RGI factorization formula at $\mathcal{O}(\alpha_s^3)$ in the collinear limit

$$\alpha_s\,\tilde{\tilde{\sigma}}_1^{(TT)}(\omega,\gamma;1) = \tilde{\tilde{\sigma}}_0^{(TT)}(\omega,\gamma;1)\left[\frac{\alpha_s}{2\pi}\frac{P_{gg}}{\gamma} + 2\frac{\alpha_s}{2\pi}\frac{P_{qq}}{\gamma} - \frac{\alpha_s b}{\gamma} + \mathcal{O}(\gamma^0)\right] , \tag{4.54}$$

where $\tilde{\tilde{\sigma}}_0^{(TT)}$ is the LO (collinear) integrand defined in eq. (4.36).

The calculation rules are the same as the collinear analysis of the LO diagram. The first term of eq. (4.54) stems from the diagram of fig. 4.7a which involves a $P_{gg}$ splitting function. According to the analysis of CCSS [34], this contribution can be entirely associated with the gluon Green's function.

Similar to eq. (3.5), at fixed $\alpha_s$, the iteration of the $P_{gg}$ splitting function along the gluon ladder provides a geometric series that is easily summed, yielding

$$\omega\,\mathcal{G}(\omega,\gamma;1)^{\text{coll}} = \sum_{n=0}^{\infty}\left(\frac{\alpha_s}{2\pi}\frac{P_{gg}(\omega)}{\gamma}\right)^n = \left[1 - \frac{\bar{\alpha}_s}{\omega}\frac{1+\omega A_{gg}}{\gamma}\right]^{-1} . \tag{4.55}$$

Since $\omega\mathcal{G} = [1 - \frac{\bar{\alpha}_s}{\omega}X]^{-1}$ [cfr. eq. (4.9b)], we conclude $X_0^{\text{coll}}(\omega,\gamma;1) = [1+\omega A_{gg}]/\gamma$.

The second term in eq. (4.54) stems from the diagrams with a gluon emitted from the quark lines, where an extra $P_{qq}$ splitting function is produced, see fig. 4.7b and its symmetric counterpart (thus a factor of 2 is accounted). As the gluon emitted from the quark lines on the side, it is naturally associated with the impact factors. However, we note that, since $P_{qq}$ vanishes at $\omega = 0$ (cfr. eq. (4.38)), these contributions are suppressed by two powers of $\omega$ w.r.t. the diagram with $P_{gg}$, and thus are next-to-next-to-leading in the BFKL hierarchy. Nevertheless, we keep them just to be accurate in the LO DGLAP evolution.

The third term in eq. (4.54) is the running coupling ($b$-dependent) contribution derived in eq. (4.35), and there is flexibility to attribute it to either the impact factors or the GGF, or even partially both. In the following section, we shall deal with this flexibility more systematically, and propose some possible choices of transverse NLO RGI impact factor.

### 4.4.2 NLO RGI transverse impact factor

In this subsection, We move on to determine the NLO RGI impact factor from the NLO cross section derived in the previous subsection. We start by parametrizing the collinear structure of RGI impact factors and kernel as follows, similar to the LO case but with more parameters

$$\Phi(\omega,\gamma;1) = \Phi_0(\omega,\gamma;1)\left[1+\bar{\alpha}_s\left(\frac{M(\omega)}{\gamma}+\frac{\bar{M}(\omega)}{1+\omega-\gamma}+r_1(\omega,\gamma)\right)+\mathcal{O}(\bar{\alpha}_s^2)\right] \tag{4.56}$$

$$X(\omega,\gamma;1) = \frac{1+\omega U(\omega)}{\gamma}+\mathcal{O}(\gamma^0)+\bar{\alpha}_s\left(\frac{V(\omega)}{\gamma^2}+\mathcal{O}(\gamma^{-1})\right)+\mathcal{O}(\bar{\alpha}_s^2)\ , \tag{4.57}$$

where $r_1$ is regular at $\gamma = 0, 1+\omega$ and we have taken into account that additional powers of $\bar{\alpha}_s$ involve additional powers of $1/\gamma$ and $1/(1+\omega-\gamma)$.[5] We omit the superscript $(T)$ on the impact factors in the subsection for simplicity.

The integrand of the NLO cross section is, with the LO contribution $\Phi_0\,\mathcal{G}_0\,\Phi_0$ excluded,

$$\begin{aligned}\alpha_s\,\tilde{\tilde{\sigma}}_1(\omega,\gamma;1) &= (\Phi_0\,\mathcal{G}_1\,\Phi_0+\Phi_1\,\mathcal{G}_0\,\Phi_0+\Phi_0\,\mathcal{G}_0\,\Phi_1)-\Phi_0\,\mathcal{G}_0\,\Phi_0\\ &= \tilde{\tilde{\sigma}}_0(\omega,\gamma;1)\ \bar{\alpha}_s\left[\frac{\frac{1}{\omega}+M+\bar{M}+U}{\gamma}+\mathcal{O}(\gamma^0)\right]\ .\end{aligned} \tag{4.58}$$

By comparing eq. (4.58) with eq. (4.54), we obtain a relation that works as a constraint on our proposed parameterization,

$$M+\bar{M}+U = A_{gg}+2\bar{P}_{qq}-\bar{b}\ , \tag{4.59}$$

with $\bar{b}$ defined in eq. (1.94), $\bar{P}_{ab}\equiv P_{ab}/(2C_A)$, and $\bar{P}_{gg} = 1/\omega + A_{gg}$ [cfr. eq. (4.41)].

To check the compatibility of our collinear analysis with the known BFKL results, and also to investigate the potential constraints on the RGI impact factors, we show the

[5] Recall that $\Phi_0^{(T)}$ has collinear poles of second order. As a result, we expect an improved NL impact factor with cubic poles. In contrast, the collinear behavior of the BFKL impact factor $\phi_1^{(T)}$ featuring cubic and even quartic poles at $\gamma = 0, 1$, as it is apparent from eq. (4.61).

collinear structure of the NLO BFKL transverse impact factor eqs. (4.24a) and (4.27) and kernel eq. (1.93).[6] At symmetric scales $s_0 = \mu_R^2 = Q_1 Q_2$, i.e., $p = 0$:

$$\phi_0(\gamma) = \phi_0(1-\gamma) = C_0 \left( \frac{1}{\gamma^2} + \frac{D(0)}{\gamma} + \frac{1}{(1-\gamma)^2} + \frac{\bar{D}(0)}{1-\gamma} + \cdots \right) \tag{4.60}$$

$$\phi_1(\gamma) = \phi_0(\gamma) \left( \frac{-1}{\gamma^2} + \frac{\eta}{\gamma} + \frac{-3/2}{(1-\gamma)^2} + \frac{\bar{\eta}}{1-\gamma} + \cdots \right) \tag{4.61}$$

$$\chi(\gamma) = \frac{1}{\gamma} + \bar{\alpha}_s \left( \frac{-1/2}{\gamma^3} + \frac{A_1(0) - \bar{b}/2}{\gamma^2} + \frac{H_1}{\gamma} + \cdots \right) \tag{4.62}$$

$$\eta = -\frac{11}{6} \, , \quad \bar{\eta} = -\frac{7}{4} \, , \quad H_1 = -\frac{T_R N_f}{N_c} \left( \frac{5}{9} + \frac{13}{18 N_c^2} \right) \, , \tag{4.63}$$

where $C_0$, $D(0)$ and $\bar{D}(0)$ were already determined in eq. (4.46) and the full $A_1$ reads

$$A_1(\omega) = -\frac{1}{\omega+1} + \frac{1}{\omega+2} - \frac{1}{\omega+3} - [\psi(2+\omega) - \psi(1)] + \frac{11}{12} - \frac{T_R N_f}{3 N_c^3} \, . \tag{4.64}$$

Thus the consistency condition on the kernel eq. (4.18) yields

$$A_1 - b/2 = U + V \, . \tag{4.65}$$

By noting that $\phi_0(\gamma) = \phi_0(1-\gamma) = \Phi_0(0, \gamma; p)$ for any $p$, eq. (4.20) is simplified,

$$\begin{aligned} \phi_1(\gamma) + \phi_1(1-\gamma) &= \Phi_1(0,\gamma) + \Phi_1(0, 1-\gamma) \\ &\quad + \chi_0(\gamma)[\partial_\omega \Phi_0(0,\gamma) + \partial_\omega \Phi_0(0, 1-\gamma)] + \phi_0(\gamma) \partial_\omega X_0(0,\gamma) \, , \end{aligned} \tag{4.66}$$

where $\Phi$'s and $X$ must be considered here at $p = 0$, i.e., by replacing $\gamma \to \gamma + \omega/2$ in eqs. (4.56) and (4.57). From eq. (4.61) we can expand the l.h.s. of eq. (4.66) around the collinear pole $\gamma = 0$:

$$\phi_1(\gamma) + \phi_1(1-\gamma) = \phi_0(\gamma) \, \bar{\alpha}_s \left[ \frac{-5/2}{\gamma^2} + \frac{\eta + \bar{\eta}}{\gamma} + \mathcal{O}(\gamma^0) \right] \, . \tag{4.67}$$

By expanding the r.h.s. of eq. (4.66) using eqs. (4.56) and (4.57) — with the replacement $\gamma \to \gamma + \omega/2$ —, the coefficient $-5/2$ of the quadratic pole within square brackets in NLO BFKL impact factors eq. (4.67) is correctly reproduced from the RGI approach,

[6] With running-coupling scale $\mu_R^2 = Q_1^2$, the double poles of $\chi_1(\gamma)$ are $A_1/\gamma^2$ and $(A_1 - \bar{b})/(1-\gamma)^2$. With symmetric scale $\mu_R^2 = Q_1 Q_2$, the coefficients of both poles are equal to $A_1 - \bar{b}/2$.

while the coefficients of the simple poles are equal if

$$\eta + \bar{\eta} = B + \bar{B} + \tfrac{1}{2}D + \tfrac{1}{2}\bar{D} + M + \bar{M} + U\Big|_{\omega=0} . \tag{4.68}$$

We can check that this is indeed the case. In fact, by exploiting eq. (4.52) and eq. (4.59), we find the coefficient of the simple pole in the RGI approach is

$$B + \bar{B} + \tfrac{1}{2}D + \tfrac{1}{2}\bar{D} + M + \bar{M} + U\Big|_{\omega=0} = 2\bar{P}_{qq} + 2A_{qg} + A_{gq} + A_{gg} + \tfrac{1}{2}D + \tfrac{1}{2}\bar{D} - \bar{b}\Big|_{\omega=0} \tag{4.69a}$$

$$= -\frac{43}{12} = \eta + \bar{\eta} , \tag{4.69b}$$

thus proving the consistency of next-to-leading BFKL and leading-order DGLAP.

Of course, the constraints (4.65) and (4.69a) derived from eqs. (4.18) and (4.20) respectively, can be fulfilled in different ways. In table 4.2 we present some choices that we prefer on physical grounds.

| scheme name | $U$ | $V$ | $B+\bar{B}$ | $M+\bar{M}$ |
|---|---|---|---|---|
| collA | $A_{gg}-\bar{b}$ | $\Delta A+\bar{b}/2$ | $2A_{qg}+A_{gq}$ | $2\bar{P}_{qq}$ |
| collB | $A_{gg}$ | $\Delta A-\bar{b}/2$ | $2A_{qg}+A_{gq}$ | $2\bar{P}_{qq}-\bar{b}$ |
| zVnB | $A_1-\bar{b}/2$ | 0 | $2A_{qg}+A_{gq}$ | $2\bar{P}_{qq}-\Delta A-\bar{b}/2$ |
| zVnM | $A_1-\bar{b}/2$ | 0 | $2A_{qg}+A_{gq}-\Delta A-\bar{b}/2$ | $2\bar{P}_{qq}$ |
| zVzM | $A_1-\bar{b}/2$ | 0 | $2\bar{P}_{qq}+2A_{qg}+A_{gq}-\Delta A-\bar{b}/2$ | 0 |

**Table 4.2.** Favourite scheme choices for defining the NLO RGI transverse impact factor.

For simplicity of the presentation, we introduced $\Delta A$ in the table, where

$$\Delta A = A_1(\omega) - A_{gg}(\omega) = \frac{C_F}{C_A} 2N_f \bar{P}_{qg}(0) = \left(1 - \frac{1}{N_c^2}\right)\frac{T_R N_f}{3N_c} . \tag{4.70}$$

Remarks on these schemes are as follows,

- Schemes “collA" and “collB" are motivated by the collinear analysis. They suggest the value of $B+\bar{B}$ from eq. (4.52) and the values of $M+\bar{M}$ and $U$ from eqs. (4.55) and (4.59).
- In the Scheme “collA", we assign the running-coupling term $-\bar{b}$ to the kernel, while in the Scheme “collB" to the impact factors.
- In the Schemes “zV…" we set the coefficient $V$ of the double pole of $X_1$ to zero , following the spirit of the RG improvement to transfer the most singular $\gamma$-poles of

NL objects into regular $\omega$-corrections of leading-order terms. In this way, we assign all the dependence of the kernel on the gluon anomalous dimension and running coupling $A_1 - \bar{b}/2$ to the $\mathcal{O}(\omega)$ term of the leading eigenvalue $X_0$.

- The Scheme “zVnB" adopts the natural (i.e., collinearly motivated) choice for the $B$'s coefficients.
- The Scheme “zVnM" adopts the natural choice for the $M$'s coefficients.
- The Scheme “zVzM" sets the coefficients $M$ of the cubic poles of the NLO impact factors to zero, thus assigning all the residual dependence on the anomalous dimensions to the $\mathcal{O}(\omega)$ term of the leading impact factor $\Phi_0$.

In fact, each of the schemes in table 4.2 can be implemented with more flexibility on how $B$, $\bar{B}$, $M$ and $\bar{M}$ are individually specified, and also because the regular part of impact factors is fully constrained only at $\omega = 0$. For the leading impact factor $\Phi_0^{(T)}$, we propose the three sub-schemes of eq. (4.53), where $B = \bar{B}$ in the sub-schemes I and II, while $\bar{B} = B + A_{gq}$ in sub-scheme III, as in eqs. (4.53a) to (4.53c).

As for the LO eigenvalue function, we adopt the expression in [34]:

$$X_0(\omega,\gamma;0) = 2\psi(1) - \psi(\gamma + \frac{\omega}{2}) - \psi(1-\gamma+\frac{\omega}{2}) + \omega U(\omega)\left(\frac{1}{\gamma+\omega/2} + \frac{1}{1-\gamma+\omega/2}\right) , \tag{4.71}$$

where $U(\omega)$ depends on the scheme choice as shown in table 4.2. Then, according to eq. (4.18), the next-to-leading improved eigenvalue at $\omega = 0$ is given by

$$X_1(0,\gamma) = \chi_1(\gamma) + \frac{1}{2}\chi_0(\gamma)\frac{\pi^2}{\sin^2\pi\gamma} - U(0)\left(\frac{1}{\gamma} + \frac{1}{1-\gamma}\right)\chi_0(\gamma) . \tag{4.72}$$

The above expression is free of cubic poles, but still contains simple poles and possibly double poles, depending on the scheme choice:

$$X_1(0,\gamma) = \left(A_1 - \frac{\bar{b}}{2} - U(0)\right)\frac{1}{\gamma^2} + \left(H_1 + \frac{\pi^2}{6} - U(0)\right)\frac{1}{\gamma} + \cdots . \tag{4.73}$$

According to the RGI method, we require the RGI eigenvalue function $X_1(\omega,\gamma)$ to have poles at the expected $\omega$-shifted positions. Thus the complete expression for the RGI eigenvalue function $X_1(\omega,\gamma)$ is given by

$$X_1(\omega,\gamma) = X_1(0,\gamma) + \frac{A_1(\omega) - \frac{\bar{b}}{2} - U(\omega)}{(\gamma+\frac{\omega}{2})^2} - \frac{A_1(0) - \frac{\bar{b}}{2} - U(0)}{\gamma^2} + (\gamma \leftrightarrow 1-\gamma) +$$

$$+\left(H_1+\frac{\pi^2}{6}-U(0)\right)\left[X_0(\omega,\gamma)-\chi_0(\gamma)\right]\ . \tag{4.74}$$

We can now exploit eq. (4.66) to constrain the NLO improved transverse impact factor at $\omega=0$ and arbitrary $\gamma$. If we further require such impact factor to be symmetric in $\gamma\to 1-\gamma$, we obtain[7]

$$\begin{aligned}\Phi_1(0,\gamma)&=\frac{1}{2}\left[\Phi_1(0,\gamma)+\Phi_1(0,1-\gamma)\right]\\&=\frac{1}{2}\Big[\phi_1(\gamma)+\phi_1(1-\gamma)-\phi_0(\gamma)\partial_\omega X_0(0,\gamma)-\chi_0(\gamma)\Big(\partial_\omega\Phi_0(0,\gamma)+\partial_\omega\Phi_0(0,1-\gamma)\Big)\Big]\ .\end{aligned} \tag{4.75}$$

Its Laurent expansion around $\gamma=0$ reads

$$\Phi_1(0,\gamma)=C_0\left[\frac{M(0)}{\gamma^3}+\frac{M_2}{\gamma^2}+\frac{M_1}{\gamma}+\mathcal{O}(\gamma^0)\right]\ , \tag{4.76}$$

where $M_2$ and $M_1$ depend on the scheme choice that defines the $\omega$-dependence of $\Phi_0(\omega,\gamma)$ and $X_0(\omega,\gamma)$ in eqs. (4.53) and (4.71).

We extend $\Phi_1$ at $\omega\neq 0$ by requiring the collinear poles to be located at $\gamma=-\omega/2$ and $\gamma=1+\omega/2$ and with $\omega$-dependent leading coefficients $M(\omega)$ and $\bar{M}(\omega)$ as in eq. (4.56). This can be obtained in various ways, and we adopt the following choice:

$$\begin{aligned}\Phi_1(\omega,\gamma;0)&=\Phi_1(0,\gamma)\\&+C_0\left\{\left[\frac{M(\omega)}{(\gamma+\frac{\omega}{2})^3}+\frac{M_2}{(\gamma+\frac{\omega}{2})^2}+\frac{M_1}{\gamma+\frac{\omega}{2}}\right]-\left[\frac{M(0)}{\gamma^3}+\frac{M_2}{\gamma^2}+\frac{M_1}{\gamma}\right]+\begin{pmatrix}\gamma\leftrightarrow 1-\gamma\\ M\to\bar{M}\end{pmatrix}\right\}\ .\end{aligned} \tag{4.77}$$

Having required $\Phi_1$ to be symmetric causes $M(\omega)=\bar{M}(\omega)$ equal to half the expression in the last column of table 4.2.

[7] We note that, while $\phi_0(\gamma)$ is symmetric in $\gamma\to 1-\gamma$, the NLO impact factor $\phi_1(\gamma)$ is not. Actually, since the latter has been derived [83] a cross section [115] which depends on the product $\phi^{(T)}(\gamma)\phi^{(T)}(1-\gamma)$, it is not clear to us how $\phi_1$ has been unambiguously derived, without imposing further requirements.

## 4.5 Resummation of the LO and NLO longitudinal impact factor

### 4.5.1 Cross section and impact factor at leading order

In this section, we proceed to derive the RGI longitudinal impact factors. Firstly, in order to determine the LO longitudinal RGI impact factor, we first consider the cross section $\sigma^{(LT)}(Q_1, Q_2)$ where the photon $Q_1$ (on the left) has longitudinal polarization, while the other one $Q_2$ (on the right) is transverse.

We are interested in the collinear limit $Q_1^2 \gg Q_2^2$, therefore we need the vertices that describe how the longitudinal photon $Q_1$ couples to quarks and gluons $k$ where the collinear strong ordering also specifies $Q_1^2 \gg k^2$. The form of the coupling can be derived from the longitudinal coefficient functions, as explained in appendix B.

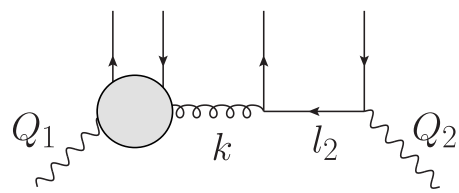


**Figure 4.8.** Diagramatics of collinear limit at leading order for the longitudinal impact factor. The blob represents the gluonic contribution to the longitudinal coefficient function at the lowest order in $\alpha_\mathrm{s}$.

The lowest order ladder diagram of our interest involving a high-energy gluon exchange is depicted in fig. 4.8. The shaded circle at the left represents the gluon contribution to the longitudinal coefficient function $C_L^g$, while the two vertices on the right side represent two splitting functions, as in the $TT$-case.

We can then repeat the collinear analysis of sec. 4.3.1 by replacing in eq. (4.36) the "transverse" factor eq. (B.6) with the "longitudinal" factor eq. (B.8) (see Appendix), thus obtaining the leading $\gamma$-pole structure of $\tilde{\tilde{\sigma}}^{(LT)}$:

$$\begin{aligned}\tilde{\tilde{\sigma}}_0^{(LT)}(\omega,\gamma;1)_{\mathrm{coll}} = {} & \frac{\alpha\alpha_\mathrm{s}\Big(\sum_q e_q^2\Big)8T_R\sqrt{2(N_c^2-1)}}{\gamma\,(2+\omega)(3+\omega)}\;\frac{1+\omega A_{gq}(\omega)}{\omega} \\ & \frac{\alpha\alpha_\mathrm{s}\Big(\sum_q e_q^2\Big)2P_{qg}(\omega)\sqrt{2(N_c^2-1)}}{\gamma^2} + \mathcal{O}\left(\gamma^{-2}\right) \\ = {} & \Phi_{\mathrm{BNP}}^{(L)}(\omega,\gamma)\;\frac{1+\omega A_{gq}(\omega)}{\omega}\;\Phi_{\mathrm{BNP}}^{(T)}(\omega,1+\omega-\gamma) + \mathcal{O}\left(\gamma^{-2}\right)\ ,\end{aligned} \tag{4.78}$$

namely the product of the corresponding BNP impact factors with exact kinematics [82], the LO GGF $1/\omega$ and the same $\mathcal{O}(\omega)$ correction $\propto A_{gq}(\omega)$. The second line of eq. (4.78) follows from the collinear structure of the BNP impact factors, reported in eq. (4.45) for the transverse polarization and in the following equation for the longitudinal polarization:

$$\begin{aligned}
\Phi^{(L)}_{\mathrm{BNP}}(\omega,\gamma) &= \alpha\alpha_{\mathrm{s}}\Big(\sum_q e_q^2\Big)T_R\sqrt{2(N_c^2-1)}\;4\frac{\pi\Gamma(\gamma+\delta+1)\Gamma(\gamma+1)}{\Gamma(\omega)}\frac{1}{(\delta^2-1)\,(\delta^2-4)} \\
&\quad\cdot\left[\frac{\psi(\gamma+\delta)-\psi(\gamma)}{\delta}\cdot\frac{3\omega^2-(\delta^2-1)}{2\omega}-3\right] \qquad (4.79)\\
&= C_0\left[\frac{1+\omega\Lambda(\omega)}{\gamma}+D_L(\omega)+\mathcal{O}(\gamma)\;+\;(\gamma\leftrightarrow 1+\omega-\gamma)\right] \qquad (4.80)
\end{aligned}$$

$$1+\omega\Lambda(\omega)=\frac{6}{(2+\omega)(3+\omega)}\;,\quad \Lambda(0)=-\frac{5}{6}\;,\quad D_L(0)=-\frac{1}{3}\;,\quad \delta\equiv 1+\omega-2\gamma\;, \tag{4.81}$$

where $C_0$ is the same normalization coefficient of the transverse impact factor in eq. (4.46). Similar to the $TT$-case, eq. (4.78) can be expanded at the pole of $\gamma=0$, where the energy scale is again asymmetric

$$\tilde{\tilde{\sigma}}^{(LT)}_0(\omega,\gamma;1)=C_0^2\frac{1}{\omega}\left[\frac{(1+\omega\Lambda)(1+\omega A_{gq})(1+\omega A_{qg})}{\gamma^3}+\mathcal{O}(\gamma^{-2})\right]\;. \tag{4.82}$$

Taking inspiration from the parametrization procedure as eqs. (4.50) and (4.80), we parametrize the collinear structure of the longitudinal LO RGI impact factor as

$$\Phi^{(L)}_0(\omega,\gamma;1)=C_0\left[\frac{1+\omega B_L(\omega)}{\gamma}+D_L(\omega)+\frac{1+\omega\bar{B}_L(\omega)}{1+\omega-\gamma}+\bar{D}_L(\omega)\right]+r_L(\omega,\gamma)\;, \tag{4.83}$$

where $r_L(\omega,\gamma)$ vanishes at $\gamma=0$ and $\gamma=1+\omega$. By combining the above expression with the analogue one in eq. (4.50), we obtain

$$\begin{aligned}
\tilde{\tilde{\sigma}}^{(LT)}_0(\omega,\gamma;1) &= \Phi^{(L)}_0(\omega,\gamma;1)\,\frac{1}{\omega}\,\Phi^{(T)}_0(\omega,1+\omega-\gamma;1)\\
&= C_0^2\frac{1}{\omega}\left[\frac{(1+\omega B_L)(1+\omega\bar{B})}{\gamma^3}+\mathcal{O}(\gamma^{-2})\right]+(\gamma\to 1+\omega-\gamma)\;. \qquad (4.84)
\end{aligned}$$

If we compare eq. (4.84) with eq. (4.82), we obtain a relation among $B_L$, $\bar{B}$ and the known quantities $\Lambda, A_{qg}, A_{gq}$. However, remembering that $B$ and $\bar{B}$ are constrained by eq. (4.52), we can actually relate $B_L$ and $B$:

$$\frac{1+\omega B_L}{1+\omega B} = \frac{1+\omega\Lambda}{1+\omega A_{qg}} \tag{4.85}$$

$$\Longrightarrow \quad B_L = \Lambda + B - A_{qg} + \mathcal{O}(\omega) \; . \tag{4.86}$$

The coefficient $\bar{B}_L$ of the simple anti-collinear pole $\gamma = 1+\omega$ can be determined analogously by considering the cross section for two longitudinal photons, i.e., by comparing the two expansions for

$$\begin{aligned}\tilde{\tilde{\sigma}}_0^{(LL)}(\omega,\gamma;1) &= \Phi_0^{(L)}(\omega,\gamma;1)\,\frac{1}{\omega}\,\Phi_0^{(L)}(\omega,1+\omega-\gamma;1)\\ &= \Phi_{\mathrm{BNP}}^{(L)}(\omega,\gamma)\,\frac{1+\omega A_{gq}(\omega)}{\omega}\,\Phi_{\mathrm{BNP}}^{(L)}(\omega,1+\omega-\gamma) + \mathcal{O}\left(\gamma^{-1}\right)\;, \end{aligned} \tag{4.87}$$

yielding

$$(1+\omega B_L)(1+\omega\bar{B}_L) = (1+\omega\Lambda)^2(1+\omega A_{gq}) \tag{4.88a}$$

$$\Longrightarrow \quad B_L + \bar{B}_L = 2\Lambda + A_{gq} + \mathcal{O}(\omega) \; . \tag{4.88b}$$

Note that the role played by $A_{qg}$ for $B$ and $\bar{B}$ in the transverse case eq. (4.52) is now played by $\Lambda$ for $B_L$ and $\bar{B}_L$ in longitudinal case eq. (4.88).

Again, similar to our proposed schemes in the transverse case, we can define the LO RGI longitudinal impact factor by sharing the $A_{gq}$ correction term between the leading collinear and anti-collinear poles:

$$\Phi_0^{(L)}(\omega,\gamma;1) = \Phi_{\mathrm{BNP}}^{(L)}(\omega,\gamma)\left[1+\frac{\omega}{2}A_{gq}(\omega)\right] \qquad \text{(scheme I)} \tag{4.89a}$$

$$\Phi_0^{(L)}(\omega,\gamma;1) = \Phi_{\mathrm{BNP}}^{(L)}(\omega,\gamma) + C_0\frac{\omega}{2}A_{gq}(\omega)\left[\frac{1}{\gamma}+\frac{1}{1+\omega-\gamma}\right] \qquad \text{(scheme II)} \tag{4.89b}$$

$$\Phi_0^{(L)}(\omega,\gamma;1) = \Phi_{\mathrm{BNP}}^{(L)}(\omega,\gamma) + C_0\,\omega A_{gq}(\omega)\frac{1+\omega A_{qg}}{1+\omega-\gamma} \qquad \text{(scheme III)}\;. \tag{4.89c}$$

Schemes I and II implement the choice $B_L = \bar{B}_L = \Lambda + A_{gq}/2$, giving rise to symmetric impact factors, while scheme III has $B_L = \Lambda$ and $\bar{B}_L = \Lambda + A_{gq} + \omega\Lambda A_{gq}$, giving rise to an asymmetric impact factor, but fulfilling exactly eq. (4.88a).

## 4.5.2 Cross section and impact factor at next-to-leading order

In this subsection, we complete our analytical work by finishing the construction of the RGI longitudinal impact factors at the next-to-leading order. The collinear analysis at NLO for the longitudinal-transverse photon cross section involves the three diagrams depicted in fig. 4.9 and can be presented in the following form:

$$\alpha_s\,\tilde{\tilde{\sigma}}_1^{(LT)}(\omega,\gamma;1) = \tilde{\tilde{\sigma}}_0^{(LT)}(\omega,\gamma;1)\left[\frac{\alpha_s}{2\pi}\frac{P_{gg}}{\gamma} + \frac{\alpha_s}{2\pi}\frac{P_{qg}}{\gamma} + \frac{C_F}{T_R}\frac{3+\omega}{2}\cdot\frac{\alpha_s}{2\pi}\frac{P_{qg}}{\gamma} - \frac{\alpha_s b}{\gamma} + \mathcal{O}(\gamma^0)\right], \tag{4.90}$$

where $\tilde{\tilde{\sigma}}_0^{(LT)}$ is the LO integrand defined in eq. (4.82).

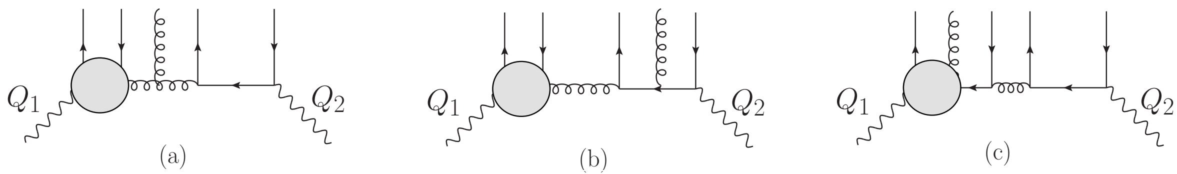


**Figure 4.9.** Diagramatics of collinear limit at next-to-leading order for the longitudinal impact factor. (a) Photon-gluon coefficient function and gluon emission from gluon line; (b) Photon-gluon coefficient function and gluon emission from quark line. (c) Photon-quark coefficient function and quark emission from parent gluon;

We shall comment the contributions in the eq. (4.90) as follows:

- The first term in the r.h.s. of eq. (4.90) stems from the diagram of fig. 4.9(a) involving a $P_{gg}$ splitting function, and can be entirely associated with the GGF.
- The second term stems from the diagram of fig. 4.9(b), with a gluon emitted from the quark line on the right, and it is naturally associated to the impact factor of the transverse photon $Q_2$.
- The third term stems from the diagram of fig. 4.9(c), which is genuinely different from other diagrams, because it involves a coefficient function where the longitudinal photon $Q_1$ couples to a quark. As explained in appendix B.0.2, the photon-quark coefficient function differs from the photon-gluon one by the multiplicative factor $C_F(3+\omega)/(2T_R)$ [cfr. eq. (B.13)]; just to the right of the blob, we find the vertex with the $P_{qg}$ splitting function. This contribution is naturally associated with the impact factor of the longitudinal photon $Q_1$.
- The fourth and last term in eq. (4.90) is the running coupling ($b$-dependent) contribution derived in eq. (4.35), and can be incorporated into either the impact

factors or the GGF, or partially both.

In order to determine the NLO RGI longitudinal impact factor from the NLO cross section, we parametrize the collinear structure of the longitudinal impact factor exactly as in eq. (4.56), by appending the subscript $L$ to the various (unbarred) coefficients, e.g., $M \to M_L$. A straightforward calculation yields

$$\alpha_s\, \tilde{\tilde{\sigma}}_1^{(LT)}(\omega,\gamma;1) = \tilde{\tilde{\sigma}}_0^{(LT)}(\omega,\gamma;1)\; \bar{\alpha}_s \left[\frac{\frac{1}{\omega}+M_L+\bar{M}+U}{\gamma} + \mathcal{O}(\gamma^0)\right] . \tag{4.91}$$

which is nothing but the result of eq. (4.58) with $T \to L$ in the first impact factor. We then derive [cfr. eq. (4.59) and the subsequent definitions]

$$M_L + \bar{M} + U = \mathcal{P}_L + \bar{P}_{qq} + A_{gg} - \bar{b}\,, \qquad \mathcal{P}_L(\omega) \equiv \frac{C_F}{T_R}\bar{P}_{qg}\frac{3+\omega}{2} \tag{4.92}$$

$$\Longrightarrow \quad M_L - M = \mathcal{P}_L - \bar{P}_{qq} = \frac{C_F}{2C_A} + \mathcal{O}(\omega)\,. \tag{4.93}$$

To check the compatibility of the collinear analysis with the known BFKL results, We start from the collinear structure of the NLO BFKL longitudinal impact factors [eqs. (4.24b) and (4.28)]:

$$\phi_0^{(L)}(\gamma) = \phi_0^{(L)}(1-\gamma) = C_0\left(\frac{1}{\gamma} + D_L(0) + \mathcal{O}(\gamma)\right) \tag{4.94}$$

$$\phi_1^{(L)}(\gamma) = \phi_0^{(L)}(\gamma)\left(\frac{-1/2}{\gamma^2} + \frac{\eta_L}{\gamma} + \frac{-1}{(1-\gamma)^2} + \frac{\bar{\eta}_L}{1-\gamma} + \cdots\right)\,, \quad \eta_L = -\frac{7}{3}\,, \quad \bar{\eta}_L = -\frac{9}{4}\,. \tag{4.95}$$

The next step, as what we did in the $TT$-case, is to expand eq. (4.20) around $\gamma = 0$ by using eqs. (4.60) to (4.63), (4.94) and (4.95) for the l.h.s. and eqs. (4.56) and (4.57) for the r.h.s.. As a result, the leading $\gamma$ poles tends to match exactly, while the subleading ones are equal if

$$\eta_L + \bar{\eta} = B_L + \bar{B} + \tfrac{1}{2}(D_L + \bar{D}) + M_L + \bar{M} + U\Big|_{\omega=0}\,. \tag{4.96}$$

Subtracting 4.69a from the above equation, we obtain a relation among collinear coefficients:

$$\eta_L - \eta = B_L - B + \tfrac{1}{2}(D_L - D) + M_L - M\,. \tag{4.97}$$

While the l.h.s. of the above relation evaluates to $-1/2$, the r.h.s. is equal to $-1/2+$

$C_F/(2C_A)$. Therefore, we find agreement with the result of ref. [83], were it not for the presence of a term proportional to $C_F$ Casimir in the collinear pole. It looks like their impact factor misses the contribution from the diagram of fig. 4.9c.

Finally, by considering the cross section for two longitudinally polarized photons, we obtain the result of eq. (4.96) with the barred (transverse) coefficients replaced by their corresponding longitudinal counterparts:

$$\eta_L + \bar{\eta}_L = B_L + \bar{B}_L + \tfrac{1}{2}(D_L + \bar{D}_L) + M_L + \bar{M}_L + U\Big|_{\omega=0} \,, \tag{4.98}$$

which is satisfied only if $M_L + \bar{M}_L = \mathcal{O}(\omega)$. If we take $\bar{M}_L = M_L$, as it is natural to assume in the transverse case, then we disagree with the result of ref. [83] by a $C_F$ term in the $1/\gamma$ pole of the ratio $\phi_1^{(L)}/\phi_0^{(L)}$.

We collect our results for the longitudinal RGI impact factor in table 4.3.

| scheme name | $U$ | $V$ | $B_L + \bar{B}_L$ | $M_L + \bar{M}_L$ |
|---|---|---|---|---|
| collA | $A_{gg} - \bar{b}$ | $\Delta A + \bar{b}/2$ | $2\Lambda + A_{gq}$ | $2\mathcal{P}_L$ |
| collB | $A_{gg}$ | $\Delta A - \bar{b}/2$ | $2\Lambda + A_{gq}$ | $2\mathcal{P}_L - \bar{b}$ |
| zVnB | $A_1 - \bar{b}/2$ | $0$ | $2\Lambda + A_{gq}$ | $2\mathcal{P}_L - \Delta A - \bar{b}/2$ |
| zVnM | $A_1 - \bar{b}/2$ | $0$ | $2\Lambda + A_{gq} - \Delta A - \bar{b}/2$ | $2\mathcal{P}_L$ |
| zVzM | $A_1 - \bar{b}/2$ | $0$ | $2\mathcal{P}_L + 2\Lambda + A_{gq} - \Delta A - \bar{b}/2$ | $0$ |

**Table 4.3.** Favourite scheme choices for defining the NLO RGI longitudinal impact factor. The values of $U$ and $V$ are the same as in table 4.2.

Once a scheme has been chosen, the LO impact factor $\Phi_0^{(L)}$ can be specified according to one of the sub-schemes in eq. (4.89), with $B_L = \bar{B}_L$ in sub-schemes I and II, while $\bar{B}_L = B_L + A_{gq}$ in sub-scheme III.

The NLO impact factor $\Phi_1^{(L)}$ is constructed to be symmetric, as in the transverse case: at $\omega = 0$ eq. (4.75) holds unaltered, provided we add to $\phi_1$ the contribution

$$\Delta\phi_1^{(L)}(\gamma) = \mathcal{P}_L(0)\left(\frac{1}{\gamma} + \frac{1}{1-\gamma}\right)\phi_0^{(L)}(\gamma) \,. \tag{4.99}$$

The Laurent expansion around $\gamma = 0$ shows a double pole

$$\Phi_1^{(L)}(0,\gamma) = C_0\left[\frac{M_L(0)}{\gamma^2} + \frac{M_{L,1}}{\gamma} + \mathcal{O}(\gamma^0)\right] \,, \tag{4.100}$$

where $M_{L,1}$ depends on the scheme choice. We extend $\Phi_1$ at $\omega \neq 0$ by requiring the collinear poles to be located at $\gamma = -\omega/2$ and $\gamma = 1 + \omega/2$ and with $\omega$-dependent leading coefficients $M_L(\omega)$ and $\bar{M}_L(\omega)$ as we did for the transverse impact factor:

$$\Phi_1^{(L)}(\omega,\gamma;0) = \Phi_1^{(L)}(0,\gamma) \\ + C_0 \left\{ \left[ \frac{M_L(\omega)}{(\gamma+\frac{\omega}{2})^2} + \frac{M_{L,1}}{\gamma+\frac{\omega}{2}} \right] - \left[ \frac{M_L(0)}{\gamma^2} + \frac{M_{L,1}}{\gamma} \right] + \begin{pmatrix} \gamma \leftrightarrow 1-\gamma \\ M \to \bar{M} \end{pmatrix} \right\} . \tag{4.101}$$

Having required $\Phi_1^{(L)}$ to be symmetric causes $M_L(\omega) = \bar{M}_L(\omega)$ equal to half the expression in the last column of table 4.3.

## 4.6 Numerical results

In this section, we apply the factorization formula with renormalization-group improved impact factors and Green's function to compute the $\gamma^*\gamma^*$ cross section in phenomenologically relevant situations. The presented results contain the sum over all combinations of photon polarizations:

$$\sigma = \sigma^{(TT)} + \sigma^{(LT)} + \sigma^{(TL)} + \sigma^{(LL)}. \tag{4.102}$$

For the NLL RGI calculation, the $\sigma^{(TT)}$ is about 56% of the total cross section on average at $Q^2 = 17\,\mathrm{GeV}^2$, while both $\sigma^{(TL)}$ and $\sigma^{(LT)}$ about 19%, $\sigma^{(LL)}$ about 6%. These percentages vary by about 2% for $\sigma^{(TT)}$, and about 1% for other polarization combinations upon changes of the scheme and varying rapidity $Y \in [2, 7]$.

The numerical calculation is based on the following formulae:

- the cross section is calculated using eq. (4.14);
- the leading eigenvalue $X_0$ is given in eq. (4.71);
- the NL eigenvalue $X_1$ in eqs. (4.72) and (4.74) with $\chi_1$ in eq. (1.93); $\omega_{\mathrm{eff}}$ in eq. (4.12);
- the leading impact factors in eqs. (4.53) and (4.89);
- the NL impact factors in eq. (4.75) at $\omega = 0$ and eqs. (4.77) and (4.101) at $\omega \neq 0$.

We shall compare our results with the experimental measurements of L3 [46] at $Q^2 = 16$ GeV$^2$ and of OPAL [47] at $Q^2 = 17.9$ GeV$^2$, and also with previous calculations of the same cross section. Since the values of $Q^2$ in L3 and OPAL are close while their error bars are relatively large, it is reasonable to compare the data from both experiments with theoretical predictions at $Q^2 = 17$ GeV$^2$.

In addition, We adopt the strong coupling value to be $\alpha_s\left(Q^2 = 17\ \text{GeV}^2\right) \approx 0.229$ as derived from the Particle Data Group [52].

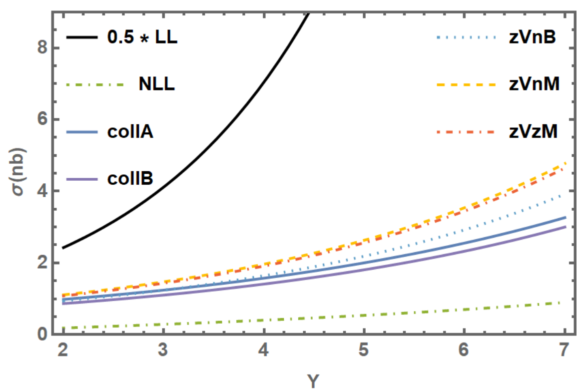


**Figure 4.10.** The value of the $\gamma^*\gamma^*$ cross section contribution from the BFKL exchange for $Q^2 = 17\ \text{GeV}^2$ as a function of rapidity $Y$. All five schemes (see tables 4.2 and 4.3) for the NLL RGI calculation are shown together with the pure LL calculation (black solid and rescaled with a factor 0.5) and pure NLL calculation (green dot-dashed).

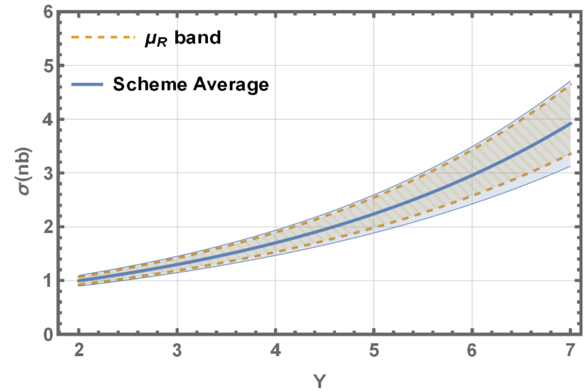


**Figure 4.11.** The value of the $\gamma^*\gamma^*$ cross section contribution from the BFKL exchange for $Q^2 = 17\ \text{GeV}^2$ as a function of rapidity $Y$. The scheme average band (blue-solid) represents the average value and standard deviation of the five resummed schemes. The $\mu_R$ band (yellow-dashed) is computed from average values of the five resummed schemes with half or double $\mu_R^2$ respectively.

In fig. 4.10 we show the results for the NLL RGI cross sections using scheme I for the LO impact factors eqs. (4.53) and (4.89) and the five different schemes from tables 4.2 and 4.3 at NLO, and compare them with the pure LL and NLL cross sections.

All five NLL RGI cross sections are significantly reduced with respect to the LL calculation, meanwhile, they are also significantly above the pure NLL calculation. We observe that, the different schemes give very similar results. In order to present the results more intuitively, we incorporate a band to represent the scheme ambiguity as in fig. 4.11. The band size is defined as the standard deviation calculated from the five schemes at each rapidity $Y$. In the following, if the improved NLL cross section is presented as a single curve, then the curve is just the average for the five NLL RGI schemes. Furthermore, we note that adopting schemes II and III for the LO impact factors does not change significantly our estimates in our tests.

In fig. 4.11, we also test the stability of the improved NLL cross section calculation with respect to the variation of the $\mu_R$ scale, the argument of the running coupling. The upper and lower $\mu_R$ band is computed from average values of the five resummed schemes with half or double $\mu_R^2$ respectively. It turns out that the $\mu_R$ band size is slightly smaller than the scheme ambiguity band size. It is worth noting that besides the dependence on $\mu_R$ of the NLO impact factor and the running coupling argument, the NLO BFKL eigenfunction would also rely on $\mu_R$ when $\mu_R^2 \neq Q_1 Q_2$,

$$\tilde{X}_1(\omega, \gamma) = X_1(\omega, \gamma) + \bar{b}\, X_0(\omega, \gamma) \ln \frac{\mu_R^2}{Q_1 Q_2}. \tag{4.103}$$

and the resummed effective $\omega$ after the NLO subtraction with $\mu_R$ dependency is then the solution of

$$\omega = \bar{\alpha}_s(\mu_R^2) X_0(\omega, \gamma) + \bar{\alpha}_s^2(\mu_R^2) \left[ X_1(\omega, \gamma) + \bar{b}\, X_0(\omega, \gamma) \ln \frac{\mu_R^2}{Q_1 Q_2} \right]. \tag{4.104}$$

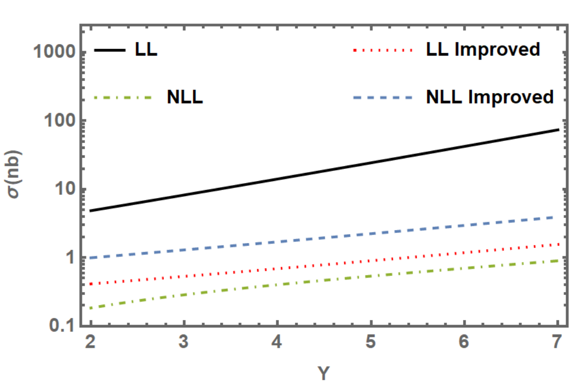


**Figure 4.12.** The value of the $\gamma^*\gamma^*$ cross section contribution from the BFKL exchange for $Q^2 = 17$ GeV$^2$ as a function of rapidity in the logarithmic vertical scale. Pure LL is shown in black-solid, NLL in green dashed-dotted, LL improved in red-dotted and NLL improved in blue-dashed. The NLL improved curve is the average of our five resummed NLL schemes (see text).

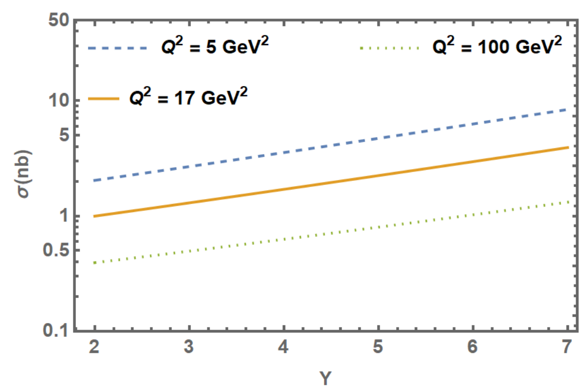


**Figure 4.13.** The value of the $\gamma^*\gamma^*$ cross section contribution from the BFKL exchange from NLL RGI calculation for $Q^2 = 5$ (blue-dashed), 17 (yellow-solid), 100 GeV$^2$ (green-dotted) as a function of rapidity $Y$ in logarithmic vertical scale.

In fig. 4.12, we compare the pure LL and NLL results (the latter computed using expressions from refs. [110, 111]), with the improved LL and NLL cross sections. Note the logarithmic vertical scale, which makes the characteristic exponential dependence of the cross section on the rapidity clearly visible. The NLL improved curve is given as the average of different schemes as explained above.

The improved LL and NLL calculations both tame the quick growth of the pure LL cross section with rapidity. It is worth noting that the improvement at LL alone — consisting in the $\omega$ shifted LO eigenfunction and LO impact factors — brings the curve down significantly. We also observe that, the improved NLL is higher than the improved LL calculation, mostly because the improved NLO corrections bring a positive $O(\alpha_s^2)$ term to the impact factors. Finally, we observe that improved calculations (both at LL and NLL) are above the pure NLL cross section.

In fig. 4.13, we compare NLL RGI cross sections for $Q^2 = 5,\ 17,\ 100$ GeV$^2$. The cross section is strongly dependent on $Q^2$. The tendency of the linear growth in the logarithm scale is unchanged upon different values of $Q^2$. The growth with rapidity is slowed down with increasing $Q^2$ due to the smaller value of the coupling constant, which affects the value of the leading exponent in the gluon Greens's function.

As introduced in the section 4.1, to compare with the experimental data, our resumed cross section shall be accompanied by the fixed order contributions from the quark box diagrams. This quark box contribution is dominant at low rapidities and decreases with the increase of the rapidity, while the BFKL cross section is only dominant at high rapidities. The total $\gamma^*\gamma^*$ cross section presented in the following includes both the quark box and the BFKL contributions.

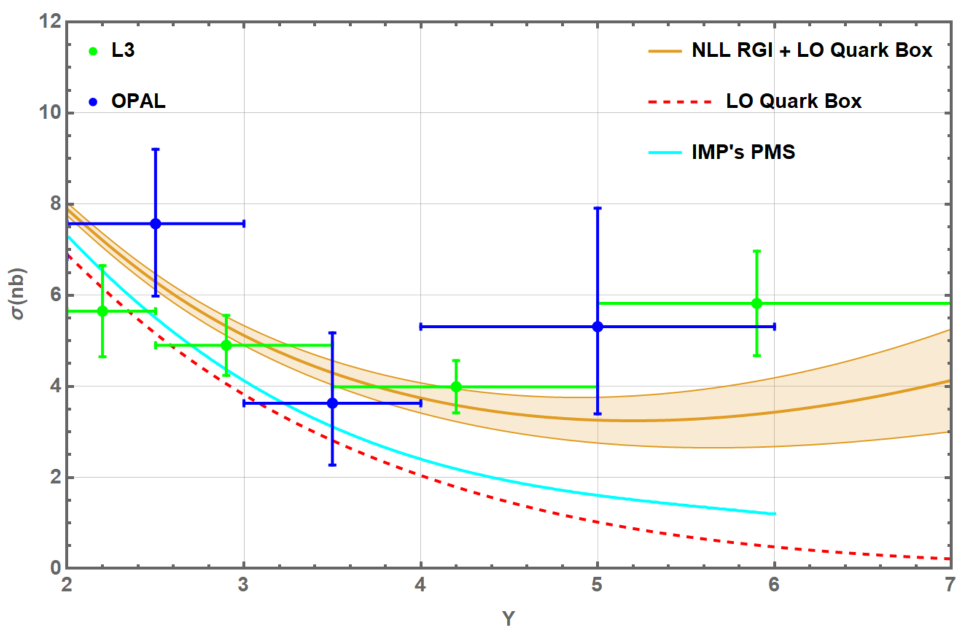


**Figure 4.14.** Cross sections for $Q^2 = 17$ GeV$^2$, compared with L3 ($Q^2 = 16$ GeV$^2$) [46] and OPAL ($Q^2 = 17.9$ GeV$^2$) [47] data. The NLL improved curve is the sum of our averaged NLL BFKL resummed scheme and LO quark box contribution. The band size represents a combination of the scheme uncertainty and the $\mu_R$ band, i.e. $\delta_{\text{total}} = \sqrt{\delta^2_{\text{scheme}} + \delta^2_{\mu_R}}$. The calculation is done for $N_f = 4$ massless flavors. The Ivanov-Murdaca-Papa's (IMP's) PMS optimized curve (solid-cyan) is from [83]. Separately shown is the quark box contribution (dashed red).

In fig. 4.14 we compare the results from NLL improved calculation with the experimental measurements of L3 [46] at $Q^2 = 16$ GeV$^2$ and of OPAL [47] at $Q^2 = 17.9$ GeV$^2$, and also with previous calculations of the same cross section from [83]. As mentioned before, since the values of $Q^2$ in L3 and OPAL are very close, and the errors on the data points are such that $Q^2$ dependence is not visible, it is reasonable to compare the data from both experiments with theoretical predictions at $Q^2 = 17$ GeV$^2$. We also show the LO quark box contribution in this figure. We observe from fig. 4.14 that the RGI NLL improved calculation has a stronger increase over rapidities than the pure NLL one. We also see that our result is significantly higher than the calculation from [83], particularly at high rapidities. The RGI calculation is consistent with the experimental data from LEP within the theoretical and experimental uncertainties.

# Chapter 5 Conclusions

We shall summarize the basic ideas of this work in this chapter and point out the outlook to address some potential topics worth future investigation.

We are interested in the resummation in the BFKL framework. In particular, we introduced the effects of the kinematic constraints and the renormalization group improvements formed in the CCSS resummation and later extended to the photon impact factors.

The kinematical constraints stem from the fact that the gluon momentum in the BFKL gluon ladder is dominant by its transverse component. It takes various forms due to different levels of approximations and applies to the real gluon emission. While the the LL BFKL yields a growth of the unintegrated gluon density that is too steep for the experimental data, we show a tamed growth with kinematic constraints by numerical calculations.

Later on, we start introducing the renormalization group improvements from the observation of the dependency of the energy scale $s_0$ in the high energy factorization cross section. By requiring the scale invariance of the cross section, we are motivated to bring the $\omega$-dependency to the BFKL eigenfunction, where $\omega$ is conjugate to the center of mass energy squared $s$ (or equivalently $1/x$) in the Mellin transform. While the scale effect is well integrated into our resummed BFKL equation, we also give the explicit expressions for the scale transformation up to NNLL.

It is quick to show that the collinear (and anti-collinear) poles are the main construct of the LL BFKL eigenfunction. A collinear analysis shows that the collinear singularities of the BFKL kernel are determined by the non-singular part of the gluon anomalous dimension, while the singular part has already been counted in the LL BFKL. Such renormalization group constrained kernel allows us to resum the $\omega$ dependency to all orders and it prompts us to study the expansion on $\omega$. What's more, we can use the

$\omega$ expansion to construct the resummed NLL kernel and predict the behaviors in even higher orders. While the NNLL BFKL eigenfunction is not currently available, we tested our approach in the $N = 4$ sYM and successfully reproduced the behavior of leading and subleading poles in the Mellin space, followed by a discussion on its mathematical structure to all orders.

The CCSS resummation takes various factors into considerations, i.e., the scale effect, the LO DGLAP from the collinear analysis, the kinematical constraint, and the running coupling, incorporated with the exact NLL BFKL eigenfunction. We compute the unintegrated gluon density and perform the fit the structure function $F_2$ and its charm component $F_2^c$ to the HERA data. We achieved great fits to the $F_2$ with or without $F_2^c$ and demonstrated the stability of our approach as their fitting parameters tend to be almost the same.

We later extend the renormalization group improvements to the impact factors by investigating the virtual photon-photon scattering cross section. We construct the consistency condition between our resummed cross section and the BFKL one, then derive resummed LO and NLO impact factors by the collinear analysis. At LO, our resumed impact factors, whether in longitudinal or transverse polarization, are consistent with the impact factors with exact kinematics computed in [82]. At NLO, the collinear analysis provides an additional term proportional to the Casimir $C_F$ in the longitudinal impact factor that is absent in the NLL BFKL. Note that our resummation has flexibility on the scheme choices. This is because: firstly, there is no input from the long distance contribution in this very framework; secondly, while the collinear analysis provides corrections and constraints to the collinear poles in the Mellin space, the subleading terms remain unspecified as they arise from the the case of comparable virtualities of the exchanged partons. Therefore, We present several resummation schemes motivated by different priorities in the factorization and treat them as an uncertainty when compared with the cross section from HEP. We achieved a consistent description to the experimental data as previous calculations in the literature are shown to be too small.

For the analysis of the resummation on the impact factors, we treat all quarks, including charm quark, massless. Whereas if one can extract the massive impact factors, a resummation can be performed accordingly. However, the extraction of the massive NLO impact factors is rather challenging and left for future studies.

In addition, at an even smaller $x$ regime, the dominant dynamics come from the gluon saturation where the gluons start to recombine and thus form non-linear evolution. One notable approach is the Balitsky-Kovchegov (BK) equation. We are interested in resuming some higher order corrections to the BK equation and forming a numerical solution.

# Appendix A
# Numerical solution to the CCSS resummation

In this appendix, we provide more details of the numerical approach to the CCSS resummed unintegrated gluon density. The general procedures are introduced in [34] and we will focus on the calculation of some boundary terms arising from the DGLAP splitting function.

On recapping the procedures in CCSS resummation [34], one needs to solve for the Green's function $\mathcal{G}\left(Y;k,k_0\right)$

$$\mathcal{G}\left(Y;k,k_0\right)=\mathcal{G}^{(0)}\left(Y;k,k_0\right)\Theta(Y)+\int_0^Y \mathrm{d}y\int_{k_{min}}^{k_{max}}\mathrm{d}k'^2\mathcal{K}\left(Y-y;k,k_0\right)\mathcal{G}\left(Y;k',k_0\right), \tag{A.1}$$

with the initial condition

$$2\pi k_0^2\mathcal{G}^{(0)}\left(Y;k,k_0\right)=\delta\left(\log\frac{k}{k_0}\right). \tag{A.2}$$

A gird in rapidity $Y$ and logarithm of momentum $k$ is introduced in order to form a numerical solution

$$\mathcal{G}\left(Y;k,k_0\right)=\sum_i\sum_j T_i(Y)T_j(k)G\left(Y_i;k_j,k_0\right). \tag{A.3}$$

We note the spacing on the rapidity grid $Y$ as $\Delta y$ with gird sites $y_n=n\Delta y$. The test function $T_i(y)$ is a triangular function defined on the vicinity $(y_{i-1},y_{i+1})$ of $y_i$,

$$T_i(y) = \begin{cases} \dfrac{1}{\Delta y}\left(y - y_{i-1}\right), & y \in \left(y_{i-1}, y_i\right) \\ \dfrac{1}{\Delta y}\left(y_{i+1} - y\right), & y \in \left(y, y_{i+1}\right). \end{cases} \tag{A.4}$$

The kernel $\mathcal{K}$ can be factorized as

$$\begin{aligned} \mathcal{K}\left(Y-y;k,k_0\right) &= \sum_\alpha \mathcal{K}_\alpha\left(Y-y;k,k_0\right) \\ &= \sum_\alpha K_\alpha(k,k')P_\alpha(Y-y)\cdot\Theta\left[Y-y-\max\left(\log\frac{k}{k'},\log\frac{k'}{k}\right)\right] \end{aligned} \tag{A.5}$$

where $\alpha$ stands for different contributions to CCSS resummation, i.e., LL and NLL BFKL, DGLAP etc. The function $P$ is the splitting function contribution with some subtraction terms and $\Theta$ function ensures a kinematic constraint to the kernel.

Discretized in the grid, the contribution from the function $P$ can be cast into the BFKL integral equation,

$$\begin{aligned} \int_x^1 \frac{\mathrm{d}z}{z}P(z)\mathcal{G}(\frac{x}{z}) &= \int_x^1 \frac{\mathrm{d}z'}{z'}P(\frac{x}{z'})\mathcal{G}(z') \\ &= \int_0^{y_i} \mathrm{d}y' P(y_i,y')\sum_k T_k(y')\mathcal{G}(y_k). \end{aligned} \tag{A.6}$$

Knowing that $y_i - y = \ln(z'/x_i)$ and replacing $y$ with $y_i - y'$, we obtain the kernel

$$P^\alpha_{i-k} = \int_0^{y_i} \mathrm{d}y P^\alpha(y)T_k(y_i - y). \tag{A.7}$$

We note here the function $P^\alpha$ only depends on the index $i-k$ and thus is only a vector. Similarly,

$$K^\alpha_{n,j} = \int \mathrm{d}k'^2\ K_\alpha(k_n,k')T_j(k') \tag{A.8}$$

It is worth showing the calculations on some boundary terms arising from the non-singular splitting function $\tilde{P}_{gg} = P_{gg} - 1/z$ and

$$P_{gg} = 2C_A\left[\frac{x}{(1-x)_+} + \frac{1-x}{x} + x\left(1-x\right)\right] + \delta(1-x)\frac{11C_A - 4n_fT_R}{6}. \tag{A.9}$$

Here, $n_f = 4$, $T_R = 1/2$, $C_A = 3$. We are particularly interested in these two terms in the splitting function,

$$\frac{x}{(1-x)_+} \quad \text{and} \quad \delta(1-x). \tag{A.10}$$

Both terms need to be taken better care of, especially at $x = 1$, $y = 0$ and any other terms can be just normally numerically integrated. We start with the $x/(1-x)_+$ term and we shall introduce the following trick,

$$
\begin{aligned}
\int_x^1 \mathrm{d}z \frac{f(z)}{(1-z)_+} &= \int_0^1 \mathrm{d}z \frac{f(z)}{(1-z)_+} - \int_0^x \mathrm{d}z \frac{f(z)}{(1-z)_+} \\
&= \int_0^1 \mathrm{d}z \frac{f(z)-f(1)}{1-z} - \int_x^1 \mathrm{d}z \frac{f(z)}{1-z} \\
&= \int_x^1 \mathrm{d}z \frac{f(z)-f(1)}{1-z} - \int_0^x \mathrm{d}z \frac{f(1)}{1-z} \\
&= \int_x^1 \mathrm{d}z \frac{f(z)-f(1)}{1-z} + f(1)\ln(1-x). \qquad \text{(A.11)}
\end{aligned}
$$

The only test function $T_i$ has non-zero contribution to eq.(A.7) at $x = 1$ is $T_0(x)$, then with $T_0(x)|_{x=1} = 1$,

$$
\begin{aligned}
\int_{x_1}^1 \mathrm{d}z \frac{zT_0(z)}{(1-z)_+} &= \int_{x_1}^1 \mathrm{d}z \frac{zT_0(z)-T_0(1)}{1-z} + T_0(1)\ln(1-x_1) \\
&= \int_{x_1}^1 \mathrm{d}z \frac{zT_0(z)-1}{1-z} + \ln\left(1-e^{-\Delta y}\right) \qquad \text{(A.12)}
\end{aligned}
$$

Otherwise, for anywhere else, we have

$$
\int_{x_i}^1 \mathrm{d}z \frac{zT_k(z)}{(1-z)_+} = \int_{x_i}^1 \mathrm{d}z \frac{zT_k(z)}{1-z}. \qquad \text{(A.13)}
$$

For $\delta(1-x)$ term,

$$
\int_{x_k}^1 \mathrm{d}z \delta(1-z) T_i(z). \qquad \text{(A.14)}
$$

Given that $T_i(z)|_{z=1} = 0$ unless $i = 0$, we get the only non-zero contribution,

$$
\int_{x_1}^1 \mathrm{d}z \delta(1-z) T_0(z) = T(1) = 1. \qquad \text{(A.15)}
$$

There is still a subtlety we want to clarify. From the calculation above, it seems that the boundary terms are located at $i = 0$, $k = 1$ of $P_{i-k}$, where $i - k = 1$ .

This is not the full picture because we omit some contribution in (A.7) for simplicity of the derivation above. In fact, one needs to investigate $T_k(y_i - y)$ instead of $T_k(y)$. Note that

$$
T_1(y_1 - y) = T_0(y), \quad y \in [0,\ \Delta y], \qquad \text{(A.16)}
$$

with $y_1 = \Delta y$. We see that the boundary terms are actually located at $i = 1$, $k = 1$ of $P_{i-k}$, in other words, $P_0$. In principle, one can also get this $P_0$ from the case $i = 0$, $k = 0$, yet the integration for $(x_0, 1)$ is unnecessarily improper for interpretation, as $x_0 = 1$.

# Appendix B
# Lowest-order cross sections and structure functions

In this appendix, we sketch the determination of the photon-parton cross sections at the lowest order in perturbation theory, which is the basis of the analysis of the photon-photon cross section in the collinear regime $Q_1^2 \ll Q_2^2$. Such cross sections are proportional to the corresponding partonic structure functions, which in turn can be derived by the DIS coefficient functions.

### B.0.1 Transverse photon

The cross section of a virtual photon with polarization $\lambda$ scattering on a particle of momentum $P$ (e.g., a hadron) is given by (cfr. [82])

$$\sigma^{(\lambda)}(P,q) = \frac{4\pi^2\alpha}{Q^2} F^{(\lambda)}(x,Q^2) \,, \qquad x := \frac{Q^2}{2P\cdot q} \,. \tag{B.1}$$

where $F^{(\lambda)}(x,Q^2) : \lambda = L, T, 2$ are the standard structure functions with $F^{(2)} = F^{(L)} + F^{(T)}$. The integrand $\tilde{\tilde{\sigma}}(\omega,\gamma;p)$ of the double Mellin representation (4.9a) can then be written as

$$\begin{aligned} \tilde{\tilde{\sigma}}(\omega,\gamma;1) &= \int_{Q_1^2}^{\infty} \frac{\mathrm{d}s}{s} \left(\frac{Q_1^2}{s}\right)^{\omega} \int \frac{\mathrm{d}Q_1^2}{Q_1^2} \left(\frac{Q_2^2}{Q_1^2}\right)^{\gamma-\frac{1}{2}} 2\pi Q_1 Q_2\, \sigma(s,Q_1^2,Q_2^2) \\ &= \int_0^1 \frac{\mathrm{d}x}{x} x^{\omega} \int \frac{\mathrm{d}Q_1^2}{Q_1^2} \left(\frac{Q_2^2}{Q_1^2}\right)^{\gamma} (2\pi)^3 \alpha F(x,Q_1^2) \,. \end{aligned} \tag{B.2}$$

In the case of an incoming quark of flavour $a$ and small offshellness $Q_2^2 \ll Q_1^2 \equiv Q^2$, the partonic structure functions at lowest order are nothing but the corresponding coefficient functions:

$$F_0^{(T,a)}(x,Q^2) = F_0^{(2,a)}(x,Q^2) = x\, e_a^2\, C_0^{(2,q)}(x) = e_a^2 \delta(1-x)\ , \qquad F_0^{(L,a)}(x,Q^2) = 0\ . \tag{B.3}$$

Therefore, at the lowest order only the transverse polarization is effective and we have

$$\tilde{\tilde{\sigma}}_0^{(T,a)}(\omega,\gamma;1) = \int_0^1 \frac{\mathrm{d}x}{x} x^\omega \int \frac{\mathrm{d}Q_1^2}{Q_1^2} \left(\frac{Q_2^2}{Q_1^2}\right)^\gamma (2\pi)^3 \alpha F_0^{(T,a)}(x,Q_1^2) = (2\pi)^3 \alpha\, e_a^2 \frac{1}{\gamma} \tag{B.4}$$

which is the first factor of the collinear chain (4.36), before summing over quark and antiquark flavors. By taking the inverse Mellin transform with respect to $\gamma$, we have

$$\tilde{\tilde{\sigma}}_0^{(T,a)}(\omega, Q_1^2, Q_2^2; 1) = (2\pi)^3 \alpha\, e_a^2\ , \tag{B.5}$$

representing the first factor in eq. (4.30) — again, before summing over quark and antiquark flavors.

The first non-vanishing contribution of the photon-gluon structure functions starts at $\mathcal{O}(\alpha_s)$. In the collinear limit, i.e., considering the strong ordering of partons' momenta, each rung provides a factor $\int_{k_{i-1}^2}^{k_i^2} \frac{\mathrm{d}k^2}{k^2} \frac{\alpha_s(k^2)}{2\pi} P_{ab}(\omega)$. With fixed running coupling such a factor reduces to $\frac{\alpha_s}{2\pi} \log \frac{k_i^2}{k_{i-1}^2} P_{ab}(\omega)$, which becomes $\frac{\alpha_s}{2\pi} P_{ab}(\omega)/\gamma$ in $\gamma$-space. Therefore, at $\mathcal{O}(\alpha_s)$, for a transverse photon we have

$$\tilde{\tilde{\sigma}}_1^{(T,g)}(\omega,\gamma;1) = \sum_a (2\pi)^3 \alpha\, e_a^2 \frac{1}{\gamma} \cdot \frac{\alpha_s}{2\pi} \frac{P_{(q=a)g}(\omega)}{\gamma}\ . \tag{B.6}$$

in agreement with the first factors of eq. (4.36) since $\sum_a e_a^2 = 2\sum_q e_q^2$. The other factors follow from the remaining two vertices.

### B.0.2 Longitudinal photon

The longitudinal structure function starts at $\mathcal{O}(\alpha\alpha_s)$ in perturbation theory, and receive contributions from gluons and quarks. We start by considering the gluon-initiated structure function, which is well known in the literature, and can be read, e.g., from eq. (B.5) of ref. [116]

$$F_1^{(L,g)}(x,Q^2) = x\, \frac{\sum_a e_a^2}{2N_f}\, C_1^{(L,g)}(x, Q^2/\mu_F^2) = \frac{\alpha_s}{2\pi} \Big(\sum_a e_a^2\Big) T_R\, 4\, x^2 (1-x)\ . \tag{B.7}$$

The corresponding longitudinal photon-gluon cross section in Mellin space can then be determined from eq. (B.2) and reads

$$\tilde{\tilde{\sigma}}_1^{(L,g)}(\omega,\gamma;1) = \frac{16\pi^2\alpha\alpha_{\rm s}\left(\sum_a e_a^2\right)T_R}{\gamma\,(2+\omega)(3+\omega)}\ . \tag{B.8}$$

It is straightforward to check that the r.h.s. of eq. (B.8) is proportional to the simple pole at $\gamma = 0$ of the BNP longitudinal impact factor with exact kinematics with its full $\omega$-dependence, just like the r.h.s. of eq. (B.6) is proportional to the double pole of the BNP transverse impact factor:

$$\tilde{\tilde{\sigma}}_1^{(T,g)}(\omega,\gamma;1) = 2\pi\Big(\sum_a e_a^2\Big)T_R\,S_T(\omega,\gamma) + \mathcal{O}(\gamma^{-1}) \tag{B.9}$$

$$\tilde{\tilde{\sigma}}_1^{(L,g)}(\omega,\gamma;1) = 2\pi\Big(\sum_a e_a^2\Big)T_R\,S_L(\omega,\gamma) + \mathcal{O}(\gamma^{0})\ . \tag{B.10}$$

The quark-initiated structure function, is also well known in the literature, and can be read, e.g., from eq. (B.1) of ref. [116]:

$$F_1^{(L,a)}(x,Q^2) = x\ e_a^2\ C_1^{(L,q)}(x,Q^2/\mu_F^2) = \frac{\alpha_{\rm s}}{2\pi}e_a^2\,C_F\,2x^2 \qquad (a = \text{quark or antiquark})\ . \tag{B.11}$$

The corresponding longitudinal photon-quark cross section in Mellin space can then be determined from eq. (B.2) and reads

$$\tilde{\tilde{\sigma}}_1^{(L,a)}(\omega,\gamma;1) = \frac{8\pi^2\alpha\alpha_{\rm s}\,e_a^2\,C_F}{\gamma\,(2+\omega)} \qquad (a = \text{quark or antiquark})\ . \tag{B.12}$$

Summing over all quarks and antiquarks we get

$$\sum_a \tilde{\tilde{\sigma}}_1^{(L,a)}(\omega,\gamma;1) = \frac{C_F}{T_R}\,\frac{3+\omega}{2}\,\tilde{\tilde{\sigma}}_1^{(L,g)}(\omega,\gamma;1)\ . \tag{B.13}$$

In practice, the blob connecting a longitudinal photon to all quarks and antiquarks displayed in fig. 4.9(c) is equal to the blob connecting the longitudinal photon to a gluon in fig. 4.9(a),(b) up to the additional multiplicative factor $C_F(3+\omega)/(2T_R)$.

# Bibliography


[1] C. M. LATTES, H. Muirhead, G. P. Occhialini, and C. F. Powell, "Processes involving charged mesons," *Nature*, vol. 159, no. 4047, pp. 694–697, 1947. Publisher: Nature Publishing Group UK London.

[2] H.-X. Chen, W. Chen, X. Liu, and S.-L. Zhu, "The hidden-charm pentaquark and tetraquark states," *Physics Reports*, vol. 639, pp. 1–121, 2016. Publisher: Elsevier.

[3] Y.-R. Liu, H.-X. Chen, W. Chen, X. Liu, and S.-L. Zhu, "Pentaquark and tetraquark states," *Progress in Particle and Nuclear Physics*, vol. 107, pp. 237–320, 2019. Publisher: Elsevier.

[4] J. Greensite, *An Introduction to the Confinement Problem*, vol. 972 of *Lecture Notes in Physics*. Cham: Springer International Publishing, 2020.

[5] J. Collins, *Foundations of perturbative QCD*. Cambridge University Press, 2011.

[6] M. Breidenbach, J. I. Friedman, H. W. Kendall, E. D. Bloom, D. H. Coward, H. DeStaebler, J. Drees, L. W. Mo, and R. E. Taylor, "Observed Behavior of Highly Inelastic Electron-Proton Scattering," *Physical Review Letters*, vol. 23, pp. 935–939, Oct. 1969.

[7] G. Altarelli and G. Parisi, "Asymptotic freedom in parton language," *Nuclear Physics B*, vol. 126, no. 2, pp. 298–318, 1977.

[8] Y. L. Dokshitzer, "Calculation of the structure functions for deep inelastic scattering and e+ e-annihilation by perturbation theory in quantum chromodynamics," *Zh. Eksp. Teor. Fiz*, vol. 73, no. 1216, p. 26, 1977.

[9] V. N. Gribov and L. N. Lipatov, "DEEP INELASTIC ep-SCATTERING IN A PERTURBATION THEORY.," tech. rep., Inst. of Nuclear Physics, Leningrad, 1972.

[10] V. Gribov and L. Lipatov, "e+ e-pair annihilation and deep inelastic ep scattering in perturbation theory," *Soviet Journal of Nuclear Physics*, vol. 15, pp. 675–675, 1972.

[11] I. Abt, T. Ahmed, V. Andreev, B. Andrieu, R.-D. Appuhn, M. Arpagaus, A. Babaev, H. Bärwolff, J. Ban, and P. Baranov, "Measurement of the proton structure function F2 (x, Q2) in the low-x region at HERA," *Nuclear Physics B*, vol. 407, no. 3, pp. 515–535, 1993.

[12] M. Derrick, D. Krakauer, S. Magill, B. Musgrave, J. Repond, S. Repond, R. Stanek, R. L. Talaga, J. Thron, and F. Arzarello, "Measurement of the proton structure function F2 in ep scattering at HERA," *Physics Letters B*, vol. 316, no. 2-3, pp. 412–426, 1993.

[13] L. N. Lipatov, "The bare pomeron in quantum chromodynamics," *Zh. Eksp. Teor. Fiz*, vol. 90, p. 1536, 1986.

[14] L. N. Lipatov, "The bare pomeron in quantum chromodynamics," *Soviet Journal of Experimental and Theoretical Physics*, vol. 63, no. 5, p. 904, 1986.

[15] E. A. Kuraev, L. N. Lipatov, and V. S. Fadin, "Pomeranchuk singularity in nonabelian gauge theories," *Sov. Phys.-JETP (Engl. Transl.);(United States)*, vol. 45, no. 2, 1977.

[16] E. A. Kuraev, L. N. Lipatov, and V. S. Fadin, "Pomeranchuk singularity in non-abelian gauge theories," *Zhurnal Ehksperimental'noj i Teoreticheskoj Fiziki*, vol. 72, no. 2, pp. 377–389, 1977.

[17] Y. Y. Balitsky and L. N. Lipatov, "The Pomeranchuk singularity in quantum chromodynamics," *Yad. Fiz.*, vol. 28, pp. 1597–1611, 1978.

[18] I. I. Balitsky and L. N. Lipatov, "The Pomeranchuk Singularity in Quantum Chromodynamics," *Sov. J. Nucl. Phys.*, vol. 28, pp. 822–829, 1978.

[19] J. B. Bronzan and R. L. Sugar, "Regge Behavior of Spontaneously Broken Non-abelian Gauge Theory," *Phys. Rev. D*, vol. 17, p. 585, 1978.

[20] T. Jaroszewicz, "Infrared Divergences and Regge Behavior in QCD," *Acta Phys. Polon. B*, vol. 11, p. 965, 1980.

[21] V. S. Fadin and L. N. Lipatov, "BFKL pomeron in the next-to-leading approximation," *Physics Letters B*, vol. 429, pp. 127–134, June 1998.

[22] M. Ciafaloni and G. Camici, "Energy Scale(s) and Next-to-leading BFKL Equation," *Physics Letters B*, vol. 430, pp. 349–354, July 1998.

[23] I. Balitsky and G. A. Chirilli, "Next-to-leading order evolution of color dipoles," *Phys. Rev. D*, vol. 77, p. 014019, 2008.

[24] A. Kovner, M. Lublinsky, and Y. Mulian, "NLO JIMWLK evolution unabridged," *Journal of High Energy Physics*, vol. 2014, p. 114, Aug. 2014.

[25] M. Lublinsky and Y. Mulian, “High energy QCD at NLO: from light-cone wave function to JIMWLK evolution,” *Journal of High Energy Physics*, vol. 2017, p. 97, May 2017.

[26] G. P. Salam, “A resummation of large sub-leading corrections at small x,” *Journal of High Energy Physics*, vol. 1998, no. 07, p. 019, 1998.

[27] G. Altarelli, R. D. Ball, and S. Forte, “Resummation of singlet parton evolution at small x,” *Nuclear Physics B*, vol. 575, no. 1-2, pp. 313–329, 2000.

[28] G. Altarelli, R. D. Ball, and S. Forte, “Small-x resummation and HERA structure function data,” *Nuclear Physics B*, vol. 599, no. 1-2, pp. 383–423, 2001.

[29] G. Altarelli, R. D. Ball, and S. Forte, “Factorization and resummation of small x scaling violations with running coupling,” *Nuclear Physics B*, vol. 621, no. 1-2, pp. 359–387, 2002.

[30] G. Altarelli, R. D. Ball, and S. Forte, “An anomalous dimension for small x evolution,” *Nuclear Physics B*, vol. 674, no. 1-2, pp. 459–483, 2003.

[31] G. Altarelli, R. D. Ball, and S. Forte, “Small x Resummation with Quarks: Deep-Inelastic Scattering,” *Nucl. Phys. B*, vol. 799, pp. 199–240, 2008.

[32] M. Ciafaloni, D. Colferai, and G. P. Salam, “A collinear model for small x physics,” *JHEP*, vol. 10, p. 017, 1999.

[33] M. Ciafaloni, D. Colferai, and G. P. Salam, “Renormalization group improved small x equation,” *Phys. Rev. D*, vol. 60, p. 114036, 1999.

[34] M. Ciafaloni, D. Colferai, G. P. Salam, and A. M. Stasto, “Renormalization group improved small x Green’s function,” *Phys. Rev. D*, vol. 68, p. 114003, 2003.

[35] M. Ciafaloni, D. Colferai, G. P. Salam, and A. M. Stasto, “The Gluon splitting function at moderately small x,” *Phys. Lett. B*, vol. 587, pp. 87–94, 2004.

[36] M. Ciafaloni, D. Colferai, G. P. Salam, and A. M. Stasto, “A Matrix formulation for small-x singlet evolution,” *JHEP*, vol. 08, p. 046, 2007.

[37] A. Sabio Vera, “An ’All-poles’ approximation to collinear resummations in the Regge limit of perturbative QCD,” *Nucl. Phys. B*, vol. 722, pp. 65–80, 2005.

[38] M. Bonvini, S. Marzani, and T. Peraro, “Small-x resummation from HELL,” *Eur. Phys. J. C*, vol. 76, no. 11, p. 597, 2016.

[39] R. S. Thorne, “The Running coupling BFKL anomalous dimensions and splitting functions,” *Phys. Rev. D*, vol. 64, p. 074005, 2001.

[40] C. D. White and R. S. Thorne, “A Global Fit to Scattering Data with NLL BFKL Resummations,” *Phys. Rev. D*, vol. 75, p. 034005, 2007.

[41] M. Ciafaloni, "Coherence effects in initial jets at small Q2/s," *Nuclear Physics B*, vol. 296, no. 1, pp. 49–74, 1988.

[42] B. Andersson, G. Gustafson, and J. Samuelsson, "The Linked dipole chain model for DIS," *Nucl. Phys. B*, vol. 467, pp. 443–478, 1996.

[43] J. Kwiecinski, A. D. Martin, and P. J. Sutton, "Constraints on gluon evolution at small x," *Z. Phys. C*, vol. 71, pp. 585–594, 1996.

[44] J. Kwiecinski, A. D. Martin, and A. M. Stasto, "A Unified BFKL and GLAP description of F2 data," *Phys. Rev. D*, vol. 56, pp. 3991–4006, 1997.

[45] M. Ciafaloni, D. Colferai, G. Salam, and A. Staśto, "Extending QCD perturbation theory to higher energies," *Physics Letters B*, vol. 576, pp. 143–151, Dec. 2003.

[46] P. Achard, O. Adriani, M. Aguilar-Benitez, J. Alcaraz, G. Alemanni, J. Allaby, A. Aloisio, M. G. Alviggi, H. Anderhub, and V. P. Andreev, "Double-tag events in two-photon collisions at LEP," *Physics Letters B*, vol. 531, no. 1-2, pp. 39–51, 2002.

[47] The OPAL Collaboration and G. Abbiendi et al., "Measurement of the hadronic cross-section for the scattering of two virtual photons at LEP," *The European Physical Journal C*, vol. 24, pp. 17–31, May 2002.

[48] M. Deak, K. Kutak, W. Li, and A. M. Staśto, "On the different forms of the kinematical constraint in BFKL," *The European Physical Journal C*, vol. 79, p. 647, Aug. 2019.

[49] W. Li and A. M. Staśto, "Structure functions from renormalization group improved small x evolution," *The European Physical Journal C*, vol. 82, p. 562, June 2022.

[50] D. Colferai, W. Li, and A. M. Staśto, "Renormalization group improved photon impact factors and the high energy virtual photon scattering," *Journal of High Energy Physics*, vol. 2024, p. 106, Jan. 2024.

[51] S. Coleman and D. J. Gross, "Price of Asymptotic Freedom," *Physical Review Letters*, vol. 31, pp. 851–854, Sept. 1973.

[52] Particle Data Group, "Review of particle physics," *Progress of Theoretical and Experimental Physics*, vol. 2022, no. 8, p. 083C01, 2022. Publisher: Oxford University Press.

[53] J. Meyer, "HERA e-p scattering events observed in the H1Detector," 2005. Publication Title: H1Events DESY.

[54] R. P. Feynman, "Very High-Energy Collisions of Hadrons," *Physical Review Letters*, vol. 23, pp. 1415–1417, Dec. 1969.

[55] J. D. Bjorken and E. A. Paschos, "Inelastic Electron-Proton and $\gamma$-Proton Scattering and the Structure of the Nucleon," *Physical Review*, vol. 185, pp. 1975–1982, Sept. 1969.

[56] J. D. Bjorken and E. A. Paschos, "High-Energy Inelastic Neutrino-Nucleon Interactions," *Physical Review D*, vol. 1, pp. 3151–3160, June 1970.

[57] R. K. Ellis, W. J. Stirling, and B. R. Webber, *QCD and collider physics*. Cambridge university press, 2003.

[58] J. Collins and J.-W. Qiu, "$k_t$ factorization is violated in production of high-transverse-momentum particles in hadron-hadron collisions," *Phys. Rev. D*, vol. 75, p. 114014, 2007. _eprint: 0705.2141.

[59] G. Curci, W. Furmanski, and R. Petronzio, "Evolution of parton densities beyond leading order: the non-singlet case," *Nuclear Physics B*, vol. 175, no. 1, pp. 27–92, 1980.

[60] W. Furmanski and R. Petronzio, "Singlet parton densities beyond leading order," *Phys. Lett. B*, vol. 97, no. CERN-TH-2933, pp. 437–442, 1980.

[61] W. Furmanski and R. Petronzio, "Lepton-hadron processes beyond leading order in quantum chromodynamics," *Zeitschrift für Physik C Particles and Fields*, vol. 11, pp. 293–314, 1982.

[62] S. Moch, J. A. Vermaseren, and A. Vogt, "The three-loop splitting functions in QCD: The non-singlet case," *Nuclear Physics B*, vol. 688, no. 1-2, pp. 101–134, 2004.

[63] A. Vogt, S. Moch, and J. Vermaseren, "The three-loop splitting functions in QCD: the singlet case," *Nuclear Physics B*, vol. 691, no. 1-2, pp. 129–181, 2004.

[64] G. P. Salam, "An introduction to leading and next-to-leading BFKL," Oct. 1999.

[65] L. V. Gribov, E. M. Levin, and M. G. Ryskin, "Semihard processes in QCD," *Physics Reports*, vol. 100, pp. 1–150, Nov. 1983.

[66] J. R. Forshaw and D. A. Ross, *Quantum chromodynamics and the pomeron*. No. 9, Cambridge University Press, 1997.

[67] J. Bartels, "High-energy behaviour in a non-Abelian gauge theory:(I). Tn→ m in the leading ln s approximation," *Nuclear Physics B*, vol. 151, pp. 293–341, 1979. Publisher: Elsevier.

[68] L. Lipatov, "POMERON IN QUANTUM CHROMODYNAMICS," in *Advanced Series on Directions in High Energy Physics*, vol. 5, pp. 411–489, WORLD SCIENTIFIC, July 1989.

[69] N. Gromov, F. Levkovich-Maslyuk, and G. Sizov, "Pomeron Eigenvalue at Three Loops in N = 4 Supersymmetric Yang-Mills Theory," *Physical Review Letters*, vol. 115, p. 251601, Dec. 2015.

[70] V. N. Velizhanin, "BFKL pomeron in the next-to-next-to-leading approximation in the planar N=4 SYM theory," Aug. 2015.

[71] S. Caron-Huot and M. Herranen, "High-energy evolution to three loops," *Journal of High Energy Physics*, vol. 2018, p. 58, Feb. 2018.

[72] A. H. Mueller, *Perturbative quantum chromodynamics*, vol. 5. World Scientific, 1989.

[73] D. Amati, R. Petronzio, and G. Veneziano, "Relating hard QCD processes through universality of mass singularities (II)," *Nuclear Physics B*, vol. 146, no. 1, pp. 29–49, 1978. Publisher: Elsevier.

[74] R. K. Ellis, H. Georgi, M. Machacek, H. D. Politzer, and G. G. Ross, "Factorization and the Parton Model in QCD," *Physics Letters B*, vol. 78, no. 2-3, pp. 281–284, 1978. Publisher: North-Holland.

[75] C. T. Sachrajda, "Inclusive production at large transverse momentum in QCD," *Physics Letters B*, vol. 76, no. 1, pp. 100–104, 1978. Publisher: Elsevier.

[76] S. B. Libby and G. Sterman, "Mass divergences in two-particle inelastic scattering," *Physical Review D*, vol. 18, pp. 4737–4745, Dec. 1978.

[77] A. H. Mueller, "Cut vertices and their renormalization: A generalization of the Wilson expansion," *Physical Review D*, vol. 18, pp. 3705–3727, Nov. 1978.

[78] A. V. Efremov and A. V. Radyushkin, "Field Theoretic Treatment of High Momentum Transfer Processes. 3. Gauge Theories," *Teor. Mat. Fiz.*, vol. 44, p. 327, 1980.

[79] S. Catani and F. Hautmann, "High-energy factorization and small-x deep inelastic scattering beyond leading order," *Nuclear Physics B*, vol. 427, pp. 475–524, Oct. 1994.

[80] I. Balitsky and G. A. Chirilli, "Photon impact factor and $k_t$-factorization for DIS in the next-to-leading order," *Physical Review D*, vol. 87, p. 014013, Jan. 2013. arXiv: 1207.3844.

[81] S. Catani, M. Ciafaloni, and F. Hautmann, "High energy factorization and small-x heavy flavour production," *Nuclear Physics B*, vol. 366, no. 1, pp. 135–188, 1991.

[82] A. Bialas, H. Navelet, and R. Peschanski, "Virtual photon impact factors with exact gluon kinematic," *Nuclear Physics B*, vol. 603, pp. 218–230, June 2001.

[83] D. Y. Ivanov, B. Murdaca, and A. Papa, “The $\gamma^*\gamma^*$ total cross section in next-to-leading order BFKL and LEP2 data,” *Journal of High Energy Physics*, vol. 2014, p. 58, Oct. 2014. arXiv: 1407.8447.

[84] I. Bojak and M. Ernst, “Small x resummations confronted with F2 (x, Q2) data,” *Physics Letters B*, vol. 397, no. 3-4, pp. 296–304, 1997.

[85] S. Catani, F. Fiorani, and G. Marchesini, “Small x Behavior of Initial State Radiation in Perturbative QCD,” *Nucl. Phys. B*, vol. 336, pp. 18–85, 1990.

[86] S. Catani, F. Fiorani, and G. Marchesini, “QCD Coherence in Initial State Radiation,” *Phys. Lett. B*, vol. 234, pp. 339–345, 1990.

[87] G. Marchesini, “QCD coherence in the structure function and associated distributions at small x,” *Nucl. Phys. B*, vol. 445, pp. 49–80, 1995.

[88] H. Jung and others, “The CCFM Monte Carlo generator CASCADE version 2.2.03,” *Eur. Phys. J. C*, vol. 70, pp. 1237–1249, 2010.

[89] Y. L. Dokshitzer, V. A. Khoze, S. I. Troian, and A. H. Mueller, “QCD Coherence in High-Energy Reactions,” *Rev. Mod. Phys.*, vol. 60, p. 373, 1988.

[90] J. Kwiecinski and D. Strozik-Kotlorz, “Possible Parametrization of Parton Distributions Incorporating Singular Small X Behavior Implied by QCD and Its Phenomenological Implications for HERA,” *Z. Phys. C*, vol. 48, pp. 315–326, 1990.

[91] G. Beuf, “Improving the kinematics for low-x QCD evolution equations in coordinate space,” *Phys. Rev. D*, vol. 89, no. 7, p. 074039, 2014.

[92] M. Ciafaloni and D. Colferai, “The BFKL equation at next-to-leading level and beyond,” *Phys. Lett. B*, vol. 452, pp. 372–378, 1999.

[93] A. V. Kotikov and L. N. Lipatov, “DGLAP and BFKL evolution equations in the N=4 supersymmetric gauge theory,” *Nuclear Physics B*, vol. 661, pp. 19–61, June 2003.

[94] S. Marzani, R. D. Ball, P. Falgari, and S. Forte, “BFKL at next-to-next-to-leading order,” *Nucl. Phys. B*, vol. 783, pp. 143–175, 2007.

[95] G. Camici and M. Ciafaloni, “Non-abelian qq contributions to small-x anomalous dimensions,” *Physics Letters B*, vol. 386, no. 1-4, pp. 341–349, 1996.

[96] G. Camici and M. Ciafaloni, “Irreducible part of the next-to-leading BFKL kernel,” *Phys. Lett. B*, vol. 412, pp. 396–406, 1997.

[97] K. Kutak and S. Sapeta, “Gluon saturation in dijet production in p-Pb collisions at the Large Hadron Collider,” *Physical Review D*, vol. 86, p. 094043, Nov. 2012.

[98] S. Catani, M. Ciafaloni, and F. Hautmann, “Gluon contributions to small x heavy flavour production,” *Physics Letters B*, vol. 242, no. 1, pp. 97–102, 1990.

[99] J. C. Collins and R. K. Ellis, “Heavy-quark production in very high energy hadron collisions,” *Nuclear Physics B*, vol. 360, no. 1, pp. 3–30, 1991.

[100] A. J. Askew, J. Kwiecinski, A. D. Martin, and P. J. Sutton, “QCD predictions for deep-inelastic structure functions at the DESY ep collider HERA,” *Physical Review D*, vol. 47, pp. 3775–3782, May 1993.

[101] M. A. Kimber, *Unintegrated parton distributions.* Doctoral, Durham University, 2001.

[102] A. J. Askew, J. Kwiecinski, A. D. Martin, and P. J. Sutton, “Properties of the BFKL equation and structure function predictions for DESY HERA,” *Physical Review D*, vol. 49, pp. 4402–4414, May 1994.

[103] J. Berger and A. M. Staśto, “Small-x nonlinear evolution with impact parameter and the structure function data,” *Physical Review D*, vol. 84, p. 094022, Nov. 2011.

[104] H. Mäntysaari and B. Schenke, “Confronting the impact parameter dependent JIMWLK evolution with HERA data,” *Physical Review D*, vol. 98, p. 034013, Aug. 2018.

[105] A. Donnachie and P. V. Landshoff, “Total cross sections,” *Physics Letters B*, vol. 296, pp. 227–232, Dec. 1992.

[106] M. Glück, E. Reya, and A. Vogt, “Dynamical parton distributions of the proton and small-x physics,” *Zeitschrift für Physik C Particles and Fields*, vol. 67, pp. 433–447, Sept. 1995.

[107] T. H1 and Z. Collaborations, “Combined Measurement and QCD Analysis of the Inclusive ep Scattering Cross Sections at HERA,” *Journal of High Energy Physics*, vol. 2010, p. 109, Jan. 2010.

[108] H1 Collaboration, “Measurement of $D^{*\pm}$ Meson Production and Determination of $F_2^{c\bar{c}}$ at low $Q^2$ in Deep-Inelastic Scattering at HERA,” *The European Physical Journal C*, vol. 71, p. 1769, Oct. 2011.

[109] R. D. Ball, V. Bertone, M. Bonvini, S. Marzani, J. Rojo, and L. Rottoli, “Parton distributions with small-x resummation: evidence for BFKL dynamics in HERA data,” *The European Physical Journal C*, vol. 78, p. 321, Apr. 2018.

[110] G. A. Chirilli and Y. V. Kovchegov, “$\gamma^*\gamma^*$ cross section at NLO and properties of the BFKL evolution at higher orders,” *Journal of High Energy Physics*, vol. 2014, p. 99, May 2014.

[111] G. A. Chirilli and Y. V. Kovchegov, "Erratum to: $\gamma^*\gamma^*$ cross section at NLO and properties of the BFKL evolution at higher orders," *Journal of High Energy Physics*, vol. 2015, p. 75, Aug. 2015.

[112] J. Bartels, A. De Roeck, and H. Lotter, "The $\gamma^*\gamma^*$ total cross section and the BFKL Pomeron at e+ e- colliders," *Physics Letters B*, vol. 389, no. 4, pp. 742–748, 1996.

[113] V. Budnev, I. Ginzburg, G. Meledin, and V. Serbo, "The two-photon particle production mechanism. Physical problems. Applications. Equivalent photon approximation," *Physics Reports*, vol. 15, pp. 181–282, Jan. 1975.

[114] I. Schienbein, "Two-Photon Processes and Photon Structure," *Annals of Physics*, vol. 301, pp. 128–156, Nov. 2002. arXiv:hep-ph/0205301.

[115] G. A. Chirilli and Y. V. Kovchegov, "Solution of the NLO BFKL equation and a strategy for solving the all-order BFKL equation," *Journal of High Energy Physics*, vol. 2013, p. 55, June 2013.

[116] E. B. Zijlstra and W. L. van Neerven, "Order-$\alpha_s^2$ QCD corrections to the deep inelastic proton structure functions F2 and FL," *Nuclear Physics B*, vol. 383, pp. 525–574, Sept. 1992.

# Vita

**Wanchen Li**

## Education

**The Pennsylvania State University** Pennsylvania, US
*Ph.D. in Physics* *2017 – 2024*

**Nanjing University** Nanjing, China
*B.S. in Physics* *2013 – 2017*

## Research Interest

High Energy Physics Phenomenology, Quantum Chromodynamics, Computational Physics.

## Publication

1. M. Deak, K. Kutak, W. Li and A. M. Staśto, "On the different forms of the kinematical constraint in BFKL,"
   Eur. Phys. J. C **79**, no.8, 647 (2019)
   doi:10.1140/epjc/s10052-019-7171-z [arXiv:1906.09062 [hep-ph]].

2. W. Li and A. M. Stasto, "Structure functions from renormalization group improved small x evolution,"
   Eur. Phys. J. C **82**, no.6, 562 (2022)
   doi:10.1140/epjc/s10052-022-10523-6 [arXiv:2201.10579 [hep-ph]].

3. D. Colferai, W. Li and A. M. Stasto, "Renormalization group improved photon impact factors and the high energy virtual photon scattering,"
   JHEP **01**, 106 (2024)
   doi:10.1007/JHEP01(2024)106 [arXiv:2311.07443 [hep-ph]].